Developments in the Built Environment 17 (2024) 100378

Contents lists available at ScienceDirect

Developments in the Built Environment

journal homepage: www.sciencedirect.com/journal/developments-in-the-built-environment

Concrete 3D printing technology for sustainable construction: A review on raw material, concrete type and performance

Xiaonan Wang [a,b], Wengui Li [a,*], Yipu Guo [a], Alireza Kashani [a], Kejin Wang [c], Liberato Ferrara [d], Isabel Agudelo [e]

[a] Centre for Infrastructure Engineering and Safety, School of Civil and Environmental Engineering, The University of New South Wales, NSW 2052, Australia
[b] School of Civil and Environmental Engineering, University of Technology Sydney, NSW 2007, Australia
[c] Department of Civil, Construction and Environmental Engineering, Iowa State University, IA 50011, USA
[d] Department of Civil and Environmental Engineering, Politecnico di Milano, 20133 Milano MI, Italy
[e] School of Industrial Design, National University of Colombia, Ave Cra 30 #45-3, Bogotá, Colombia

ARTICLE INFO

Keywords:
Three-dimensional printing concrete
Functional concrete
Sustainable concrete
Economy and environment

ABSTRACT

This paper reviews recent developments and proposes perspectives for future research on three-dimensional printing concrete (3DPC). This review originally analyses the 3DP applications combined with concrete types that are classified into three groups: functional concrete, sustainable concrete, and special concrete. The 3DP technique shows different effects on concrete types due to various modification methods (e.g., nano-additive, fibre addition, and chemical reagent) and challenging requirements (e.g., anisotropy exploit and defect). Summarily, the oriented fibre of 3DPC is a double-edged sword, asking for optimal structural design for engineered cementitious composite (ECC), ultra-high-performance concrete (UHPC), and most fibre-improved concrete. The 3DP technique is not propitious to all concrete types, such as foam concrete, because the additional pressure in the printing process poses a huge disadvantage to foam stability. This paper also proposes the 3DPC protentional from the view of concrete features, which represents a contribution to advanced concrete technology and 3DPC development direction.

1. Introduction

Three-dimension printing (3DP) is a technology aiming for smart manufacturing, saving resource, and informatization management that benefit high efficiency manufacturing, eco-friendly development, and low cost. The capability has been proven in various areas (Ngo et al., 2018) and arouses interest around the world. This technology also leads to a rapid growth of 3DP concrete (3DPC), which enables 3DPC to be a trending topic, as shown in Fig. 1, based on the search on Web of science data in November 2023 using the following keywords: (3D printing OR additive manufacturing) AND (concrete OR cement OR building OR mortar).

1.1. 3DPC processes and benefits

Traditional printing is restricted to the two-dimensional plane (like the ink is printed on paper line by line), while the 3DP technology adopts the theory and expands to the real structure. Briefly, 3DPC is fabricated layer by layer without conventional formwork, showing excellent effectiveness and design flexibility. The process poses higher challenges to computer-aid intelligent design and properties of printed materials, but it requires less labour and makes the complex structure possible (García de Soto et al., 2018). These benefits directly reduce material waste and time consumption, leading to less pollution, higher building efficiency, less injury, etc. The details will be elaborated in this paper. In summary, 3DPC is a highly efficient technology for smart manufacturing with less burden on the environment, which brings bright prospects to modern civil engineering (Muñoz et al., 2021; Alhumayani et al., 2020).

The 3DP technique has attracted much attention in various areas and presented promising advantages in concrete applications. The lower cost of labour and formwork, high building effectiveness, compatibility for intelligent construction, which may bring benefit on economy and environment, are generally believed as prominent advantages of 3DP. Ji et al. (2019) proposed a 60–80% reduction in working days and an over 60% reduction in waste generation due to 3DP based on the case in (Ji et al., 2019). At current stage, high cost and consumption of 3DPC is common (Ebrahimi et al., 2022; Flatt and Wangler, 2022) but the future

* Corresponding author. School of Civil and Environmental Engineering, The University of New South Wales, NSW 2052, Australia.
E-mail address: wengui.li@unsw.edu.au (W. Li).

https://doi.org/10.1016/j.dibe.2024.100378
Received 30 November 2023; Received in revised form 22 January 2024; Accepted 13 February 2024
Available online 23 February 2024

Abbreviation

3DP	Three-dimension printing
3DPC	Three-dimension printing concrete
CAB	Coarse aggregate binding
DoF	Degrees of freedom
FA	Fly ash
GGBS	Ground Granulated Blast-furnace Slag
HPMC	Hydroxypropyl methylcellulose
LF	Limestone
NS	Nano-silica
PC	Portland cement
PCE	Polycarboxylate ether
PCM	Phase change material
PE	Polyethylene
PP	Polypropylene
RA	Recycled aggregate
RCA	Recycled coarse aggregate
RFA	Recycled fine aggregate
SCA	Selective cement activation
SF	Silica fume
SP	Superplasticizer
SPI	Selective paste intrusion
TC	Thermal conductivity
VMA	Viscosity modifying admixture
WG	Waste glass

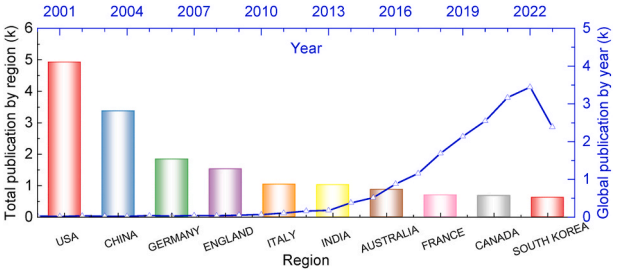

Fig. 1. Publication for 3DPC in main regions and growth by year.

is bright (Meng et al., 2023; Tu et al., 2023). More details are required to analyse the performance of 3DPC on the economy, environment, and building efficiency. The reliability has been proved in successful large-scale cases, but some the benefits are not yet fully researched or demonstrated (Tinoco et al., 2022).

1.2. Recent achievements and applications

1.2.1. 3D concrete printing with shape variety and accuracy

The flexible shape design of 3DP is attractive in construction. Anton et al. (2021) utilised the benefit of 3DP on aesthetic design and proposed a platform to construct sophisticated bespoke columns with a decent production accuracy (within 15 mm) as shown in Fig. 2(a). The advantage of 3DPC in shape variety was remarkable in the design and production of concrete shells. A successful application (a free-form concrete shell) shown in Fig. 2(b) was fabricated based on a strain-hardening cement-based composite, which was a difficult job for using the casting method (Tošić et al., 2022). The benefit of 3D shape was also illustrated in Fig. 2(c) called Knitting Concrete (Westerlind et al., 2020). Although some complex structures could be done by the conventional cast, a great deal of manpower, formwork, cost and time

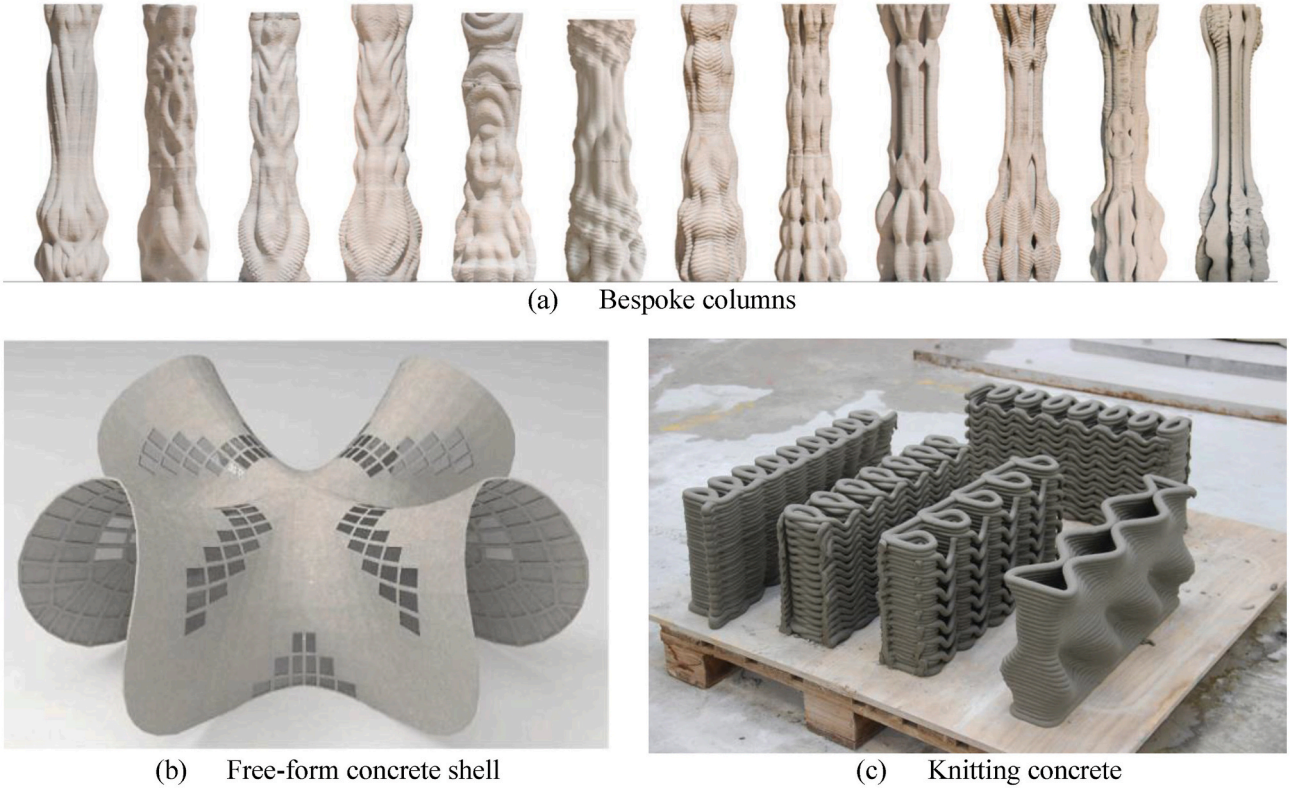

Fig. 2. Benefit of 3DP on various shapes.

were required (Chen et al., 2024; Li et al., 2024; Liu et al., 2024; Zhao et al., 2024).

1.2.2. 3DPC elements for assembled structure

Besides printing whole structures, 3DPC could be applied to elements for assembled structures that may have better working performance at the current stage. Vantyghema et al. (Vantyghem et al., 2020) designed a girder with a span of 4 m in Belgium shown in Fig. 3(a). The topology optimisation and post-tensioning strand provided great strength and an obvious material saving. Asprone et al. (2018) used a reinforcing method for a 3DP beam in Italy shown in Fig. 3(b). Although the overall nonlinear flexural capability was lower due to local failure mechanisms, the initial flexural stiffness was equal to the full solid counterpart, which presented significant material savings. A full-scale bridge with a span of 6.5 m and a width of 3.5 m was printed in Netherlands (Salet et al., 2018) shown in Fig. 3(c). Apart from main reinforcement during assembly, reinforcement cable was embedded during printing along with filaments. A synthetic epoxy-based interface material was applied to the cross-section to smoothen the surface. The in-situ test proved the load capability of 57 kN. The above cases used a similar construction procedure to produce 3DPC segments and then assemble them into structures with post-reinforcement. A bus station was installed by printed components (Zhang et al., 2019a) as shown in Fig. 3(d) that cost less than 12 h for 3DPC and 5 h for installation. The cooperation of 3DPC and assembled structure presented outstanding efficiency.

1.2.3. Large scale 3DPC structures

The large scale is another feature of 3DPC when compared to other 3DP products made by other industries, like 3DP bones. Many structures were successfully constructed to prove the potential of 3DP large structures. A wall structure consisting of two 3D printing polymer-foam walls and the inner self-compacting concrete filling was used to build a 95 m^2 house in Nantes, France (Furet et al., 2019). Ji et al. (2019) built a power distribution substation with on-site printed walls and casted columns, where horizontal steel mesh was embedded to enhance the integrity as a part of ring beam. A structure with dimensions of 78 × 60 × 90 cm was printed in 150 min in the lab by Weng et al. (2019) and showed an acceptable fireproof ability. Then they (Weng et al., 2020) enlarged this structure to a bathroom unit by printing the top part, bottom part, and cast base slab. This prefabricated unit could be installed in buildings. He et al., (2020) printed partial wall elements and assembled them as a vertical green wall. The benefit of 3DP on shape design helps the wall become more energy effective. Diggs-McGee et al., (2019) proved that a 47.6 m^2 building could be printed in 48 h, even under ambient disturbance. The application of 3DPC was not even limited to earth. Cesaretti et al. (2014) investigated the possibility of 3DP construction on the moon based on the lunar soil where the limited material, machine, and labour were the main challenges. A robotic arm concrete 3DP system has a viable method to build a real-scale habitat (Meisel et al., 2021).

1.3. Objectives and scopes

This paper reviews the state-of-art research in 3DPC to illustrate the recent progress and support further development of 3DPC. In this paper, the range of concrete is rough for reading-friendly. For instance, concrete without coarse aggregates (normally defined as mortar) and alkali-activated concrete (normally defined as geopolymer) are also described as concrete in this paper. This paper mainly emphasises intrinsic printing features and material modification. Meanwhile, vital information about 3D printers and the models for printing paths are included to give comprehensive knowledge. Concrete material modification and testing technology have been developed over hundreds of years. Many properties are especially crucial for 3DPC, such as material thixotropy and non-destructive testing for printing quality from Section 2 to Section 4, which are concluded in this paper. Compared to conventional concrete, 3DPC requires higher time-sensitive properties and shape deformation. Also, intelligent and digital technology appears significantly in 3DPC, as shown in Section 3 and Section 4. Next, Section 5 reviews 3DPC applications for many dominant concrete types divided into three groups: functional concrete, sustainable concrete, and special concrete. The specific changes (like recycled aggregate for sustainable concrete, high alkaline condition for geopolymer, shape effect of printed filament on electromagnetism, etc.) challenge compatible modification for printing quality and functional performance. For example, the alignment effect of printing provides higher orientation consistency of fibre, but the extrusion pressure is prone to reducing foam stability for foam concrete. Many cases have been reported, but the contribution of 3DP technology is not always positive, which asks for comprehensive comments and suggestions. Current reviews of this aspect are rare. Summarily, 3DPC has different compatibilities among various concrete types, and this review is valuable for promoting the 3DP for specific concrete types with excellent effectiveness. The previous part about 3DP technology in Section 2 similarly contributes to various 3DPC application modifications. This review paper helps to broaden applications and take full advantage of 3DPC effectively.

2. 3D printing concrete

2.1. Printing methods and requirements

In this paper, the popular printing methods applied to the concrete are classified as *extrusion-* and *powder-based* methods. In the extrusion-based method, raw materials are pre-mixed and then extruded on the expected position layerwise. A high viscosity is normally expected to maintain low slump and self-support that cause the printing process to be similar to *extrusion*. The printed material is required to be extrudable and robust enough to retain a stable shape during printing. In the powder-based method, the raw materials are separated into two parts, i.e., liquid parts, and powder parts. The liquid part drips to the expected position under the control of printers. The liquid part is not limited to extremely low viscosity like the most common water, but it must can be applied continuously like fresh paste (Lowke et al., 2022). During the printing, the liquid part is applied on the expected position layer-by-layer. This process is similar to the extrusion-based method but the "paper" is powder bed so the *powder* part is highlighted, when "paper" for extrusion-based method is flat bed. The powder part (such as cement, fly ash, sand, etc.) is generally applied to each layer plane. The liquid and powder parts are printed in a crossing sequence, which is another difference. The cement hydration normally starts after the printing process in the powder-based method, while it occurs before printing in the extrusion-based method. The optimal contact between the liquid part and the powder part is critical for the final quality.

2.1.1. Extrusion-based 3DPC

The procedure of extrusion-based 3DPC is intuitive as shown in Fig. 4. In addition to the properties of the printed material, the capability of printers and printing parameters are also crucial. The material extrusion speed should match the printing speed (nozzle moving speed) in certain conditions to control the shape and quality of filaments (Tay et al., 2022). Moreover, Zhi et al. (2022) proposed the effects of spiral blade geometry on the extruded material. Chen et al. (2021) proposed an extrudability window and an operation window to ensure the printing quality by controlling the extrusion rate to match printing speed. A slow extrusion rate could cause thinner layers, or discontinuous layers, while a very high rate could lead to hose blockage. A long time interval between printed layers enabled lower layers to become stiffer to support the layers above but it reduced the bond strength between layers (Chen et al., 2020). Generally, the printing direction showed little influence but the distance between the nozzle and the printing bed was important (Ashrafi et al., 2019). Shorter distance reduced time and space for the additional gravity-leading deformation of concrete filament before

(a) 3DP topology optimized girder by Vantyghema et al

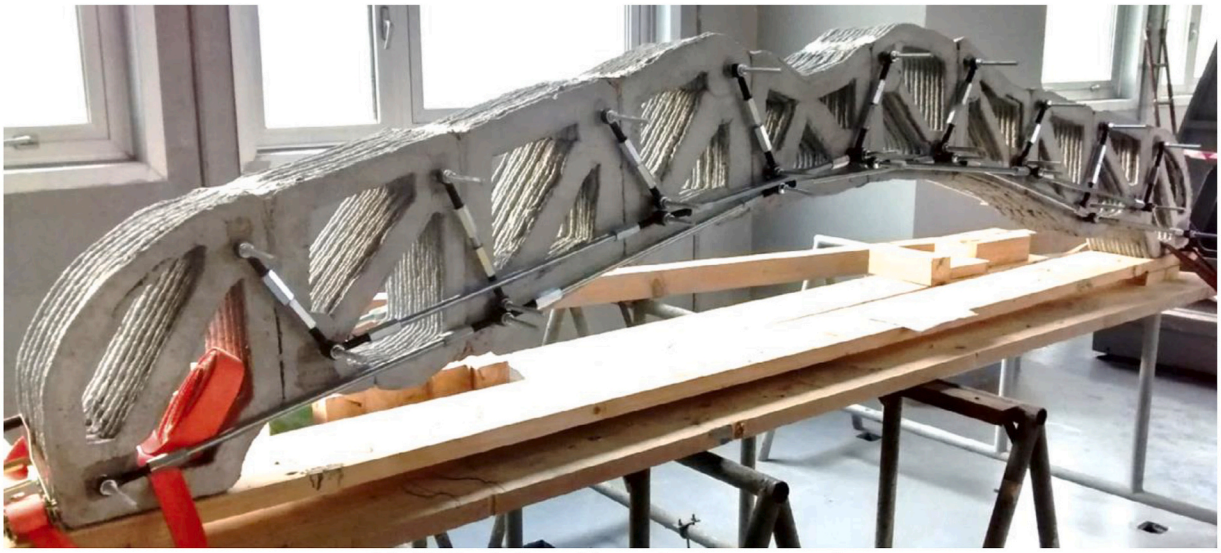

(b) 3DP reinforced beam by Asprone et al.

(c) 3DP reinforced bridge by Salet et al.

(d) Bus station by Zhang et al.

Fig. 3. Cases of 3DPC in assembled structure.

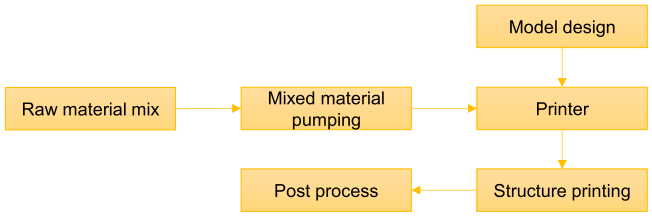

Fig. 4. Diagram of normal extrusion-based 3DPC procedure.

landing on the bed. The accumulative deformation of each layer reduced total height and enlarged the distance between the nozzle and the last layer. The printing toolpath should be rectified regularly to compensating dynamic error and maintain this distance. The mutually compatible printing parameters are crucial for 3DPC quality has been a consensus. Many printing parameters of extrusion-based printing are given in Table 1 and the information about 3DP material will be reviewed. It is noticeable that there are various units for extrusion speed. The unit like "L/min" is the volume of extruded material and "kg/h" is the mass of extruded material. The unit of "r/min" presents the rotation speed that is widely used to pump the fresh concrete. The printing speed is divided as horizontal (H) and vertical (V) directions. In many papers, only horizontal speed was presented.

2.1.2. Powder-based 3DPC

As explained above, the powder-based method (also known as binder jetting or inkjet) consists of two parts. Based on the features of the powder bed, three popular types directly used for 3DPC are illustrated as selective cement activation (SCA) (Shakor et al., 2020a; Xia et al., 2019), selective paste intrusion (SPI) (Pierre et al., 2018; Weger and Gehlen, 2021), and coarse aggregate binding (CAB) (Yu et al., 2020, 2022) as shown in Fig. 5 (Lowke et al., 2022). Furthermore, the general process is divided into six sub-processes (Lowke et al., 2022): layer application, layer compaction as appropriate, fluid application, fluid penetration, removal of the unbound particle bed (excavation) and after printing treatment (post-treatment), as shown in Fig. 6.

A balanced combination of liquid part and solid part is determined by effective degree of penetration and compaction of powder. These are the most critical in quality of powder-based 3DPC. However, the penetration performance is not easy to control for the reactive powders that showed obvious time-dependent features (Zuo et al., 2020). Take the most popular method, selective cement activation, as an example. The liquid-to-solid ratio is a foundational factor for the penetration performance (Voney et al., 2020). In summary, superfluous liquid may cause lower accuracy (normally represented oversize) due to large penetration area, while insufficient liquid bring inadequate penetration and hydration leading to a loose structure (Shakor et al., 2017). To ensure high accuracy, the nozzle is generally small and close to the printing bed, which was compatible with much-flowing liquid. This action can reduce the unexpected flow spread.

The features of powder-based method are critical for penetration performance. For instance, the finer particle size of powders delays the penetration of droplets leading to longer penetration time, larger spreading diameter, and lower penetration depth (Xia et al., 2019). The compaction process is also important to improve the smoothness and packing of the powder bed that would affect the 3DPC quality (Shakor et al., 2021). High compaction pressure improves the packing level but may bring cracks at the bottom layers that normally is in the early stage of hydration and does not reach to good strength (Lowke et al., 2022). Therefore, the maximum compact pressure is limited lower than the load capacity of fresh samples (Xia et al., 2019). The influence of particle-bed density on penetration is controlled by many parameters (Talke et al., 2023) including translational speed of roller, compaction height, etc. Many printing parameters of powder-based methods are summarised at Table 2. Different to extrusion-based method, one key

Table 1
Parameters used in extrusion printing.

Extrusion speed	Print speed	Printed filament	Note	Refs.
44 mm/s	44 mm/s	–	–	Rahul et al. (2019)
–	H: 100 mm/s V: 2 mm/s	–	–	Rahul et al. (2022)
–	H: 100 mm/s V: 1.11 mm/s	–	–	Mohan et al. (2021a)
1.5 L/min	H: 50 mm/s V: 10 mm/s	Thickness: 10 mm	–	Bai et al. (2021)
2–29 L/min	80 mm/s	–	–	Vantyghem et al. (2020)
1.35 L/min	50 mm/s	Thickness: 15 mm	<9 layers per print	Xiao et al. (2020)
100 r/min	100 mm/s	Thickness: 25 mm Width: 65 mm	Vibration 50 Hz	Wang et al. (2022a)
–	60 mm/s	Thickness: 10 mm Width: 30 mm	Each layer length: 785 mm	Kruger et al. (2019)
200 r/min	120 mm/s	Thickness: 15 mm Width: 30 mm	Each layer length: 200 mm	Liu et al. (2022a)
5 mm/s	15 mm/s	Thickness: 5 mm	UHPC	Yang et al. (2022a)
1.3 L/min	30 mm/s	Thickness: 10 mm Width: 30 mm	UHPC Time interval: 3 min	Arunothayan et al. (2020)
750 kg/h	169 mm/s	–	–	Ashrafi et al. (2019)
850 kg/h	118 mm/s 157 mm/s	–	Nozzle to bed: 15 mm Various lab temperature and humidity	Ashrafi et al. (2021a)
200 r/min	120 mm/s	Thickness: 18 mm Width: 40 mm	Coarse aggregate <12 mm	Liu et al. (2022b)
133.3 r/min	120 mm/s	Thickness: 10 mm	Nozzle to bed: 20 mm Foam concrete	Liu et al. (2021)
100 g/s	100 mm/s	Thickness: 13 mm	Nozzle to bed: 20 mm ECC concrete	Zhu et al. (2019)
1 L/min	30 mm/s	Thickness: 10 mm	–	Yu et al. (2021)
1.8 L/min	4000 mm/min	Thickness: 15 mm	–	Weng et al. (2019)
5.4 L/min	H: 75 mm/s V: 13 mm/min	–	Nozzle to bed: 24 mm Copper tailings	Ma et al. (2018a)
0.4 L/s	50 mm/s	–	Nozzle to bed: 40 mm Contain coarse aggregate	Xiao et al. (2022)
–	20 mm/s	Thickness: 10 mm	Nozzle to bed: 20 mm RFA	Sun et al. (2022)
0.35 L/s	20 mm/s	Thickness: 10 mm	–	Hao et al. (2022)

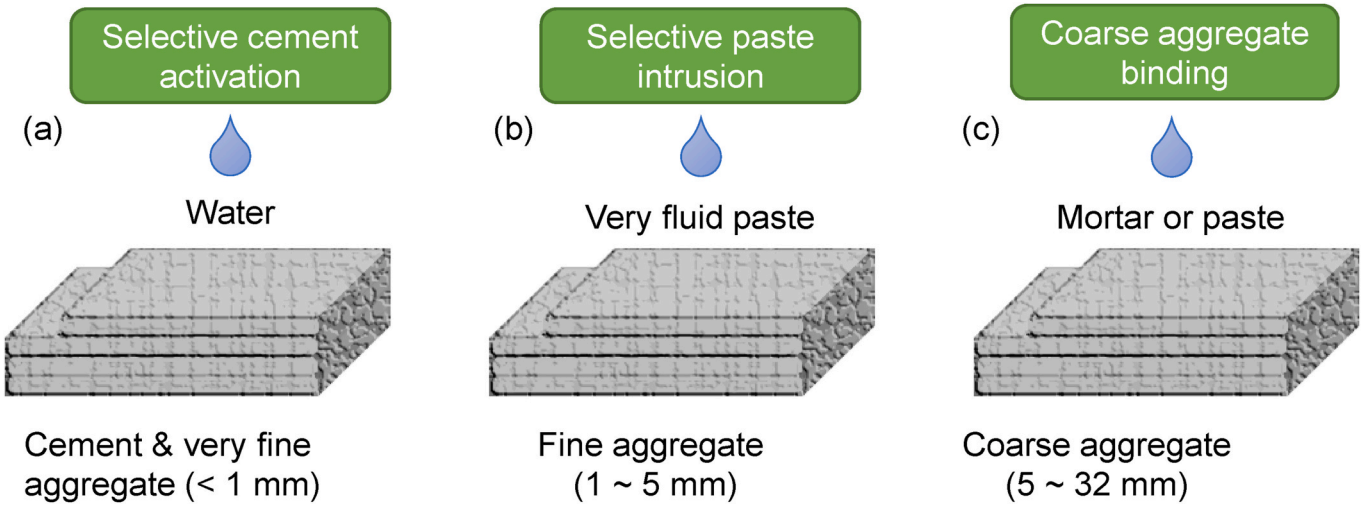

Fig. 5. Main types of powder-based methods in concrete printing (according to (Lowke et al., 2022)).

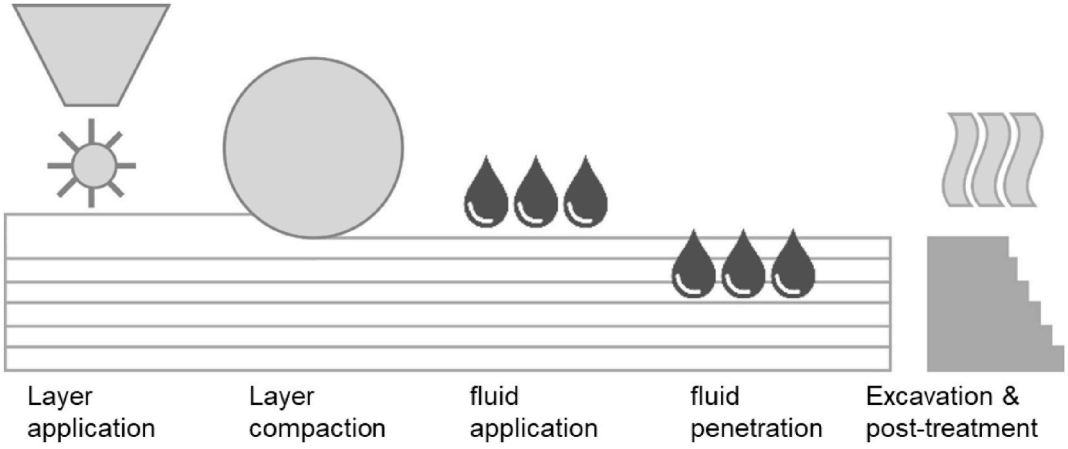

Fig. 6. Sub-processes of powder-based method (Lowke et al., 2022).

Table 2
Parameters used in powder-based printing.

Layer thickness	Nozzle	Liquid part	Powder bed	Injection ratio	Note	Refs.
2.25 mm	Round Ø 0.19 mm	–	–	–	Nozzle to bed: 1.25 mm	Salari et al. (2022)
7 mm	Round Ø 5 mm	Mortar	Coarse aggregate (1.18–7 mm)	–	–	Yu et al., 2020, 2022
3 mm	Round Ø 0.25 mm	Silicate solution	20 wt% metakaolin Silica sand	0.6 μl/mm	Nozzle distance 0.75 mm	Voney et al. (2020)
0.1016 mm	304 nozzles; each drop size: 2.5 pL	–	FA Class F Slag Silica sand	Binder/volume ratio: 0.24 for shell section and 0.12 for core section	Max pressure: 0.9 Pa	Xia et al. (2019)
0.1 mm	HP10 print head	Water and isopropyl alcohol	Cement and fine sand	–	–	Lowke et al. (2020)
1 mm	water-jet print head	Water	Cement, fine sand, methylcellulose ether	–	–	Lowke et al. (2020)
3 mm	–	Paste	Sand <3 mm	–	–	Pierre et al. (2018)
3 mm	Round Ø 2 mm	Paste	Sand: 1–2.2 mm	Nozzle: 2000 mm/min Applied paste: 2.22 cm^3/cm	Nozzle to bed: 15 mm	Weger and Gehlen (2021)

parameter (printing speed) is replaced by the injection ratio. The injection ratio is affected by printing speed but more directly essential to the liquid-to-solid ratio and printing quality.

2.1.3. Main characteristics of extrusion- and powder-based methods

The extrusion-based printing method is suitable for being printed on a plane. However, the cantilever structure and overhanging part challenge the self-supporting ability (Ji et al., 2019; Weng et al., 2019) that is

common for buildings like the roof. Some researchers selected to print components separately to complete a whole building (Weng et al., 2020). The practical solution is essential. From the cases around the world, three kinds of methods are representative of solving this problem. First one is conventional formwork. Xiao et al. (2020) added wood boards to support fresh printed concrete at the top of doors and windows that were removed after concrete hardened. This method connects conventional technology and intelligent construction providing a reliable solution. Nevertheless, this method will delay construction progress. Furthermore, it conflicts with the ideal theory that the 3DPC application can eliminate the requirement for formwork. The second one is a novel toolpath design to complete the roof structure, avoiding the cantilever structure. The interlayer adhesion and self-supporting capability of fresh 3DPC are not strong for cantilevers but accepted for small inclinations. The acceptable overhang is believed to be from −20° to 20° if the material mixing design is appropriate, and Anton et al. (2021) achieved the 3DPC columns with complex geometric shown in Fig. 2(a). Carneau et al. (2020) described it as an adaption from the theory of masonry stacking structure (mutual support from components). 3DPC structures with the whole rooftop were printed without additional process, as shown in Fig. 7(a). Obviously, this method has the architecture constraint that is a compromising option. The final method uses weak 3DPC. Normally, the printed fresh filament is required to be continuous without break because of the weak strength. However, Tay et al. (2019) utilised the discrete filament (filament with obvious breaks and cracks) controlled by printing parameters. The discrete filaments were used to support cantilever structures, as shown in Fig. 7(b). In other words, the discrete filaments filled the part that should be vacant but helpful for supporting the cantilever. The weak mechanical properties of discrete filaments allowed them to be removed easily in the post-process. It is a novel idea to print the cantilever automatically, but the post-process causes additional costs of time, labour, and wasted material (removed filaments).

For powder-based method, the unreactive powder could be good support for printed structure, especially in the early stage (Voney et al., 2020). Shakor et al. (2021) utilised this feature to print specimens with different rotations via the powder-based method, which investigated the anisotropy with various gradients rather than only directions along the axis in most experiments with the extrusion method. Water evaporation is a key reason for the shrinkage and weak strength, similar to conventional concrete in dry curing condition, which is also a serious problem for extrusion-based 3DPC (Ranjbar et al., 2022) especially for onsite extrusion 3DPC due to the lack of formwork cover. Without post-processes, the powder-based method can achieve lower evaporation which means the water is mostly covered by powder and separated from the air (Zuo et al., 2020). For the extrusion-based method, the evaporation from the lateral surface is a problem although the interlayer water could be contained in the same way.

In addition, the commercial powder-based printer, especially for large-scale applications, usually use a row of nozzles to improve efficiency (Xia et al., 2019) that is not widely suitable to entrusion-method. The capability of a single nozzle is normally very small to control the liquid part with high accuracy. This nozzle row configuration poses challenges on the flexibility of printing, which lead to a single linear

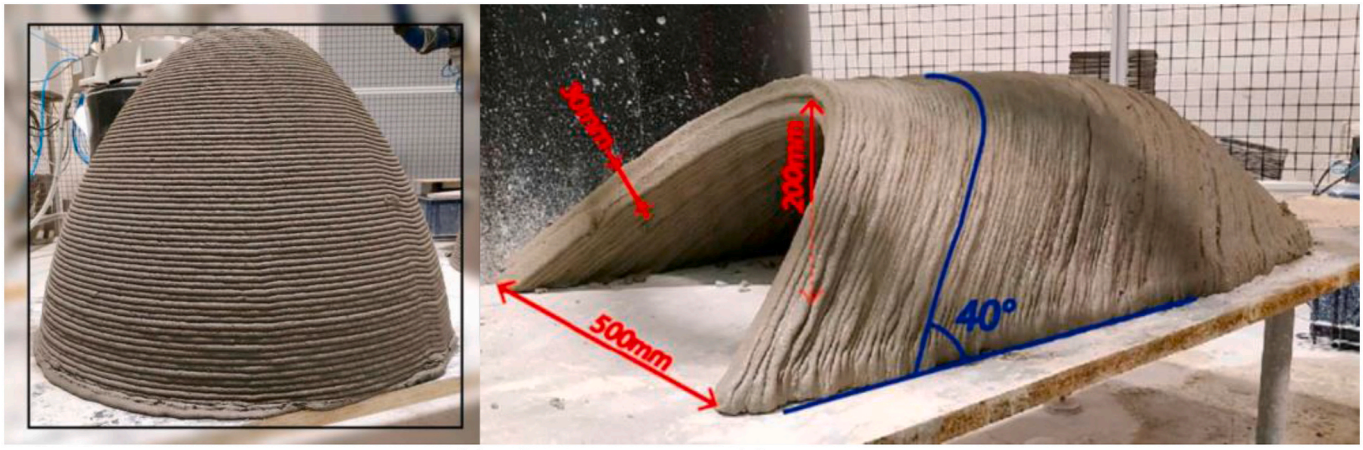

(a) 3DP structures with cover

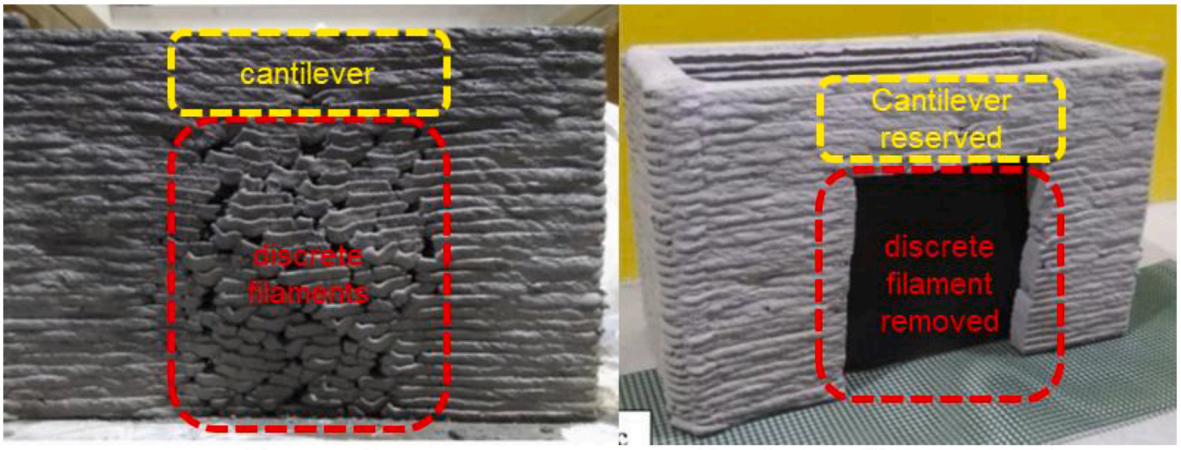

(b) Cantilever structures supported by discrete filaments

Fig. 7. 3DPC structures with whole roof.

printing direction of most powder-based printers. The printing mainly follows X direction. When the nozzle moving on Y direction, the liquid application stop (Feng et al., 2015), as shown in Fig. 8. The powder feeding and rolling direction are able to parallel (Cesaretti et al., 2014) or perpendicular (Shakor et al., 2020a) to the printing direction. Many structures, like circle printing path, are difficult to be completed by this nozzle row configuration.

2.2. Printing equipment and characteristics

A continuous filament with good quality asks appropriate printing parameters as discussed above. For example, the extrusion rate must match printing speed in extrusion-based method (Anton et al., 2021). The completion of optimal printing parameters is controlled by printers. Two main kinds of printers are exhibited and compared. This aims to introduce recently applied printers and give a summary of their characteristics. The modification and development of printers are not discussed in this paper.

2.2.1. 4-DoF (degrees of freedom) gantry

The structure of a 4-DoF gantry is relatively not complex in mechanical structure. The printer frame at Asprone et al. (2018) shows a different shape to a normal gantry but the features are still identical to normal 4-DoF printers. The capabilities of many 4-DoF gantries are summarised in Table 3.

2.2.2. 6-DoF robot

6-DoF robot is another popular type of printer that has a higher degree of freedom. Researchers preferred to use it for complex challenges. Craveiro et al. (2020) developed a printing system based on a 6-axis robotic arm that was able to print functional material with varying pump speed and print head spatial displacement according to predefined material and shape designs. This system consists of whole processes from material preparation to a dynamic extruder. The parameters of many printers are presented in the last rows of Table 3, and the picture illustration is shown in Fig. 9. It is noticeable that the 6-DoF robot generally would not be used in powder-based printing. It is difficult to apply powders from various directions that is the major advantage of the 6-DoF robot. The difficulty is mainly caused by both delivery and application. The plane powder is more reasonable and feasible in a 4-DoF gantry printer.

2.2.3. Features and differences of printers

It is expectable from the name that the 6-DoF robot is more flexible in constructing complex tasks. The printing path of 4-DoF printer is relatively limited, but the simple structure of the gantry enables easy modification and operation design.

The working area is one of the critical problems in the in-situ application for large structures. The gantry printer is relatively easy to scale up while the working area adjustment for robotic printer is more complex. Many systems allow work area extension of robotic printers (Dörfler et al., 2022). Manual relocation may be a solution, but much time, labour, and space are required for movement. The cooperation of several printing platforms could achieve a large structure in less time. Still, the work division is a new problem, considering the effect of the time gap on printing quality. In addition, the integrity of the large part deserves much attention. However, a simple gantry also needs help to build a vast structure because the printing toolpath and speed are difficult to match the setting time of fresh concrete.

2.3. Materials and properties for 3D concrete printing

2.3.1. Extrudability and buildability for extrusion-based 3DPC

Extrudability refers to the ability to extrude the prepared material as filaments while buildability presents the stable shape retaining ability and enough strength for the whole structure's integrity. It is commonly accepted that an acceptable extrudability needs a relatively soft material, but satisfactory buildability needs a rigid one. The contradictory requirements of extrusion and building are presented that primarily rely on hydration performance and microstructure. This could be enhanced by proper additives (Reiter et al., 2020).

Suitable extrusion usually is defined as a smooth surface without cracks and blockage (Hou et al., 2021; Brooks et al., 2022). The extrudability is closely controlled by various factors for flowability. The authors regarded good flowability as the average flow velocity varying from 2.3 to 3.5 mm/s and the expanded diameter ranging from 160 to 210 mm/s. A similar result was reported in (Chen et al., 2020) where the flow spread diameter above 140 mm was provided as a good extrudability. Dong et al. (2022) modified the spread of fresh mortar to around 179 mm for printing UHPC. Wang et al. (2022b) recommended a spread diameter of 150–210 mm in a self-sensing composite. The spread range, conducted according to (EN 1015, 2006), between 135 and 165 mm was defined as adequate flowability (Cuevas et al., 2021). Ma et al. (2022) regarded spreading diameter through the jumping-table test within

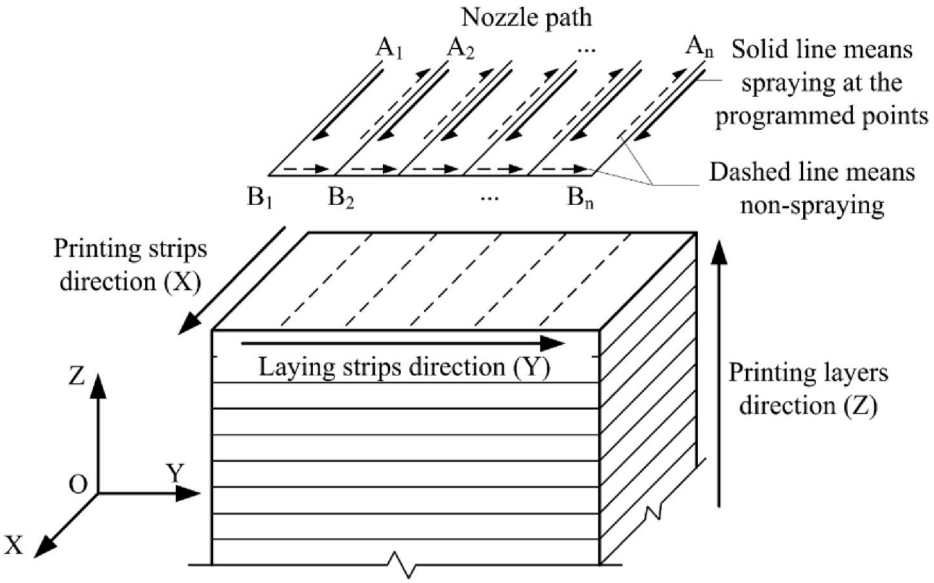

Fig. 8. Printing process and direction (Feng et al., 2015).

Table 3
Parameters of 4-DoF gantry printers.

Extrusion-based					
Frame size (m) Length × width × height	Nozzle diameter (mm)	Printing speed	Extrusion	Note	Refs.
1.1 × 7.2 × 2.9	Rectangular 40 × 13.5 (Chen et al., 2020) Round Ø 15 (Chen et al., 2021)	0–120 mm/s	–	Pipe diameter: 25 mm	Chen et al., 2020, 2021
–	Rectangular 30 × 20	–	–	Pipe diameter: 32 mm	Rahul et al. (2019)
0.5 × 0.39 × 1.1	Rectangular 8 × 30			Nozzle to bed: 24 mm	Ma et al. (2018a)
1.8 × 1.8 × 1.5	Round Ø 30	–	–	–	Bai et al. (2021)
Triangle with sides of 4 Maximum height of 1.5	Round Ø 25	–	–	Pipe diameter: 25 mm	Asprone et al. (2018)
3 × 3 × 4	Round Ø 30	0–120 mm/s	–	–	Xiao et al. (2020)
Extended length × 7.2 × 2.9	–	0–500 mm/s Acceleration: 50–200 mm/s^2	–	–	Ji et al. (2019)
3 × 3 × 3	Round Ø 40	–	–	Vibration of 50 Hz	Wang et al. (2022a)
1.8 × 1.6 × 1.8	Round Ø 30	–	–	–	Arunothayan et al., 2020, 2022
0.75 × 0.75 × 0.5	Rectangular 30 × 30	–	Maximum pressure: 4 kg/cm^2	–	Rahul and Santhanam (2020)
0.6 × 0.6 × 1	Round Ø 15	0–100 mm/s	–	Accuracy of 0.1 mm	Cui et al. (2022)
3.5 × 3.5 × 3	Round Ø 40	–	–	–	Liu et al. (2022b)
1.45 × 1.2 × 0.8	Rectangular 50 × 40 Rectangular 40 × 15	–	Mixing speed: 60 rpm	–	Sikora et al. (2022)
1.8 × 1.6 × 1.8	Round Ø 30	–	–	Pipe long: 3 m	Yu et al. (2021)
1.2 × 1.2 × 1.0	Rectangular 30 × 15	–	–	–	Weng et al. (2019)
	Round Ø 25 (Vantyghem et al., 2020) Rectangular 50 × 20 (Rahul et al., 2022) Rectangular 40 × 10 (Mohan et al., 2021a)		2–29 L/min (Vantyghem et al., 2020) 0–105 L/min (Rahul et al., 2022) 0–29 L/min (Mohan et al., 2021a)	Pipe diameter: 25 mm Maximum pumping pressure: 40 bar (Mohan et al., 2021a)	(Vantyghem et al., 2020; Rahul et al., 2022; Mohan et al., 2021a)
	Round Ø 25	–	–		Craveiro et al. (2020)

Powder-based				
Frame size (m) Length × width × height	Nozzle diameter (mm)	Powder feeding	Note	Refs.
0.185 × 0.236 × 0.132	304 nozzles	build speed of 2–4 layers/min	–	Xia et al. (2019)
0.23 × 0.254 × 0.203	–	21 rectangular holes 4.5 × 1 mm in Powder container	–	Shakor et al. (2020a)
0.356 × 0.254 × 0.203	Nozzle HP 4810A 11	–	Roller: diameter of 22 mm and length of 356 mm	Lowke et al. (2022)
0.305 × 0.375 × 0.25	Round Ø 2	–	–	Weger and Gehlen (2021)
0.2 × 0.25 × 0.2	HP10 print head	–	Base layer: 1 mm	Lowke et al. (2020)
0.45 × 0.6 × 0.5	Water-jet print head	–	Water pressure: 0.3–0.8 bar Nozzle moving 8000–17000 mm/min	Lowke et al. (2020)

174–210 mm as preferred. Zou et al. (2021) found that the fluidity of mortar between 168 and 201 mm was suitable for extrusion and printing with a smooth surface. The flowability of extruded materials in (Zhang et al., 2018) was much higher, among which the group with the lowest flowability of 190 mm presented the best buildability although all samples could be extruded. Zhang et al. (2019a) selected a higher value, 192.5–269 mm, and successfully printed a large-scale structure.

The criteria index varies. The slump result can also be an index. The slump range of 120–130 mm was regarded to have the best printing effect in (Ji et al., 2019), where coarse aggregates were used. The fresh concrete presented good extrudability, although coarse aggregates and continuous grading provided the lowest flowability (Bai et al., 2021). Chen et al. (2020) introduced extrusion pressure as an index to evaluate extrusion ability. This method was applied with constant printing speed and material flow rate, forming an interrelated whole. Rahul et al. (2019) proposed the yield stress should be 1.5–2.5 kPa to keep good

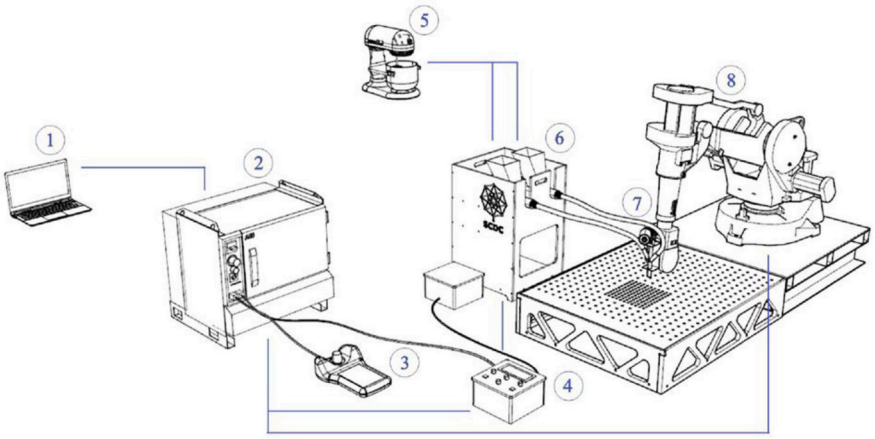

1. Computer for designing & robot code;
2. Robot controller model;
3. Robot tech pendant for hand control;
4. Pumps tech pendant for hand control;
5. Mixer for materials preparation;
6. Concrete pumps;
7. Dynamic mixer/extruder nozzle
8. Robotic arm.

(a) Extrusion (Craveiroa et al. in Portugal)

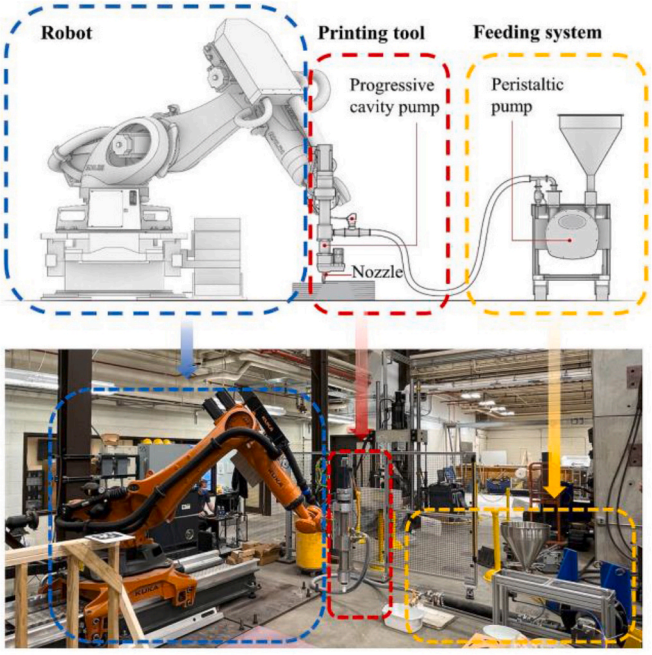

(b) Extrusion (Zhou et al. in USA)

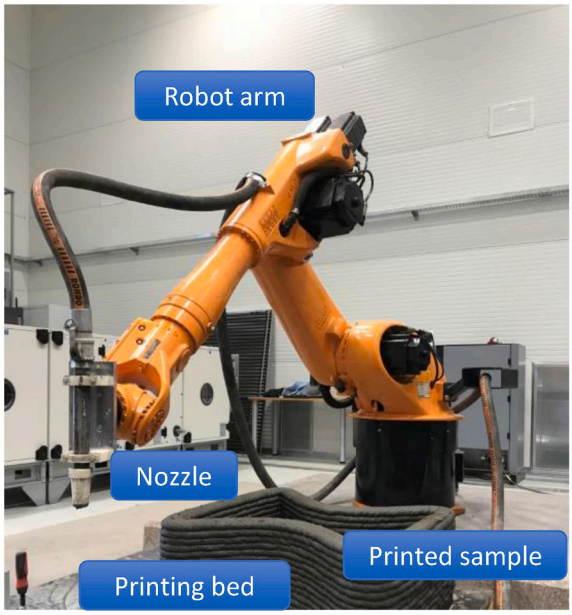

(c) Extrusion (Vespalec et al. in Czech)

Fig. 9. 6-DoF robot printing (a. whole process illustration; b. printing system; c. 6-DoF robot).

extrudability. Mohan et al. (2021b) believed the dynamic yield stress was prominent for extrudability while the static yield stress was critical for printability. This index was affected by secondary mixing that brought higher fluidity (by ~ 6%) but lower yield stress (by ~ 3%) (Xiao et al., 2020).

Notably, the definition of optimal extrusion property is related to the printing machine. The mortar with low flowability and slump can still be extruded well because of the larger nozzle and higher motor torque (Zhang et al., 2022a). The congestion and printing interruptions likely occurred when the spread diameter was lower than 192 mm in the experiment (Zhang et al., 2019a) with a nozzle diameter of 20 mm.

The extrudability and buildability occurred in extrusion printing while powder-based printing emphasized the sufficient combination and reaction of powder bed and printed ink. Yu et al. (2020) stated that the target penetration of the binder should be one to two times the aggregate layer height. The maximum yield stress value that enabled full penetration in this experiment was 69 Pa. The uncompleted penetration that caused voids around aggregates was found, which was the main reason for lower density and weaker strength.

2.3.2. Mix design and optimisation for extrusion-based 3DPC

The printing method, printer system, and property of raw material are interconnected for quality printing (Xiao et al., 2020). For instance, the inter-layer time interval is affected by the open time of the material and structural shape. Open time is a period in which the fresh concrete has enough pumpability and inter-layer adhesion. The definition of perfect design of any part separately is biased although the research on every part was meaningful. Portland cement is a widely used binder but there are a lot of other choices. Researchers have conducted various experiments using different binders and found that some of them were very promising.

(1) Use of special cementitious material

Mohan et al. (2021a) used calcium sulfoaluminate cement (CSA) as the binder. An important feature of CSA cement was the fast reaction and short open time that affected the printing process. Borax and sodium gluconate were added to prolong the open time. The results from both the conduction calorimeter and ultrasonic P-wave transmission measurements proved the retardation. The open time was prolonged by

borax to the same value as the counterparts Portland cement, and was more effective when the amount of retarder was 0.5 wt% of the binder. However, higher viscosity caused pumping pressure loss and weaker early-stage strength. Therefore, cement was partially replaced by limestone (LF) that presented similar viscosity with Portland cement sample and 20% higher yield stress when 30 wt% of LF cooperated with borax. The strength was good with LF addition on the seventh day although it was still low on the first day. The sample, including CSA, borax, and 20 wt% LF, showed the best buildability with a critical height of 382 mm, 25 mm higher than the Portland cement counterpart. Perrot et al. (2018) provided the possible application of earth-based material by adding alginate in 3DP and believed in its ability for wall production. The alginate improved its strength as a fast binder and was also an eco-friendly material. The printed sample reached 1.7 MPa, while pores were found on the cross-section.

(2) Use of supplementary cementitious materials

The replacement of cement by GGBFS, SF (Geng et al., 2020), FA, micro-silica (Nerella et al., 2019), etc., is one way to modify the concrete properties and reduce pollution of cement consumption. A multitype of cementitious materials could be incorporated to achieve better performance (Zhang et al., 2018). The modification is mainly on fresh concrete properties, like flowability and cement hydration. To achieve optimal early strength, Panda et al. (2019a) added sodium sulphate as an activator in the binder containing 60% FA. Zhang et al. (2018) designed a mix with SF and nanoclay and significantly improved the component's quality. SF accelerated hydration reaction while nanoclay enhanced thixotropy. SF was also able to raise the initial yield stress and thixotropy but the benefit of modified hydration on layer bond was observable only if the rheological properties were desired (Geng et al., 2020). Geng et al. (2020) also proved the significance of sufficient interface humidity on bond quality. Chen et al. (2021) substituted cement with calcined clay (CC) containing around half metakaolin and LF to reduce cement consumption. The CC and LF with high specific surface area caused a significant reduction of water film thickness, further leading to a lower flow rate and weaker compressive strength. The substitution proportion was proposed as less than 75% to ensure the basic strength although B90 group showed better buildability. Further, the CC with different metakaolin content replaced LF (Chen et al., 2019). It was proved that the high-content CC accelerated the initial hydration and contributed to shorter initial setting time and higher compressive strength. The reason may be the enhanced nucleation and facilitated microstructure due to the increased tiny particles of metakaolin.

(3) Effect of aggregate content

The aggregate is the foundation for concrete strength while the aggregate content is critical. Zhang et al. (2019b) found a positive linear relationship between the flowability of cement paste and the optimum aggregate content under the same buildability. This result was still valid when the binder raw material and water content changed. The excess slurry theory also explained the rheological behaviour, which showed a linear relationship with optimal sand content. Mohan et al. (2021b) analysed the effect of aggregate content with a maximum particle size of 2 mm. The aggregate-to-binder ratio increased from 1.0 to 1.8 with the same viscosity modifying admixture (VMA) dosage of 0.1%. The dosage of superplasticizer (SP) was varied to maintain the flow value in the 50–60% range. It was expected that the plastic viscosity and yield stress would increase due to the lower binder content. The SP showed different compensating efficiency on yield stress and plastic viscosity, which explained different increments in yield stress by 23% and plastic viscosity by 153% with increasing aggregate content. This further made lower lubrication performance affecting extrudability. The range of aggregate-to-binder ratio was lower as 0.93, 1 and 1.1 in (Wang et al., 2022a) with a constant coarse-to-fine aggregates ratio of 1.87 and the additives in all groups. Higher yield stress and plastic viscosity were observed and worse extrudability occurred at 0.93 group, which presented that more binder gave higher flowability and deformation leading to poor buildability. The deformation was less with a lower ratio of 1. However, a much lower binder failed to wrap aggregates and fill voids leading to obvious surface defects. In the study (Kondepudi et al., 2022), the effect of aggregate content was investigated based on 3DP geopolymer concrete. The same trend of increasing yield stress and viscosity with decreasing binder was observed, and the researchers pointed out the linear relation in viscosity and the nonlinear relation in yield stress. The increasing aggregate content filled up more space and demanded less paste. Sufficient paste was still required to coat the surfaces of aggregate particles and overcome frictions between the aggregate particles.

(4) Effect of coarse aggregate

Considering the printing resolution and capacity of printers, the application of coarse aggregate in 3DPC starts after fine aggregate since it is still extremely important for real structures. Zhang et al. (2022a) regarded mortar and coarse aggregate as two phases in the mixing design while adding coarse aggregate was based on equivalent volume. The mortar was lubricating layer coating coarse aggregates in this two-phase model, and the lubricating layer became thinner with more coarse aggregates, leading to a reduction in flowability by over 50% and much stiffer in the slump test with 30–35 vol% replacement. The most significant growth happened on static yield stress (over a hundred times) followed by dynamic yield stress and plastic viscosity with an exponential relationship with replacement rate. The relationship between rheological property and the coarse aggregate fraction was described by the Coussot model and the Krieger-Dougherty model. The plastic viscosity was generally lower than dozens Pa·s of mortar but much higher for concrete with coarse aggregate that required much higher pumping pressure (Zhang et al., 2022a). Therefore, the plastic viscosity was one critical index that cooperated for printability evaluation when coarse aggregates were used. In addition to aggregate content, the effect of coarse aggregate was also investigated in (Wang et al., 2022a) with a size range of 5–10 mm. The calculated mortar thickness decreased from 4.43 mm to 2.42 mm with higher coarse aggregates from 50% to 80% (weight percentage of whole aggregates), leading to higher static yield stress, dynamic yield stress and plastic viscosity. The enhancement efficiency of coarse aggregates on compressive strength in 3DPC was higher than that in cast concrete although 3DPC was still weaker than cast concrete. It was noticeable that the anisotropic characteristic was remarkably eliminated by increasing coarse aggregates after curing for 28 days. The coarse aggregates could be redistributed during printing and penetrated the layer surface, enhancing the binding strength and reducing anisotropy. The homogeneousness of pores and aggregates was significant to mechanical performance (Vespalec et al., 2020). The effect of coarse aggregates was important to crack propagation although it was inconsiderable to uniaxial tension strength.

(5) Unconventional aggregates incorporation

The research focused on unconventional aggregates also gave exciting ideas. Tao et al. (2022a) used river and manufactured sands in close particle distribution but with different shape features. The river sand had higher sphericity with an aspect ratio of 1.19 while that of manufactured sand was 1.57. This feature could be presented by packing fraction. The packing fraction decreased from 0.59 to 0.52 with the manufactured sand ratio increased from 0 to 100 vol%. A significant increase in elastic module and a moderate increase in yield stress were observed. It was noticeable that the critical printing height showed an excellent linear relationship with the packing fraction. Li et al. (2021) investigated the feasibility of seawater and coral sand concrete for 3D printing. All mixing plans showed good extrusion ability under the fixed

sand-to-binder ratio of 1 and water-to-binder ratio of 0.24 or 0.26, where a water reducer was used to modify the flow diameter between 150 and 200 mm. The seawater was collected from Victoria Harbor in Hong Kong. The flexural strength of 9.10 MPa and compressive strength of 89.56 MPa were satisfactory. Tao et al. (2022b) introduced perforated fly ash cenosphere (PFAC) that was FAC processed by acid to replace sand partially. PFAC was hollow particles with perforation that was able to carry internal curing water. The rheological properties were reduced because the released water from PFAC under shear stress increased the lubrication. A remarkable advantage on autogenous shrinkage strain reached 81% with 15 vol% PFAC (replaced sand). Furthermore, the hollow morphology of PFAC with low strength and elastic modulus was prone to cause weaker concrete, but the internal curing effect compensated for this drawback, which led to similar compressive strength to the reference specimen. The analyses mentioned above are summarised in Table 4, and many 3DPC mix plans with suitable applications are shown in Table 5.

2.3.3. Materials and properties of powder-based 3DPC

The difference in the printing process poses different challenges, so powder-based 3DPC requires specific research. For powder-based 3DPC, Shakor et al., 2017, 2021 proposed a powder mixture consisting of cement, 5 wt% fine sand, and 1% fibre. The cement was mixed with 32.2 wt% OPC and 67.8 wt% calcium aluminate cement. The humectant was added to water as the dropped liquid. The printed specimen achieved a compressive strength of 37.88 MPa. The printing accuracy was as good as commercial powders (like ZP150, mainly consisting of plaster, vinyl polymer and carbohydrate) in the experiment. Feng et al. (2015) used this commercial powder and ZB60 (containing humectant and water) to study the mechanical performance of the powder-based 3DPC. The printed specimen showed apparent anisotropic behaviour. The flexural strength of the Z direction (perpendicular to the printing plane) was still the highest, similar to that of extrusion-based 3DPC. Compressive strength and elastic modulus showed different features. Apart from the weaker layer bond, the highest compression strength and elastic modulus were observed for cubes when the load was applied to the X direction (printer head travel direction), which was also proved in (Nematollahi et al., 2019). It was explained by the shorter time interval between strips than between layers. Salari et al. (2022) introduced eco-friendly magnesium oxychloride cement in binder jetting 3DPC. The pulverised magnesium oxide was mixed with fine aggregates as the powder bed and magnesium chloride hexahydrate was dissolved in a deionized water solution as the liquid binder. The reaction was going with the printing process.

It was noticeable that the relatively higher water ratio provided higher compressive strength and low apparent porosity in many powder-based 3DPC experiments (Shakor et al., 2017, 2020a, 2021), which was the opposite performance compared to conventional concrete. Lowke et al. (2020) explained that the higher water content likely facilitated the water penetration into layers and the bond improvement. A powder bed with very fine packing was better for accuracy than coarse particles. Seven times enhancement was achieved due to increasing the water/-cement ratio from 0.15 to 0.4, although the penetration tunnels were more extensive. In water-jetting applications, this change in water content generally caused a rougher surface of the powder bed that supported a higher layer bond (Lowke et al., 2022). However, higher water content was normally related to lower printing accuracy (Lowke et al., 2020, 2022). Therefore, it should be in a reasonable range based on research.

The SPI method had effective control on the hydration compared to SCA that significantly affected the mechanical performance. To ensure penetration performance, the Technical University of Munich group conducted an investigation via experiment and model analyses (Pierre et al., 2018). The specimen achieved 78 MPa of compressive strength on the 7th day after printing with good paste penetration (Weger and Gehlen, 2021). The 3DPC products also showed excellent ability to resist freeze-thaw, carbonation, and chloride migration, although the raw materials were conventional.

The benefits of coarse aggregate on strength were widely recognised and proved in powder-based printing. The compressive strength of 3DPC containing larger sand (d90 = 450 μm) showed higher strength (16 MPa) than that containing smaller sand (d90 = 140 μm, 6 MPa), probably because the aggregates larger than the layer thickness created mechanical interlocking between the layers (Lowke et al., 2020). Yu et al. (2020) believed binder jetting was preferred for coarse application considering the size limitation of extrusion. The proportion of coarse aggregates reached nearly 40% in a modified binder jetting printing sample where the paste was extruded on the coarse aggregate. The same group replaced paste with mortar and fine sand (176 μm) (Yu et al., 2022). To achieve full penetration, the strength and the plastic viscosity of the mortar were critical. A decreased sand/cement ratio (from 0.45 to 0.4) could increase the strength of the printed specimen, but a further low ratio (from 0.4 to 0.35) penetration significantly and produced more voids, which caused lower strength of the printed specimen. Many applications are shown in Table 6.

2.3.4. Roles of additives and fibres for enhancement

Many additives are used to improve extrudability, buildability, and strength (like superplasticizer, early strength agents, cellulose ethers as water-retaining agents, VMA, fibres, etc.) For example, extruded filaments were short or blocked if the superplasticizer was less than 0.10%.

Table 4
Effects of various modification on extrusion-based 3DPC.

Method		Effects	Refs.
Different cementitious material	CSA	Shorter open time can be prolonged by borax and sodium gluconate; higher viscosity can be modified by LF.	(Mohan et al., 2021a; Zhang et al., 2018; Perrot et al., 2018; Nerella et al., 2019; Panda et al., 2019a; Chen et al., 2019)
	Earth-based material	Good possibility with the binder of alginate; all material is sustainable	
	Calcined clay	Accelerated the initial hydration; shorter initial setting time; lower flow rate; different constitution shows the different effect on strength	
		SF raises initial yield stress and thixotropy; nanoclay enhance thixotropy	
Aggregate content	More aggregate causes low flowability, low deformation, high yield stress, and plastic viscosity; aggregate content shows linear relation in viscosity and nonlinear relation in yield stress; an optimal ratio of binder-to-aggregate is required to satisfy both extrudability and buildability; sufficient binder should overcome frictions between aggregates		(Wang et al., 2022a; Mohan et al., 2021b; Zhang et al., 2019b; Kondepudi et al., 2022)
Different aggregates incorporation	More coarse aggregates improve stiffness for buildability but increase pumping pressure; anisotropy could be eliminated due to cross-layer coarse aggregate		(Wang et al., 2022a; Vespalec et al., 2020; Zhang et al., 2022a; Tao et al., 2022a, 2022b; Li et al., 2021)
	Critical printing height shows a good linear relationship with the packing fraction of aggregate; 3DPC containing seawater and coral sand concrete shows good strength; perforated fly ash cenosphere reduces rheological because of leaked water		

Table 5
Mix designs of extrusion-based 3DPC.

Binder	Aggregate	Water	Additive	Printer	Refs.
Cement: 579 kg with 6–20% LF extender; FA Class F: 165 kg; SF: 83 kg	1167 kg Size <4.75 mm	261 kg (0.30)	SP: 1.48 wt%	4 DoF Extrusion	Kruger et al. (2020)
Cement: 663 kg; FA Class F: 165.7 kg	497.2 kg Quartz powder (0.01–0.1 mm) 372.9 kg Quartz sand 1 (0.1–1 mm) 372.9 kg Quartz sand 2 (0.1–1 mm)	265.2 kg (0.32)	PP fibers length of 12 mm and thickness of 40 μm nominal dosage of 1.8 kg/m^3 control plastic shrinkage PCE-based SP: 0.83 kg (0.10 wt%)	4 DoF Extrusion	Rahul et al. (2019)
Cement: 800 kg; SF: 200 kg	No. RA kg CP kg DS kg Mix-CG 630 780 690 Mix-IG 630 0 1470 Mix-OG 630 1470 0	500 kg (0.5)	Basalt fiber: 0.4 vol % SP: Mix-CG 17 kg; Mix-IG 18 kg; Mix-OG 15 kg	4 DoF Extrusion	Bai et al. (2021)
Cement: 34.7 kg	Dried sand: 51.1 kg	13.2 kg (0.38)	Water retention agent: 1 wt%	6 DoF Extrusion	Vantyghem et al. (2020)
No. PC CC LF B0 100 0 0 B45 55 30 15 B75 25 50 25 B90 10 60 30	Sand: 150 kg	0.3 (0.3)	PCE-based SP 1.5 wt% and 2 wt % hydroxypropyl methylcellulose (HPMC)-based (VMA) 0.24 wt %	4 DoF Extrusion	Chen et al. (2021)
Cement: 621 kg	Sand (<2 mm): 1241 kg	227 kg (0.37)	PCE-based SP: 1.5 wt%	Extrusion	Van Der Putten et al. (2020)
Cement: 1000 kg	Sand: 1000 kg	350 kg (0.35)	HPMC: 0.128 wt% PCE-based SP: 0.083 wt% Nano-clay: 0.498 wt%	4 DoF Extrusion	Xiao et al. (2020)
	Sand: 750 kg and RFA: 250 kg	385 kg (0.385)	HPMC: 0.125 wt% PCE-based SP: 0.075 wt% Nano-clay: 0.461 wt%		
Cement: 1000 kg	RAF: 1000 kg	485 kg (0.485)	HPMC: 1.28 kg Sodium gluconate: 1.2 kg SP: 1.1 kg or SP: 1.2 kg with 10 kg fiber Fiber: PE length of 12 mm	4 DoF Extrusion	Xiao et al. (2021)
Cement: 1000 kg	RAF: 1000 kg	485 kg (0.485)	HPMC: 1.28 kg SP: 0.83 kg Sodium gluconate: 0, 0.3, 0.6, 1.2 kg	4 DoF Extrusion	Zou et al. (2021)
Cement: 45 kg Ground slag: 30 kg Silica fume: 25 kg	Sand: 100 kg	237 kg (0.237)	Water retention agent: 1.14 wt% Clay: 1.5 wt%	Extrusion	Liu et al. (2022c)
Cement: 100 kg	Coarse aggregate: 362 kg Sand: 320 kg	0.66 kg (0.66)	Accelerator: 3–5 wt% FA: 2.4 wt%	4 DoF Extrusion	Ji et al. (2019)
Cement: 100 kg	Coarse aggregate: 340 kg Sand: 298 kg	0.60 kg (0.60)	Accelerator: 3–5 wt% FA: 3.2 wt%	4 DoF Extrusion	Ji et al. (2019)
Cement: 713.1 kg; Silica fume: 79.2 kg	Sand: 1290 kg Coarse aggregate: varying volume incorporation in the mortar (up to 25 vol% is acceptable)	237.7 kg (0.30)	PCE-based SP: 0.65, 1.20, 1.50 wt%	4 DoF Extrusion	Zhang et al. (2022a)
Cement: 756.4 kg; FA Class F: 48.8 kg; SF: 24.4 kg	Sand: 1290 kg (<3 mm)	(0.30)	PCE-based SP: 2.93 kg; early strength agent: 146.4 kg; cellulose ethers: 0.29 kg; PVA fiber: 0.6 kg	4 DoF Extrusion	Liu et al. (2022a)
Cement: 750 kg; FA: 165 kg; SF: 165 kg	Sand: 1080 kg (0.1–0.4 mm)	154 kg (0.14)	PCE-based SP: 10 kg; Cellulose water retention agent: 1.08 kg; NCC: 24 kg; Steel fiber: 78 kg (6 mm)	4 DoF Extrusion	Yang et al. (2022a)
Cement: 700 kg; SF: 300 kg	Sand: 400 kg fine (D_{50}: 176 μm), 300 kg medium (D_{50}: 498 μm), 300 kg coarse (D_{50}: 840 μm)	160 kg (0.16)	Water retention agent: 1.5 wt%; VMA (Sodium carboxymethyl cellulose): 0.3 wt%; Steel fiber: 2 vol %;	4 DoF Extrusion	Arunothayan et al. (2020)
Cement: 588.5 kg; FA: 83.4 kg; SF: 196.2 kg; ground slag: 112.8 kg	Sand: 750.3 kg (<1 mm); Crumb rubber: 132.4 kg (<2.36 mm)	294.2 kg (0.3)	Midrange water reducer: 14.7 kg (1.5 wt%); Clay: 27.5 kg	Extrusion	Liu et al. (2022d)
Cement: 232 kg; FA Class C: 166 kg; SF: 83 kg	Sand: 1146 kg (0.16–0.2)	232 kg (0.28)	Polycarboxylic acid high performance water reducing agent (HWRA): 8.29 kg; cellulose viscosity agent: 0.4 wt%	Extrusion	Lee et al. (2019)
Cement: 815 kg	Sand: 1222 kg (<2 mm)	258 kg (0.35)	PCE-based SP: 4.24 kg; methyl cellulose-based VMA: 0.81 kg	6 DoF Extrusion	Mohan et al. (2021a)
CSA cement: 652 kg Limestone: 163 kg	Sand: 1222 kg (<2 mm)	258 kg (0.35)	PCE-based SP: 2.85 kg; methyl cellulose-based VMA: 0.81 kg; retarder (borax or gluconate) 4.05 kg	6 DoF Extrusion	Mohan et al. (2021a)
Cement: 70 kg; FA Class F: 20 kg; SF: 10 kg	Sand: 17 kg (<2 mm)	49.5 kg (0.495)		4 DoF Extrusion	Tay et al. (2019)
Cement: 506.25 kg	Fine sand: 607.5 kg (150–425 μm)	200 kg (0.39)	SP: 2.531 kg; Retarder 2.7 L; Accelerator 3.375 L; E6-Glass fibre: 11.14 kg (1 wt% of cement + sand)	6 DoF Extrusion	Shakor et al. (2020b)
Cement: 444 kg; FA: 96.6 kg; micro-silica: 41.4 kg	Fine aggregates: 870 kg (0.15–4.75 mm) Coarse aggregates: 588 kg (5–10 mm)	210 kg (0.36)	PCE-based SP: 0.53 kg; HPMC: 1.11 kg; Retarder (sodium gluconate): 0.11 kg	4 DoF Extrusion	Ji et al. (2022)

(*continued on next page*)

Table 5 (*continued*)

Binder	Aggregate	Water	Additive	Printer	Refs.
Portland-LF cement (80–94% clinker and 6–20% LF replacement): 562 kg; FA Class F: 162 kg; micro-silica: 81.4 kg	Granite sand: 1144 kg (<4.75 mm)	256 kg (0.32)	polycarboxylate polymer-based SP: 4.9 kg (0.6%); HPMC-based VMA: 2.4 kg (0.3%); PP microfibre: 9.1 kg (6 mm)	4 DoF Extrusion	van den Heever et al. (2022a)
Cement: 660 kg; FA Class F: 165 kg;	Quartz sand: 1237 kg (<1 mm)	264 kg (0.32)	PCE-based SP: 0.08%; HPMC: 0.25 kg; PP fibre: 1.8 kg (12 mm)	Extrusion	Rahul and Santhanam (2020)
Cement: 612 kg; FA Class F: 153 kg;	Quartz sand: 938 kg (<1 mm) Expanded clay: 210 kg (<10 mm)	245 kg (0.32)	PCE-based SP: 0.08%; HPMC: 0.25 kg; PP fibre: 1.8 kg (12 mm)	Extrusion	Rahul and Santhanam (2020)
Cement: 800 kg; Silica fume: 200 kg	Coral sand: 1000 kg (0.1–3 mm)	240 kg (0.24)	Water reducer: 1.8 % (100% seawater was used)	Extrusion	Li et al. (2021)
Cement: 800 kg; Silica fume: 200 kg	Coral sand: 1000 kg (0.1–3 mm)	260 kg (0.26)	Water reducer: 1.6 % (100% seawater was used)	Extrusion	Li et al. (2021)
Cement: 864 kg; SF: 18 kg; Nanoclay: 18 kg	Fine aggregate: 900 kg (<1 mm)	315 kg (0.35)	Polycarboxylate based high water reducer: 0.26% Thicker agent: 0.0125%	4 DoF Extrusion	Zhang et al. (2018)
Cement: 400 kg; Metakaolin: 100 kg	Fine aggregate: 1130 kg (<4 mm) Coarse aggregate: 300 kg (4–8 mm)	258 kg (0.52)	Liquid solidification accelerator: 3 kg	6 DoF Extrusion	Vespalec et al. (2020)
Cement: 45 kg; Calcined clay: 33.3 kg; Limestone powder: 16.7 kg; SF: 5 kg	Sand: 121.5 kg; PFAC: 11.2 kg	48 kg (0.48)	Polycarboxylate based high water reducer: 0.4%	4 DoF Extrusion	Tao et al. (2022b)
Cement:331 kg; Calcined clay: 166 kg (40–50% metakaolin); Calcined clay: 165 kg (90% metakaolin); Limestone filler: 166 kg	Sand: 1242 kg (<2 mm)	248 kg (0.3)	PCE-based SP: 17 kg HPMC-based VMA: 2 kg	Extrusion	Chen et al. (2019)
Cement: 580 kg; FA: 166 kg; SF: 83 kg	Sand: 1270 kg (<2 mm)	200 kg (0.24)	Polycarboxylate SP: 2.0 kg	4 DoF Extrusion	Sikora et al. (2022)
Cement: 38 kg; FA: 60 kg; SF: 2 kg	Sand: 83 kg (<1.18 mm)	30 kg (0.3)	Attapulgite nanoclay: 0.5 wt% Sodium sulphate: 3 wt%	4 DoF Extrusion	Panda et al. (2019a)
Cement: 90 kg; SF: 10 kg	Sand: 47 kg (mean size: 500 μm) Sand: 70 kg (mean size: 840 μm) Sand: 88 kg (mean size: 170 μm)	28 kg (0.28)	carboxylic ether polymer hyperplasticiser and VMA	Extrusion	Marchment and Sanjayan (2020)
Cement: 80 kg; FA: 10 kg; SF: 10 kg	Sand: 35 kg (mean size: 840 μm) Sand: 21 kg (mean size: 498 μm) Sand: 44 kg (mean size: 176 μm)	31 kg (0.31)	PCE-based SP: 0.8 wt% Retarder: 0.2 wt%	4 DoF Extrusion	Yu et al. (2021)
Cement: 70 kg; FA: 20 kg; SF: 10 kg	Sand: 84 kg (mean size: 378 μm) Copper tailings: 36 kg (mean size: 246 μm)	27 kg (0.27)	Polycarboxylate-based SP: 0.29 wt% PP fibre: 1.2 kg/m^3	4 DoF Extrusion	Ma et al. (2018a)

The bottom filament was compressed by 2 mm when the dosage reached 0.11% (Rahul et al., 2019). The yield stress was more sensitive to SP than plastic viscosity (Zhang et al., 2022a). This part will discuss these materials with novel performance or methods in 3DPC rather than conventional concrete modification.

The impacts of additives on printing enhancement are different but caused mainly by modified rheological properties, which have been investigated for a very long period. Cuevas et al. (2021) introduced the expanded thermoplastic microsphere (ETM) to adjust rheological, thermal and mechanical properties. The increased flowability was explained by many reasons. The packing density was increased due to fine ETM particles, leading to lower water needs, and the pre-wetted ETM brought over water, which caused the higher flow. Another reason was the spherical shape lubricating the paste. Then, the reduced yield stress and increased plastic viscosity enabled the paste to have better buildability, while the yield stress was calculated based on a mini-slump test proposed by Tan et al. (2017). The delay in setting time was remarkable because non-reactive ETM slowed the hydration. However, these characteristics made lower strength due to weaker bonds and lower thermal conductivity due to lower density. Shao et al. (2022) introduced special capsules carrying additives for 3DPC. Higher flowability was required for extrusion but lower flowability was good for buildability. The polyethylene-glycol (PEG) capsules (melting point of 55.1 °C and diameter of 2–4 mm) incorporated accelerator and VMA before mixing. During the extrusion process, a microwave treatment was employed to stimulate graphite powders (also incorporated in capsules). The increasing temperature made capsules melt and core material release, which increased static yield stress (shear rate of 0.01 rpm last for 180 s), dynamic yield stress (0.01 rpm–100 rpm in 60 s and then decreases), and plastic viscosity of the printed fresh concrete. The flowability dramatically decreased by 60 mm with 3% capsules after microwave treatment, which was satisfactory for buildability and maintained high flowability before extrusion. The enhancement of nanoclay on yield stress was evident at a low constant rotational speed of 0.1 (rpm) (Rahul et al., 2019). Ramakrishnan et al. (2021) used nanoclay to change the yield stress and viscosity that enabled the fresh hollow-core filament to be strong enough to support the self-weight of overhanging parts. Panda et al. (2019a) proved the enhancement in stiffness, nearly double Young's modulus, which contributing to successful 20 layers compared to the reference group with 13 layers.

The modification of rheological properties mainly improves the performance during printing, while the enhancement of printed and hardened 3DPC is the next key point. The incorporation of fibres showed excellent performance in 3DPC for mechanics improvement. Li et al. (2021) investigated different types of fibres (glass and basalt) with similar properties: same length of 12 mm; close diameter of 14–19 μm and 13 μm; roughly equal tensile strength of 1700 MPa and 1500 MPa; and similar elastic modulus of 72 GPa and 60 GPa. Both fibres decreased the flowability, but it could be compensated by a water reducer to reach a reasonable value. The expected enhancement in flexural strength was observed with the addition of fibre because of crack bridging ability, but much more fibres over 0.01 wt% caused more voids, leading to weaker performance. However, the effects on compressive strength were always adverse, and basalt fibre was slightly more sensitive. Shakor et al.

Table 6
Applications of powder-based 3DPC.

Applied liquid	Powder-bed mix	Note	Machine	Refs.
Water and humectant	32.2 wt% OPC and 67.8 wt% calcium aluminate cement; Fine sand contributed 5 wt%; E6-Glass fibre	SCA	4 DoF Powder	Shakor et al. (2021)
Water and humectant	32.2 wt% OPC and 67.8 wt% calcium aluminate cement; Fine sand contributed 5 wt%; 4.5% lithium carbonate	SCA	4 DoF Powder	Shakor et al. (2020a)
Deionized water; $MgCl_2.6H_2O$; rice starch	Porous glass 60.8 wt%; MgO 36.5 wt%; methylcellulose 1.5 wt %; H_3PO_4 1.2 wt%	SCA	4 DoF Powder	Salari et al. (2022)
90 vol% deionized water and 10 vol% isopropyl alcohol (ratio to cement 0.16–0.36)	Cement with Mayenite; fine sand (volume rate to cement: 60/40);	SCA	4 DoF Powder	Lowke et al. (2020)
Deionized water (ratio to cement: 0.3, 0.4, 0.5)	Cement; methylcellulose ether;	SCA	4 DoF Powder	Lowke et al. (2020)
Cement; water; PCE-SP	Fine sand (0.7–1.2 mm); medium sand (1.0–2.2 mm); coarse sand (2.0–3.2 mm)	SPI	4 DoF Powder	Pierre et al. (2018)
Cement; water (0.3); PCE-SP (0.72 wt%)	Sand (1.0–2.2 mm)	SPI	4 DoF Powder	Weger and Gehlen (2021)
Cement: 100 kg; Silica fume: 5 kg; PCE-based SP: 0.3 kg; VMA: 1 kg; water: 35 kg (0.35)	Bed: Coarse aggregate: <7 mm	CAB	4 DoF Powder	Yu et al. (2020)
Cement: 907 kg; PCE-based SP: 1.36 kg; Retarder: 3.63 kg; water: 363 kg (0.4)	Sand: 907 kg Bed: Coarse aggregate: <7 mm	CAB	4 DoF Powder	Yu et al. (2022)

(2020b) used E6-Glass fibre with a length of 6 mm and a diameter of 100 μm. The fresh concrete was extruded from a round nozzle with a diameter of 20 mm. The image analyses illustrated that the alignment appearance was significant, where 80% of fibres were oriented with the filament. Shakor et al. (2021) also introduced this fibre in powder-based 3DPC, with significant compressive and flexural strength enhancement. However, 70% of fibres were oriented perpendicularly with the printing direction but paralleled the rolling direction, a remarkable feature of the powder-based method.

The benefits of fibres were not limited to mechanical reasons. Weng et al. (2019) revealed the decreasing ability of concrete in elevated temperatures up to 800 °C and the benefit of PVA fibre on fireproof for 3DPC. The PVA fibres caused microcracks because of expansion, melting, and evaporation in high temperatures that accelerated water evaporation. Jiang et al. (2022) took nanosilica as additives cooperating with PP fibres to modify printing performance. The ultra-high specific surface of NS and interlocking among PP fibres increased the water demand, leading to lower fluidity. The NS attached to the fibre surface further raised the water absorption of fibre and expanded the water contact angle, which increased the hydrophilicity and enhanced the fibre bond. The shorter setting time accounted for accelerated hydration due to the nucleation and pozzolanic reaction of NS and higher porosity. Besides improved printability, ductile failure and decreased compressive, the observation of lower strength anisotropy was imperative, attributed to the filling and reaction of NS modified the pore structure and improved fibre bond, causing better layer performance.

However, the effects were only sometimes positive. Al-Qutaifi et al. (2018) investigated hooked-end steel and PP fibres in 3DP geopolymer concrete. Fibre incorporation reduced the workability and led to the possible nozzle blockage. The critical problem was weaker bond strength because of the uneven surface and lower adherence. This negative performance on bond strength was kept even though the dosage of fibres was reduced. The effects are summarised in Table 7.

2.3.5. Technical improvement method

The manufacturing process of 3DPC is more refined than cast concrete, allowing the critical part (layer bond) to get specific treatment and improvement. Wang et al. (2020) proposed a polymer-modified mortar to improve the bond strength. With the epoxy resin of 8%, over 2.2 times enhancement was found in tensile and shearing bonds. The electrostatic interaction between the epoxy resin and calcium ions counteracted the most effects of water molecules. Hosseini et al. (2019) introduced a polymer that consisted of 99% sulphur and 1% black carbon to enhance the layer bond strength. The polymer mixed with fine sand became the connecting layer that brought remarkably higher tensile strength in bending tests from 0.75 to 1.5 MPa. The electrostatic forces between calcium ions and the negatively-charged SBC polymer contributed to this improvement.

The lack of reinforcement is one primary reason of weaker mechanical performance that should be overcome, while reinforced 3DPC is effective. Gebhard et al. (2022) manually placed steel bars or high-strength wires in the middle point of the specimen. The bar was well covered by concrete with few defects. The bond strength was quite good based on the mixing design at ETHZ with reduced initial yield strength, smaller aggregate size, and higher compressive strength. The large scatter was observed when the bar was parallel to the filament, and it was larger for the steel wires application. Hojati et al. (2022) introduced twisted 4-point barbed wires as reinforcement manually placed along the filaments, as shown in Fig. 10(a). The bond strength between concrete and wires was strong enough and no slip was observed. The potential slip caused by the printing process was overcome. The much higher moment capacity proved the feasibility and advantage of this novel wire as reinforcement. Wang et al. (2021a) designed U nails, shown in Fig. 10(b), to improve the layer bond. The nail was vertical, which crossed several layers (4 layers in this experiment). Nails were inserted in every second layer with a staggered layout to improve the integrity further. A gratifying enhancement was proved on interlayer shear strength with up to 120% and interlayer tensile strength with up to 37.8%–61.8%. Perrot et al. (2020) manually embedded nails with a length of 30 mm, shown in Fig. 10(c), in the layer with a thickness of 10 mm. The different orientations of nails (vertical, 45° inclined toward the sample centre or toward opposite direction). The bending force was improved by up to 50% in samples with the inclined and crossed nail configuration. Although rusted nails provided minor enhancement, the maximum force was unaffected, and the durability was a potential problem. The nail with thread improved a coarse surface and higher bond strength. Therefore, Cao et al. (2022) analysed six types of nails, as shown in Fig. 10(d). FL nails provided the highest pull-out strength with the highest ratio of thread length to thread depth. Although both insertion and screwing planting methods were useful, the screwing operation was better for mortar filling in the thread gaps. The layer bond strength was improved by 38.2% thanks to one planted ST nail, and the splitting strength was enhanced by 60.8% due to multi-FL nails. Hass et al. (2022) ground nail thread, shown in Fig. 10(e), and incorporated it in 3DPC with two mixing designs. The bond strength improvement was remarkable, although higher void content was found, especially near nails. In this experiment, the pull-out strength was governed by the mortar's compressive strength. The grinding process showed little influence on the result. The nail insertion had a relaxed requirement for time but all samples in this experiment were processed within 200 min after printing. Marchment and Sanjayan (2020) embedded steel wire mesh with an average diameter of 0.5 mm and an aperture of approximately 6 × 6 mm shown in Fig. 10(f). The enhancement of flexural strength achieved 170%–290%.

Table 7
Effects of additives and fibres on 3DPC.

Additives	Amount	Results	Refs.
PCE-based SP	0.65 wt%, 1.2 wt%, and 1.5 wt% of binder	Static yield stress from 2.60 kPa to 0.22 kPa–0.13 kPa Dynamic yield stress from 1.12 kPa to 0.15 kPa–0.09 kPa Plastic viscosity from 60.4 Pa s to 53.2 Pa s to 50.7 Pa s (Rheometer 69 mm * D69 mm)	Zhang et al. (2022a)
Nanoclay	0.2 wt% of cement 900	Yield stress from 4.25 kPa to 9.0 kPa (at 30 min) (Six-blade rheometer 127 mm * D127 mm)	Ramakrishnan et al. (2021)
Attapulgite nanoclay	0.5 wt% of binder	Young's modulus increased from 0.03 to 0.06 MPa Critical layer increased from 13 to 20 Stronger early strength	Panda et al. (2019a)
Nanoclay (Attapulgite clay 1.5–2 μm)	0.1%, 0.2% and 0.3% of binder	Yield stress increased with nanoclay Superplasticizer was increased from 0.10% to 0.11%, 0.12% and 0.13% to keep stable yield stress Variability factor decreased from 4.5 to 1.2 kPa with 0.1% nanoclay in robustness test (Four-blade rheometer 24 mm * D12 mm)	Rahul et al. (2019)
VMA	0.1% of binder	Yield stress increased Superplasticizer was increased from 0.10% to 0.18% to keep stable yield stress Variability factor decreased from 4.5 to 0.5 kPa (Four-blade rheometer 24 mm * D12 mm)	Rahul et al. (2019)
VMA	VMA: 0, 0.14, 0.24, 0.48 wt% of binder refer 1.2VAM, 2VMA, 4VMA groups	Flow consistency increased Extrusion pressure increased from less 10 to - 23 Bar Water retention increased Green strength (within 4 h) increased significantly in 2VMA but no further enhancement at 4VMA 7-day strength decreased but much strength was retained in 2VMA The cement hydration was retarded	Chen et al. (2020)
Capsules with VMA and accelerator (microwave treatment)	3 wt% and 5 wt % of binder	Flowability from 160 mm to less than 100 mm (3%) Static yield stress from ~20 Pa to ~ 45 Pa (3%) Static yield stress from ~18 Pa to ~ 130 Pa (5%) Dynamic yield stress from ~25 Pa to ~ 65 Pa (3%) Dynamic yield stress from ~35 Pa to ~ 140 Pa (5%) Plastic viscosity from ~0.32 Pa s to ~ 0.6 Pa s (3%) Plastic viscosity from ~0.35 Pa s to ~ 0.8 Pa s (5%) (Before and after microwave treatment) (Four-blade rheometer 60 mm * D30 mm)	Shao et al. (2022)
Silica fume	10% of binder	Yield stress increased Superplasticizer was increased from 0.10% to 0.17% to keep stable yield stress Variability factor decreased from 4.5 to 0.9 kPa (Four-blade rheometer 24 mm * D12 mm)	Rahul et al. (2019)
ETM	0 wt% and 0.03 wt% of binder	Higher flowability (different effectiveness while highest enhancement occurred in G50 group) Longer setting time by 1–4 h Plastic viscosity increased by 66%, 25%, and 31% Lower thermal conductivity by 36% Lower strength Yield stress reduced by 18%, 1%, and 26% (based on mini-slump test)	Cuevas et al. (2021)
Sodium gluconate	0, 0.03, 0.06, 0.12 wt% of binder	Higher fluidity Longer printing window of 20, 30, 40, 60 min Weaker stiffening process	Zou et al. (2021)
PE fiber	0 wt% and 1 wt % of binder	Large and uniform deformation over maximum bearing capacity Higher maximum deformation Fail from brittle to ductile in compression and tension Mechanical properties enhanced Obvious anisotropy	Xiao et al. (2021)
Steel fibre	2 vol% of binder	Compressive strength increased by ~ 20 MPa Modulus of rupture increased by ~ 23 MPa Layer bond increased from 2.7 MPa to 5.1 MPa Flexural toughness increased by ~ 70 J/mm^2 Apparent porosity increased by ~ 5%	Arunothayan et al. (2020)
E6-Glass fibre	1 wt% of cement + sand	Compressive strength increased by ~ 108 % Flexural strength increased by ~ 68 % Printable end-effector velocity region up to 60.32 mm/s	Shakor et al. (2020b)

(*continued on next page*)

Table 7 (*continued*)

Additives	Amount	Results	Refs.
E6-Glass fibre	1 wt%	Compressive strength increased by ~ 58 % (optimal) Flexural strength increased by ~ 46 % (optimal)	Shakor et al. (2021)
Glass fibre	varied from 0.000 to 0.020% with intervals of 0.005%	Lower flowability Flexural strength increased from 9.1 up to 10.75 MPa Compressive strength decreased from 89.56 up to 87.22 MPa	Li et al. (2021)
Basalt fibre	varied from 0.000 to 0.020% with intervals of 0.005%	Lower flowability Flexural strength increased from 9.1 up to 9.24 MPa Compressive strength decreased from 89.56 up to 69.89 MPa	Li et al. (2021)
NS PP fibre	1 wt % of binder 0.2 wt% of binder	Reduced anisotropy on compressive strength by 64% Shorter setting time Reduced slump by 69% Lower deformation by 46% Weaker compressive strength Higher collops height	Jiang et al. (2022)

Reinforced concrete had proved its dominant advantage in most applications, but the automation progress needed to catch up. Although the fibre addition enhanced mechanical properties, the advantages of reinforced concrete still cannot be replaced (Gebhard et al., 2021). The difference between reinforcement steel and concrete on material and structure posed big challenges. Wang et al. (2021a) designed the equipment to automatically embed the nails, as shown in Fig. 11(a), and the overlapped layout was also adapted in (Marchment and Sanjayan, 2020). Classen et al. (2020) designed a novel printing process to assemble segmented reinforcement steel automatically, as shown in Fig. 11(b). A welding unit ran ahead of the concrete extrusion to fabricate reinforcement bars (10–100 cm adapted to layer thickness and printing speed) coated by concrete. This method improved the whole strength and integrity but reduced the printing speed. Lim et al. (2018) implemented a gear-driven steel cable extruder quipped to the nozzle. The cable was embedded with filament during printing. The bending loading capability of geopolymer concrete with fibres was further enhanced. Mechtcherine et al. (2020) designed a spool system to implement carbon wire reinforcement along the filaments. The fibre went through mineral suspension before incorporation with filaments. An outstanding enhancement was achieved on flexural strength of 38% in 40 mm × 40 mm and 238% in 20 mm × 25 mm cross-section. A similar spool design was introduced in (Marchment and Sanjayan, 2020) and cooperated with a custom-designed nozzle to embed mesh reinforcement as shown in Fig. 11(c).

The incorporation of reinforcement structure was based on the conventional theory for cast concrete achieved by the modified method, where the compatibility showed higher challenges. In computational modelling, the void between concrete and rebar may be reduced by decreasing the nozzle-rebar distance, speed ratio, geometric ratio and modified concrete with higher yield stress and lower plastic viscosity (Mollah et al., 2023). However, it was still difficult to omit the voids in complex structures. One of the major benefits of 3DPC was the highly controllable shape that was utilised to enhance layer strength. An interlocking plan as shown in Fig. 12 was tested to improve interlayer adhesion (Zareiyan and Khoshnevis, 2017). The bond strength was investigated by compressive tests and splitting tests. The force loading was parallel with the direction of layers. The tongue with a depth of 0.5″ presented the best enhancement, where 13% and 26% improvements were found in the compressive and splitting tests. The larger contact surface of layers contributed to this progress. Further, a deeper tongue did not raise the strength value. Voids and bad contact were aggravated, leading weaker layer bond that was shown in Fig. 12. This type of interlock was presented as π-type by Wang et al. (2021b), who used binder to connect concrete blocks. The results for self-locking structure could be adopted. According to the test of compression-shear and compression-splitting, the V-type showed optimal tensile and shear strength (others are I-type, π-type and S-type) with excellent bonding performance. The bonding materials had valuable effects on the bonding quality that asked for further research in compatible interlock structures with different concrete properties.

2.4. Characteristics of 3DPC

2.4.1. Benefits on construction and environment

3DPC was commonly believed to be efficient, and the reasons were various, as shown in Fig. 13. The elimination of formwork was a key reason for the contribution of 3DPC, especially for custom-designed shapes. Still, this effectiveness was lower in the condition of mass production in the same shape. Muñoz et al. (2021) proved the lower environmental impact of 3DPC in all the environmental indicators for one structural pillar. The reduction of greenhouse gas reached 38%. The advantages of 3DPC on the environment were offset in mass production that was close to the cast method performance. In a building with a vertical green wall that was partly printed (He et al., 2020), the energy consumption of air conditioners dropped by 11.20% in summer and 9.12% in a year. The lower insulation contributed by the 3DP design promoted heat dissipation through the living wall. In (Alhumayani et al., 2020), the impact of 3DPC on the environment was lower than half compared to the conventional method, which was mainly caused by less reinforcing steel and concrete.

In the research on a bathroom unit structure, the main parts were printed via the extrusion 3DP method. Results showed a significant reduction in cost (by 25.4%), CO_2 emission (85.9%), energy consumption (by 87.1%), and total weight (26.2%) (Weng et al., 2020). These benefits were caused by higher labour productivity (by 48.1%) as well as less material consumption due to the optimal inner structure that was enabled by the flexibility of 3D printing. Ramakrishnan et al. (2021) improved this feature by designing a special nozzle to print hollow-core filaments. Ebrahimi et al. (2022) investigated the impact of calcium sulfoaluminate cement and magnesium oxide cement, to replace Portland cement, in a 3DP building located in San Diego. Based on the mixing plan and analysing conditions in this experiment, most negative environmental impacts were alleviated by around 60% and 20%. However, worse performances of stratospheric ozone depletion, human carcinogenic toxicity, fossil resource scarcity and water consumption were observed, especially the high toxicity. 3DP geopolymer concrete was generally regarded as environmentally friendly. The lower waste generation was still proven, although the raw material source may lead to a higher environmental burden (Yao et al., 2020; Craveiro et al., 2017).

Anyway, it was accepted that the high efficiency of 3DPC on material, labour, and pollution generation in certain conditions (Vantyghem et al., 2020). Higher printing resolution was essential to build complex structures. Excellent construction ability and environmental protection were in complex structures (Agustí-Juan et al., 2017), but Kuzmenko et al. (2022) revealed that climate change depended much on spatial resolution. That required the resolution not be limitlessly increased. The impacts of robotic arm size and printing head velocity were relevantly weak. However, 3DPC structure was not perfect in economy and environment. In regular structures, the cost of labour and formwork became less important, but the higher cement content of 3DPC may be the critical problem. That finally led to higher total costs (Han et al., 2021).

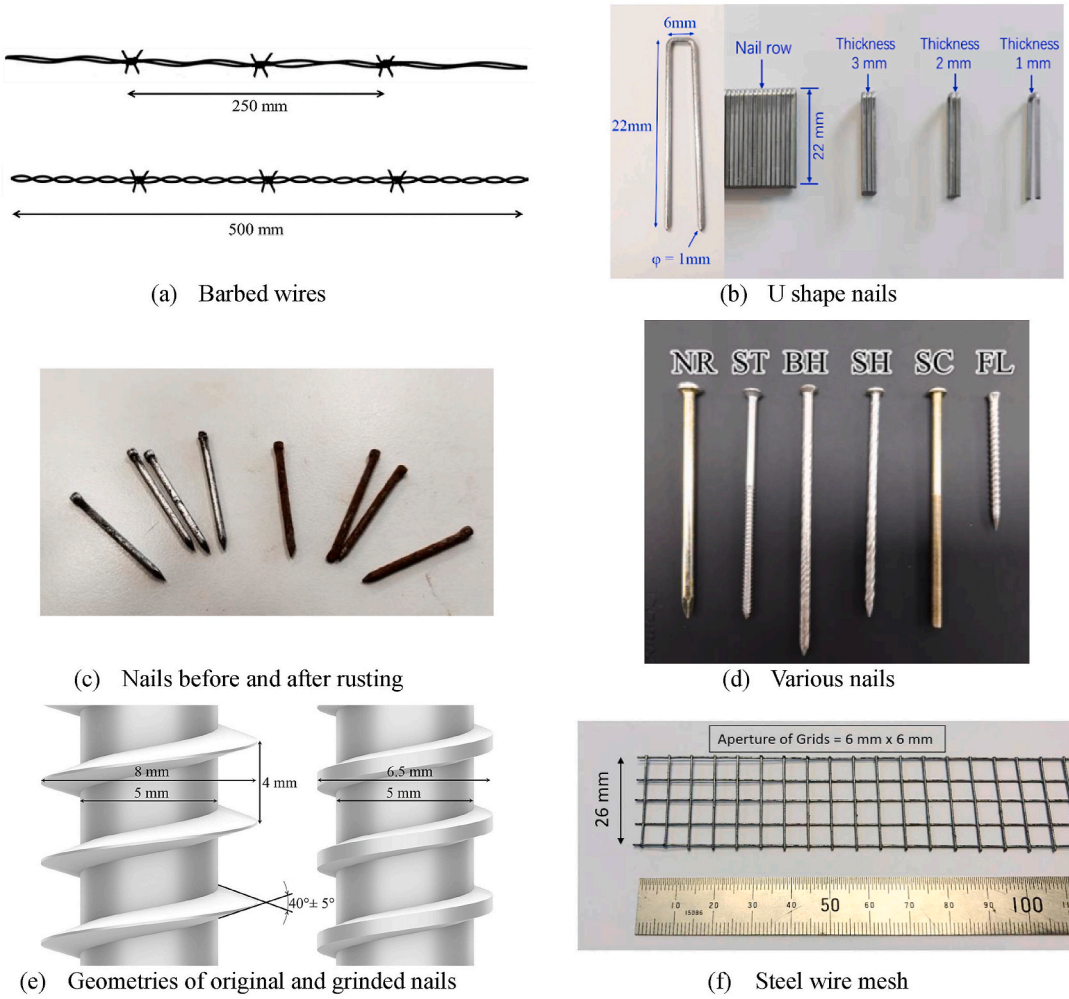

Fig. 10. Designed reinforcements in extruded 3DPC.

2.4.2. *Mechanical property*

The weaker strength was commonly prevalent in 3DPC. The reduction of compressive strength was 16–25 % in (Ji et al., 2019) and 8.3–28.5% in (Yu et al., 2020) where coarse aggregates were used. It reached 40% for compressive strength and 50–53% for flexural in (Rahul et al., 2022). This reduction may occur at all ages (Sikora et al., 2022). This phenomenon was not unvarying. Panda et al. (2017) found a higher compressive strength - 2% in Y (printing direction), although the results of the X and Z (vertical) directions were weaker.

The strength reduction mostly contributed to the worse bond quality and low aggregate ratio. The printing process caused the former, which also led to the anisotropic mechanical ability and microstructure. The anisotropy of water penetration (Zhang et al., 2022b) was a representative phenomenon further expressed by aggravated chloride penetration. The more cracks and higher porosity were the primary reasons; and the longer interlayer time interval worsened this problem (Van Der Putten et al., 2020). The latter was limited by printer limitation, especially for coarse aggregates, and caused high cement consumption (Chen et al., 2021). The coarse aggregate posed challenges to printing accuracy, successful extrusion, cement quality, etc. That was the meaning of the presented works on coarse aggregates.

2.4.3. *Microstructure property*

Inner porosity was typical in concrete, but 3DPC showed different features. In an experiment based on extrusion fibre-reinforced 3DPC (van den Heever et al., 2022a), the total porosity proportion was increased from - 6.5% to - 10% by printing methods like printing parameters and mixing design. The porosity increased slightly by 1.1% in (Kruger et al., 2021). However, the printing process affected the shape of voids significantly. The intralayer voids elongated with the larger dimension in the printing direction compared with the spherical shape in cast concrete. The aspect ratio range of 3DPC was 1.5–2.5 while that was 1.0–2.0 of cast concrete in (Wang et al., 2022a). The method to qualify the homogeneity based on superficial cross-sectional photography was believed to be inaccurate. It was found in (Liu et al., 2022a) that the pore shape was irregular but the stress concentration was easily found at the corners of elongated ellipsoidal pores. Pores larger than 0.5 mm were concentrated at the interlayer location, which dominantly caused weaker interlayer strength (Yu et al., 2021). The pores of all samples showed right-skewed log-normal distributions when the general size range was 0.06–1.2 mm and the cast sample showed more pores in the range of <0.16 mm and >1.2 mm. Extrusion pressure broke large pores into smaller voids and pressed pores smaller than 0.16 mm together. Sikora et al. (2022) proved the different pore size distribution, but the influence on water absorption, freezing and thawing, and high-temperature exposure resistance were limited. Zhang et al. (2022b) also proved faster water penetration in 3DPC than cast concrete due to the interlayer voids and the anisotropy on anti-water penetration was observed. One difference occurred in 3DPC under freezing and thawing testing when the interlayer delamination was found, which was also related to the weak bond. A different regulation was observed on nanoscale (Yu et al., 2021). The average pore diameter increased from 43 nm to 257.9 nm in printed specimens that was explained by the easier moisture loss, which could cause more capillary pores. The avoidance of

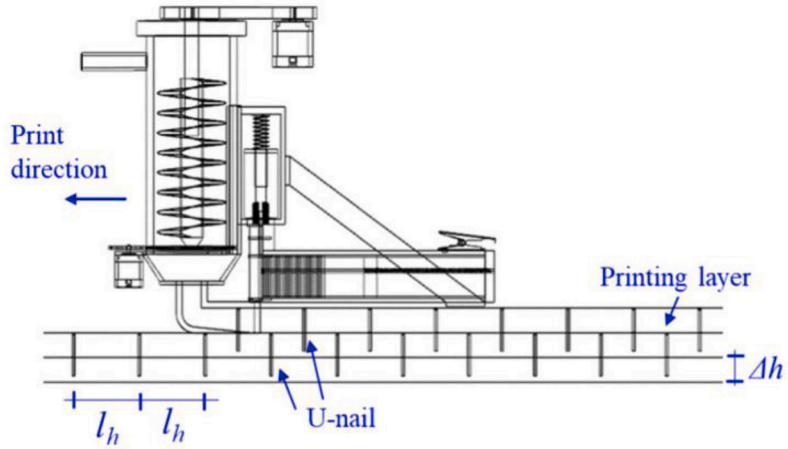

(a) U-nail insertion system during the printing process

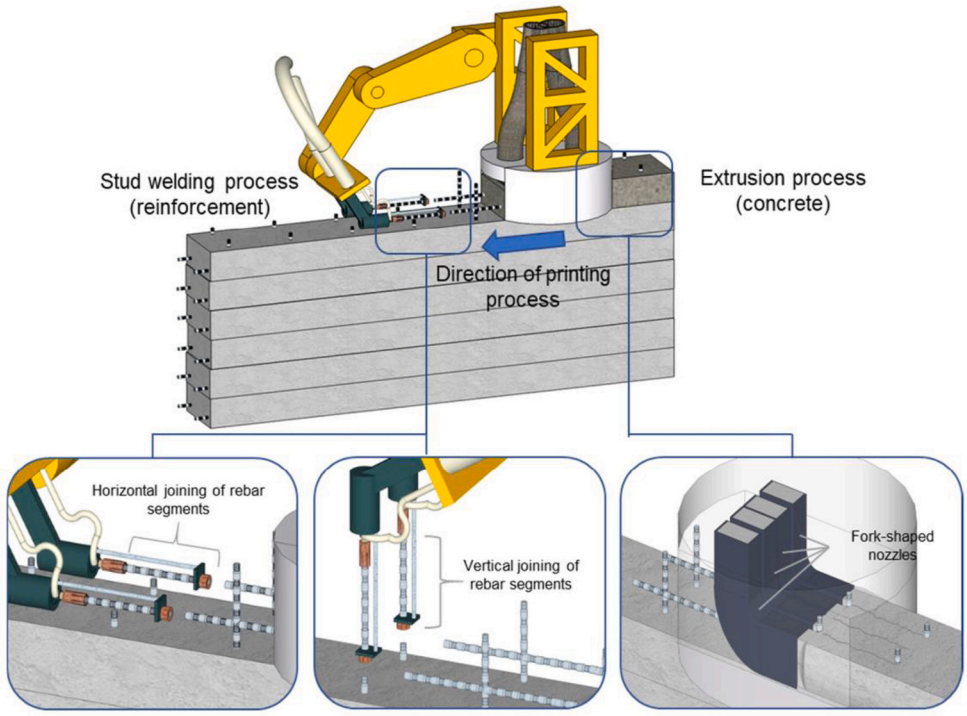

(b) Printing process of segmented reinforcement steel

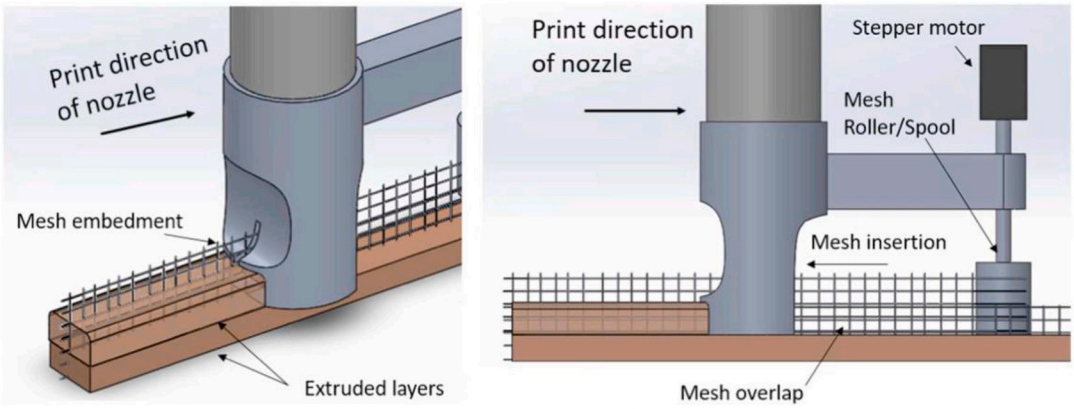

(c) Printing process of steel wire mesh

Fig. 11. Automatic printing process for reinforcement.

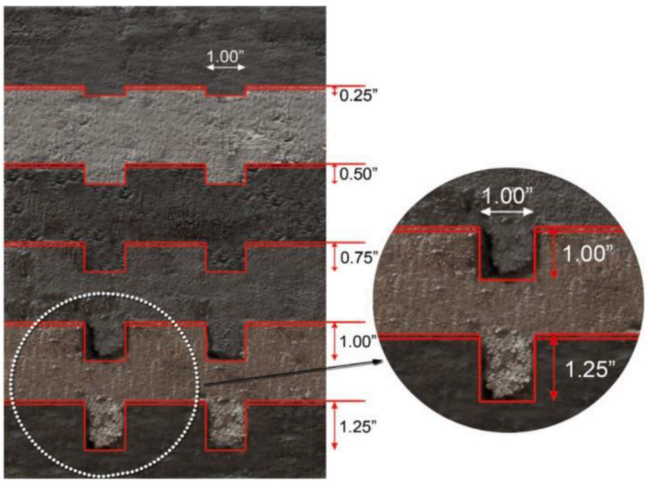

Fig. 12. Shape and size of interlocking (Zareiyan and Khoshnevis, 2017).

various mixing designs showed different sensitivity to the production process (Hass et al., 2022)

The pore shape, size, and number closely revealed mechanical performance. With longer curing time, smaller size and fewer pores led to stronger concrete. However, Lee et al. (2019) showed that there was no direct relation between pore volume and each pore that could cause defects. The reasons for voids in 3DPC were multifarious (Yu et al., 2021; van den Heever et al., 2022a). Yu et al. (2021) believed the lack of formwork leading to rapid water loss and the lack of vibration leaving air bubbles were important reasons for the higher porosity. Wang et al. (2022a) assembled a vibration motor with the container and proved the benefit of vibration on less air voids.

3. 3DPC modelling from design to property

3.1. 3DP design

3.1.1. Design of printing path

The model to design the printing path was critical for 3DPC but little useful for cast concrete. The commercial software was supportive like Slicer software to generate G-Code and define printing paths (Vlachakis et al., 2020). Much work was required to bridge the gap to optimal. Revising the slicing procedure method was necessary to generate printing paths, so many factors and suggestions were considered, including continuous path, staggered joint, and impacts of nozzle size (Xiao et al., 2020). The path design was much more complex for large structures mainly consisting of various geometric shapes, and the difficulty was increased considering the time-dependent properties of fresh concrete (Toklu et al., 2020). Wan et al. (2022) proposed a transfinite mapping method to design the path for continuous and zero-gap manufacturing of various free-form models. Anton et al. (2021) introduced complexity evaluation to analyse the geometric challenge of printing path design. The more directly critical step was toolpath generation. Ashrafi et al. (2022) proposed a set of processes to decompose a building into parts, then into layers, and finally into heads and toolpaths. This algorithm was based on shape grammar implemented in Grasshopper for Rhino. This improvement contributed to shape accuracy and geometric integrity enabling the 3DPC sample to show less deviation with design and less possible collapse. The modified toolpath also compensated for the deformation caused by material stability and polish shape precision (Ashrafi et al., 2021b). For instance, more beads for each layer enlarged the time interval allowing a stronger base to support the following layer and much that showed less deformation, when the time interval reached 33.9 s there was no observed deformation (Ashrafi et al., 2021a).

3.1.2. Design of printed components with material properties

The material properties cannot be neglected. Kruger et al. (2020) utilised a probabilistic design model to improve the accuracy by eliminating the disturbance from the non-determinacy of material property. Craveiroa et al. (Craveiro et al., 2017) designed a computational tool to maximise the superiority of 3DPC. Various material compositions were defined based on voxel determination tailored for specific requirements. 3DPC made the model possible effectively that benefited the reduction of material waste and CO_2 emissions. Vantyghem et al. (2020) used topology optimisation based on 2D square finite elements and transformed the result to 3D by Fusion 360 Autodesk. The response under various loading conditions was investigated using 3D finite element analysis to improve reliability and define the material requirement. This method supported the design of a post-tensioned concrete girder with a span of 4 m. The girder was subdivided into several parts that reduced the printing difficulty and enhanced quality. The printing path was generated by Grasshopper visual script.

3.2. Evaluation of 3DPC

3.2.1. Fresh 3DPC properties

3DPC had structural challenges compared to cast concrete that required a modified evaluation method. The structure varied in different cases where model analysing was more effective than laboratory specimen-based testing. The Mohr-Coulomb criterion was prominent among the developed models. It was believed that the Mohr-Coulomb

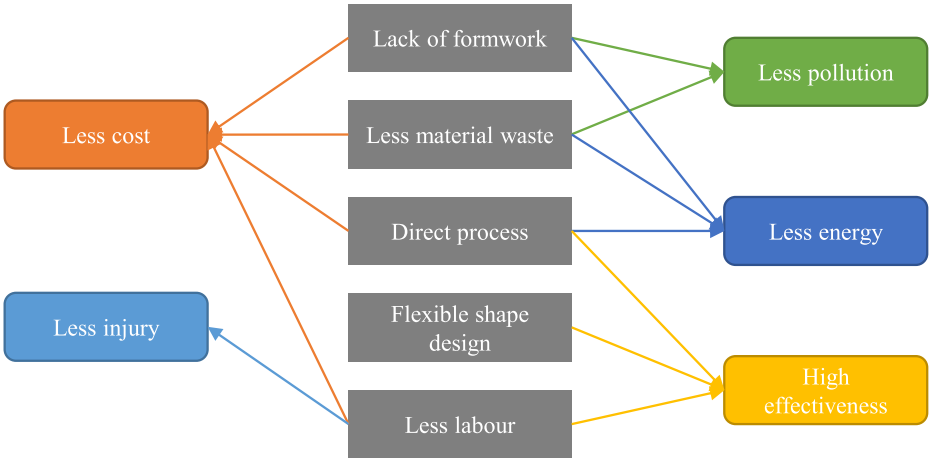

Fig. 13. Benefits of 3DPC for construction.

could not reflect the nonlinear behaviour at the early age (Liu et al., 2022e). The Drucker-Prager model was selected in a finite element model for buildability prediction, which presented great accuracy for peak stress and plastic collapse. Kruger et al. (2019) designed a lower-bound analytical model to predict buildability. This model was created based on the rheological characterisation of fresh concrete while the plastic yielding of the bottom critical layer was critical. Mohr-Coulomb criterion provided good accuracy with verification experiments. The parameters of printing (strength correction factor for confinement, layer height, constant path length per filament, constant printing speed, filament width, aspect ratio) and material (density, re-flocculation rate, initial dynamic yield shear stress, initial static yield shear stress, structuration rate) were important input information. It was pointed out that the bulking of fresh concrete was not considered. Wolfs et al. (2018a) investigated the early stage (0–90 min) mechanical behaviour and built a finite element model based on the time-dependent Mohr-Coulomb criterion. Young's modulus and cohesion linearly increased with age, but Poisson's ratio and angle of internal friction were kept constant. The model analysed presented good qualitative prediction on failure-deformation mode, although it overestimated the strength and stability. This discrepancy was mainly contributed by the disturbance in geometry and material properties in the actual printing process.

The rheological properties of fresh concrete were critical for extrusion printing. Weng et al. (2018) proposed empirical models to predict the rheological properties of fresh concrete incorporated with fibre reinforcement. The effects of five variables were investigated (water--to-binder ratio, sand-to-binder ratio, fly ash-to-cement ratio, silica fume-to-cement ratio, and dosage of fibre) on the rheology including flow resistance, torque viscosity and thixotropy. The verification based on experiment results proved the accuracy and efficiency. Zhang et al. (2022c) modified the Coussot model to predict the static yield stress of fresh 3DPC. The static yield stress of the paste and the thickness of the excess paste layer were selected as parameters. The verification experiment also proved that the flowability of paste depended on yield stress with little influence on the type of rheology modifying agents.

3.2.2. Hardened 3DPC properties

The machinal properties are crucial for concrete structures, while the perfect evaluation method has yet to be proposed (Liu et al., 2023). Researchers keep working hard on this problem. van den Heever et al. (van den Heever et al., 2022b) analysed the failure of 3DPC incorporation of PP fibres. The 3DP sample showed non-linear compression-shear evolution explained by a modified Mohr-Griffith failure criterion where the empirical material scaling factor was proposed. In comparison, the cast sample showed liner Mohr-Coulomb criterion. This modified criterion was suitable for the anisotropic capacity of 3DPC and finite element modelling. Alyami et al. (2024) investigated various metaheuristic optimisation algorithms to predict the foundational factor compressive strength of 3DP fibre-reinforced concrete. The tunicate swarm algorithm showed excellent performance with remarkable correlation and minor error, which was analysed based on 299 samples. Ooms et al. (2021) developed a model to help mesh generation for finite element models. The complex geometry and layer interaction that was defined by the printing design were taken into consideration. General purpose 8-node linear brick elements (C3D8) were used in the layer-wise mech generation, and the Mohr-Coulomb yield criterion was applied for the material property. According to the printing design, the crucial contribution was more accurate and effective numerical modelling for failure height.

Suiker et al. (2020) built a parametric model to study failure by elastic buckling and plastic collapse of 3DP walls. Only five independent parameters. The failure and maximum stacked layers result in experiments were predicted consistently by this model. This model presented performed well in square wall layouts and simple free wall configurations but was unsuitable for complex geometry with curved or inclined elements such as variable thickness. Heever et al. (van den Heever et al., 2022c) analogised masonry and 3DPC structures and then investigated the hardened state capacity and failure mechanisms via finite element models. The 3D hollow geometries were simplified to novel representative 2D plane stress equivalents. The error of the eccentric three-point bending results was acceptable, smaller or equal to 14 %, but the shear capacity of the crack pattern was overestimated.

4. Special test methods for 3DPC

The demands for optimal 3DPC are comprehensive while all-sided testing methods are effective. Many testing techniques (Nuclear Magnetic Resonance (Liu et al., 2022f), X-ray CT (Liu et al., 2022a), nano-indentation (Geng et al., 2020), etc.) and standards (GB/T 698 2419-2005 (Ma et al., 2022), NEN-EN 196-3 (Chen et al., 2021), ASTM D5607-95 (van den Heever et al., 2022b), etc.) are adopted and valid although they are introduced based on cast concrete. This part mainly focuses on specific testing methods used in 3DPC, and universal methods with typical performance. The methods with common applications for cast concrete are not be included. For example, Casagrande et al. (2020) proposed that a nylon membrane applied during specimen preparation improved the reliability and repeatability of 3DP fresh concrete. The nylon membrane protected the specimen from disturbance during demolding. The much higher displacement rate made a higher result of strength, but it was inaccurate. However, this test was not targeted for 3DPC that was available progress for the universal concrete test.

4.1. Tests for fresh concrete quality

Rheologic properties were fundamental for extrusion printing materials. The area enclosed by the hysteresis loop of the equilibrium stress against the applied shear rate was used to describe the thixotropic behaviour (Ramakrishnan et al., 2021). Lee et al. (2022) evaluated the thixotropic behaviour by the hysteresis loop. The resting time was important for thixotropy and buildability, which was closely related to the hysteresis loop area. A close relationship between the hysteresis loop area was thus established. The yield stress was usually tested by rheometer but was complicated and time-consuming, and the torque limitation was often too low (Pott and Stephan, 2021). Therefore, Pott and Stephan (2021) proposed a slow penetrating sphere test to investigate the yield stress of 3DPC. It managed to get the measured force, calculate yield stress, and further analyse buildability.

The next step is the quality test of fresh 3DPC after extrusion. Kazemian et al. (2017) proposed a framework to estimate the fresh 3DPC quality. Three requirements were considered in print quality: surface defect-free, visible, and squared edge, dimension conformity, and consistency. Two methods were used to test the shape stability: layer settlement and cylinder stability. The former was conducted by printing layers while monitoring the settlement. The latter was conducted by filling fresh concrete in a cylinder container with a constant load while monitoring the settlement. The latter could save time and material, but the former showed more direct performance. 3DPC was more sensitive to time on most properties than cast concrete. Wolfs et al. (2018b) took two time-dependent parameters, compressive strength and Young's modulus, as objectives to investigate the ultrasonic measurements in 3DPC. The pulse velocity had a great linear relation with the R^2 of 0.999. The non-destructive monitor was helpful for the fast monitoring, especially supportive for the time-dependent parameters, although further investigation was necessary.

4.2. Mechanical properties and buildability of 3DPC

The property of layer bond was a critical issue in the 3DP structure that deserved much attention. Helsel et al. (2021) verified the abilities of many non-destructive testing methods on 3DPC bonds. The X-ray radiography image correlated with bond strength reflected by the white

pixel count percentage. Shear wave energy transmission, utilizing multi-element array ultrasonics, presented an attractive relation. The ratios of normalised energy across interlayer bonds and the bond strength showed a strong correlation. In addition, groups of key values were proposed as > 0.95, 0.95–0.60, and <0.60 represented good, weak, and little bonds, respectively.

The buildability for the 3DPC was generally tested based on specific geometry designs varying in experiments. The critical number of layers and final successful height in a stacked filaments structure could present buildability (Hou et al., 2021; Jiang et al., 2022). In a 10-layer-stack test, the optimal and unique acceptable result occurred at the continuous aggregate grading mixing plan. The ultimate yielding load was 91 N with a compression of 25 mm. The compressive strain was 2.5% that was equivalent to the weight of 30 layers (Bai et al., 2021). Compared to the simply stacked filament structure, a configuration with good shape stability was more welcomed because the material's properties could be emphasized. Chen et al. (2021) printed concrete layers with a thickness of 8 mm as cylinder circles with a diameter of 200 mm. The maximum height before structure failure was used as a buildability index closely affected by the slump test result in a linear relationship. Ma et al. (2022) used constant parameters (circular nozzle with a diameter of 18 mm, a layer thickness of 1 cm, a printing speed of 1600 mm/min) to print a hollow cylinder with a diameter of 23 cm and a designed height of 50 cm. Few surface defects, no vertical distortion and layer failure, and low deformation were required. The success height was recorded as a criterion if the collapse occurred within 50 cm. A similar method was also used in (Liu et al., 2022d). The diameter of the circular nozzle was 13.5 mm with a printing speed of 25 mm/s and a layer thickness of 9 mm. The hollow cylinder with an inner diameter of 150 mm was expected to reach 15 layers. The configuration was various. The square structure with an edge of 300 mm and double filaments was used in (Zhang et al., 2018) when the final height was taken as critical data for buildability.

Another popular method was the deformation of the critical layer under specific printing parameters and shape configurations. Pasupathy et al. (2022) printed three stacked layers and recorded the deformation of the bottom layer. This method was used to compare the stability of printer layers during the loading. Similarly, the height reduction between expected and printed values was used as the critical parameter of the stacked filaments with fourteen layers to illustrate the buildability (Cui et al., 2022). The practical height was recorded 20 min after printing. In (Ashrafi et al., 2021a) nearly all cases, the bottom layer suffered the highest upper pressure and was prone to obvious deformation.

The deformation was not limited to the vertical direction. Ji et al. (2022) used a simple printing configuration. The objective was stacked filaments reaching ten layers under constant printing parameters. It was noticeable that the dimension of the filament was relatively large (width of 100 mm and height of 40 mm) because it was designed for fresh concrete incorporated with coarse aggregate. It was not appropriate for the filament with small dimensions since the unstable shape would be dominant rather than material ability.

The novel method was proposed and tried to make progress. Liu et al. (2021) proposed the angle as the second evaluation indicator in addition to stack height. As shown in Fig. 14, the smaller tan(θ) presented less deformation and better buildability. The testing geometry and printing parameter should match the excepted application. Therefore, the widely optimal compatibility between matching geometry and printing parameter was the key to establishing a standard.

5. 3D printing for different concrete types

5.1. Functional concrete

5.1.1. Self-sensing concrete

A self-sensing geopolymer was printed on concrete to repair the surface and monitor temperature (Vlachakis et al., 2020). The metakaolin-based geopolymer with sodium-based activator showed good temperature resolution of 0.1 °C and a repeatability of 0.3 °C, where the impedance magnitude was negatively correlated with temperature. The influence of the 3DP was mainly reflected in two ways. Firstly, the electrode insertion was an additional factor on integrity, where pre-arrangement was preferred, besides universal ones like printing speed and nozzle size. Secondly, the bond strength was weaker due to the non-uniform contact between the printing geopolymer and the rough concrete surface. The reduction from −1 MPa to 0.6 MPa was accepted by the authors.

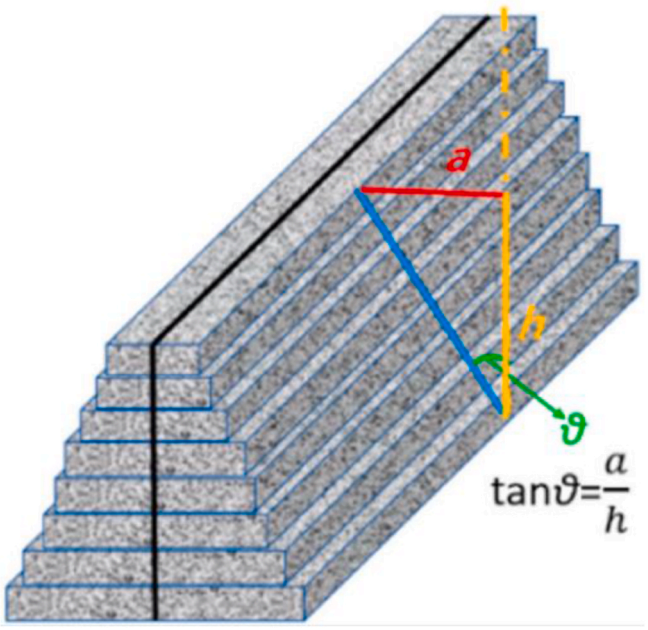

Fig. 14. Testing angle for buildability (Liu et al., 2021).

Wang et al. (2022b) investigated the performance of a self-sensing composite based on carbon fibre and activated carbon powder. In addition to anisotropic strength, the anisotropy was obvious in electrical and piezoresistive behaviour. The extrusion and printing process enabled the fibre to align with the filament, which caused a highly conductive network. However, the good conductive network only existed in each layer rather than in a perpendicular direction. The voids between layers aggravated this bad conductivity. Activated carbon powders improved the conductive path by bridging the adjacent fibres, but it mainly occurred in each layer. These features are illustrated in Fig. 15.

5.1.2. Thermo-responsive concrete

The 3DPC changed the process to complete the building, thereby causing nonnegligible effects on thermal properties. The non-uniform thermal performance in an extrusion-based 3DP room was noticeable (Sun et al., 2021a), and anisotropy also occurred in thermal performance (Hao et al., 2022). The prominent segment of temperature distribution in both vertical and horizontal directions was caused by layer connection and W-shape inner structure joints. The U-value of thermal performance varied between 1.87 and 3.04 W/(m^2·K), which was higher than 1.5 W/(m^2·K) and regarded as insufficient thermal insulation. The difference between printed concrete and cast concrete desired much attention.

Ma et al. (2022) introduced silica aerogel in 3DPC to improve thermal insulation performance. The silica aerogel granule showed particle size of 0.1–0.7 mm and low thermal conductivity (TC) of 0.012 W/(m·K). The fine silica sand was partially substituted by aerogel (0, 5, 10, 20 vol%) as aggregates with a w/b ratio of 0.42. The reduction on the spread test was observed by 0.53%–5.79% (1 mm–11 mm), showing

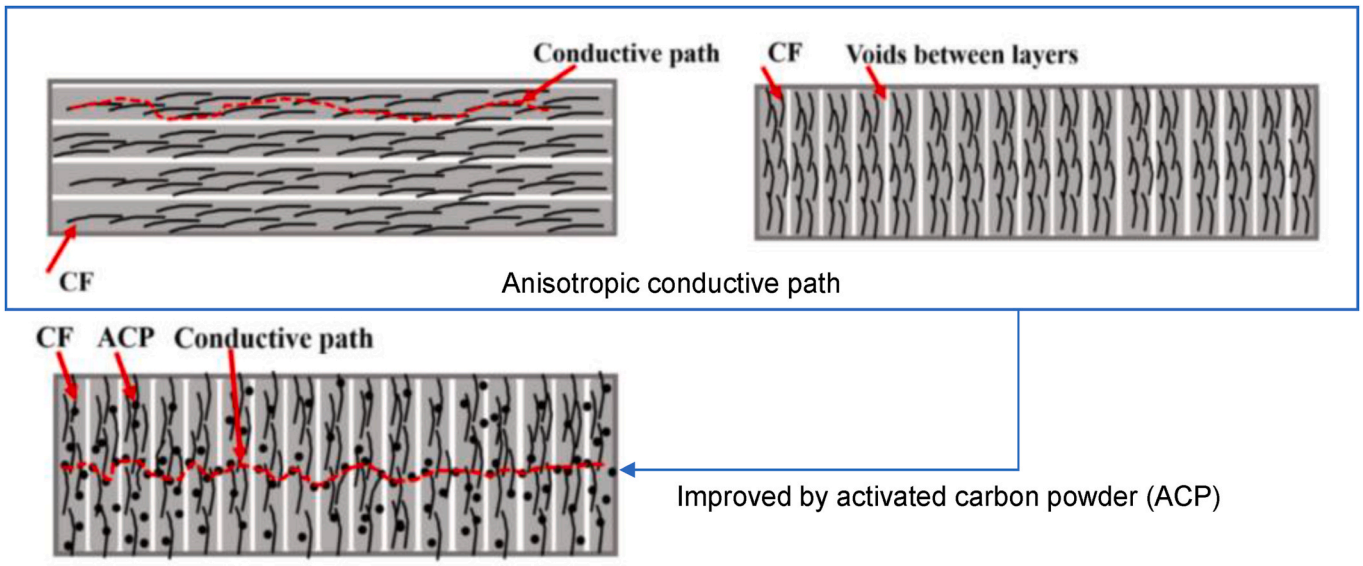

Fig. 15. Anisotropic conductive path and improvement for 3DP self-sensing concrete (Wang et al., 2022b).

lower flowability but all results were acceptable for printing. The day density and TC were decreasing that caused better thermal insulation. These two changes contributed to the fine and porous aerogel particles. The mechanical performance was decreased but much better compared with many concrete cases in similar TC. In addition to strength, the TC also presented anisotropy in 3DPC. Craveiro et al. (2020) added natural lightweight materials, granulated cork, to replace basalt sand by 10 vol %. With the help of the modified printing system, the geometry of the printed structure showed a standard deviation of 4.163 mm and a room with a multi-material functionally graded concrete wall was printed. Good energy saving was found in most testing cases. Ayegba et al. (2022) investigated the energy performance and carbon emission of 3DPC walls with different insulation plans. The polyurethane foam wall saved around 9500 kW than the reference and showed lower carbon emission (by over 2 tons) in summer. The potential of 3DPC for thermal response desired more exploration.

5.1.3. Foam concrete

Foam concrete was excellent on thermal insulation and low weight. 3DP foam concrete showed exhilarating improvement in economy, labour, and ecology compared to 3DP conventional concrete embedded insulation layer (Markin et al., 2021). The effect of high flowability on printing and the effect of extrusion on foam stability were regarded as the challenges for 3DP foam concrete (Pasupathy et al., 2022), and the optimal mix design should provide reliable printability and minimal breakage of bubbles (Markin et al., 2019). Incorporated surfactant and improved microstructural packing could ensure the stability of the foam during extrusion, where the thermal conductivities of geopolymeric foams varied between 0.15 and 0.25 W/(m·K) (Alghamdi and Neithalath, 2019). This value can be lower with the help of 3DP technology on structure design to improve the volume fraction of the whole structure.

Liu et al. (2021) attempted to use HPMC and SF to modify the printability of foam concrete. The volume bleeding rate of foam concrete was reduced and HPMC had higher sensitivity. The tan(θ) decreased in all groups, but the critical height was only sensitive to SF. Hybrid incorporation can achieve great buildability where the tan(θ) of 0.15 and critical height of 88.2 mm were presented (Liu et al., 2022f). That was explained by the flocculation model. HPMC agglomerated cement into large flocs when SF adsorbed free water also formed flocs to further reduce free water. The flocs caused by SF boosted re-flocculation after rapid shearing that improved thixotropy and buildability. The features of influence on static yield stress, dynamic yield stress, and plastic viscosity were also different. SF was dominant for the first parameter and HPMC was more effective for the rest.

The lightweight aggregate was likely to maintain the lightweight and high porosity. At the same time, the requirement on form content was lower, reducing the threat of extrusion on foam. Pasupathy et al. (2022) replaced all sands with hydrophobic surface-modified expanded perlites in the same volume. To maintain the same workability, water content was increased from 0.32 kg to 0.52 kg because of the higher specific surface area of aggregates. The wet density of concrete declined from 840 to 800 kg/m^3, although less foam (11%–7.5%) was used. The lower foam content brought the low level of foam collapse, which was proven by the density change during extrusion. A slight reduction of flowability and increment of apparent viscosity were contributed by lower foam content and features of expanded perlites (rough, irregular, rigid and high specific surface area). Cooperating with higher yield stress and the results mentioned above, the buildability was improved a lot, as shown by less deformation and failure. The compressive strength showed a remarkable increment that 100% was expected in a similar density level. The bond strength was rising and very sensitive to foam content that could be the critical reason for the stronger strength.

5.1.4. Phase change material (PCM) concrete

PCM concrete was able to regulate temperature and save thermal energy although the performance was still developing (Wang et al., 2022c). In the case of San Diego (Kuzmenko et al., 2022), the introduction of PCM offered only a slight enhancement for electricity consumption. The influence of PCM on 3DPC mainly caused varying rheology. Cui et al. (2022) introduced less than 20% commercial microencapsulated PCM with a size of 2–10 μm. More water was required due to the high specific surface area that was illustrated by the certain fluid diameter, but the printability was not affected significantly. The buildability showed similar regulation and the result was regarded as good. The compressive strength reduction was remarkable but also occurred in cast samples. This negative effect was worse, up to - 40%, by printing method because of the common quality problems of 3DPC. In the important thermal performance, the thermal conductivity was reduced by - 24% and the indoor temperature was reduced by up to 8 °C in a practical small-size experiment. Brooks et al. (2022) added commercial microencapsulated PCM in extruded concrete. The spherical shape of capsules could increase the flowability and thus decrease buildability, but this effect was alleviated when the content of capsules raised over 2.5 vol%. Due to weak capsule particles, the lower

mechanical ability and stiffness were proved as expected. It was noticeable that the printed specimen with PCM of 4.5 vol% showed slightly stronger compressive strength because higher flowability enabled the specimen to be more compact. The failure was mainly caused by the negative effect of PCM on layer connection in printed samples. The cast sample broke from the weak interfacial transition zone caused by PCM capsules. Anyway, the enhancement in temperature regulation was significant, where a reduction of around 50% in temperature amplitude can be achieved. Hao et al. (2022) tested the performance of RFA-based PCM composites on 3DPC. The paraffin was absorbed into the porous RFA. The compressive strength was lower because of RFA and further deteriorated due to the paraffin's bad bond. Porous RFA and 3DP reduced the TC, but paraffin improved it moderately. Anisotropic TC was attributed to void orientation and distribution, which could be mitigated by optimal printing parameters. Christen et al. (2023) built a PCM-3DPC concrete façade section in South Africa with a stable structure. The PCM was absorbed in recycled brick aggregate and the 28-day compressive cube strength achieved 50.6 MPa. This 3DPC presented the benefit of PCM where the maximum temperature gap reached to 3.9 °C with a total average latent heat capacity of 7360 J/kg.

5.1.5. Electromagnetic shield concrete

The electromagnetic wave (EMW) is harmful and EMW absorbing concrete is one of the solutions. mobile base stations Ma et al. (Sun et al., 2021b) incorporated copper slag and powder in extrusion-based 3DPC that was rich in Fe and Cu elements with outstanding magnetic anisotropy and high resonance frequency. An enhancement on strength of 9%–40% was obtained that was caused by lower porosity. Squeezing effect during extrusion reduced the pore size and amount. The EMW absorbing bandwidth was 4.46 GHz of 3DP sample while cast sample showed 2.71 GHz lower value. The compacter microstructure was a main reason and printing orientation effecting was another one. The reflection was regulated to enhance space impedance matching. In another experiment (Ma et al., 2018b), 3DP samples had better EMW absorption in the frequency ranges of 1–18 GHz. The surface of 3DPC was normally corrugated and rough compared to cast concrete, if there was not post process. The corrugate surface of 3DPC improved massive EMW reflection. The rough surface resulted in more EMW consumption and matching transition and diffusing reflection. The 3DPC presents attractive performance incorporated with EMW absorbing capability and further comprehensive research is essential.

5.2. Sustainable concrete

5.2.1. Recycled aggregate concrete

Recycled aggregate (RA) concrete has always been a hot topic, including for 3DPC. RA generally had high water absorption caused by wrapped mortar (Bai et al., 2021). The shrinkage problem was prone to be worse due to this feature, but methods like oversaturation could mitigate that. Bai et al. (2021) proposed that the RA could strengthen the layer bond but there was no natural aggregate reference. Rahul et al. (2022) investigated the natural and recycled coarse aggregates (RCA) with a maximum diameter of 8 mm on extrusion 3DPC. The recycled coarse aggregate led to a marginal reduction in shear stress, yield stress (from 398 to 366 Pa) and plastic viscosity (from 34 to 32 Pa s). This trend also occurred in compressive and flexural strength. However, the failure height increased to - 4 mm with similar surface quality and recycled coarse aggregates further controlled autogenous shrinkage. Li et al. (Liu et al., 2022b) also proved the anisotropic characteristics of compressive and flexural strength reduction due to RCA substitution. The final value was acceptable and higher than the sample without coarse aggregates. The effect of RCA on porosity was more evident in 3DP specimens, which was 10.09% higher than in the cast counterpart. This may be caused by the changed properties of fresh concrete that were more sensitive to the printing method.

The aggregates were fully replaced by recycled aggregates according to size, fine, coarse, and both (Xiao et al., 2022). The RCA was rough and rounded, and the recycled fine aggregates (RFA) was roughly rounded. Considering the higher water absorption and shape, additional and fractional water were added to maintain the extrusion. Moisture evaporation was a key issue in 3DPC without formwork. The RFA presented better than RCA due to higher water absorption and specific surface area. The maximum compressive strength observed in the X (printing direction) was affected by RCA, while the strength in the Y and Z directions was more sensitive to RFA.

The RFA substitution was prevalent. The improvement of additives on RFA 3DPC was effective and defined as a possible application (Xiao et al., 2021). The RFA 3DPC was successfully applied in the part of a large-scale 3DP room (Xiao et al., 2020). Xiao et al., 2020, 2021 and Zou et al. 2021 used fine recycled concrete to replace nature sand where the major difference in aggregates was higher water absorption of recycled fine aggregate (13.5% higher than 4.5%). At a 25% replacement ratio, a reduction of compressive strength by ~8 MPa and increased flexural strength by ~1.5 MPa were observed (Xiao et al., 2020). The printability window became shorter and compressive resistance was improved at the early stage when the replacement reached 100% (Zou et al., 2021). The RFA was regarded as having *higher green strength and no obvious decrease in hardened mechanical properties* in (Xiao et al., 2020). Ding et al. (2020) incorporated RFA and analysed green strength in detail. Based on uniaxial compressive tests, the RFA replacement showed negligible effects on immature specimens (rest 30–60 min after extrusion) that presented obvious lateral deformation and plastic behaviour. For mature specimens (rest 90–150 min after extrusion), the material presented small lateral deformation and shear failure plane (i.e., rigid behaviour). This feature was highlighted in RFA specimens. Sun et al. (2022) further investigated carbonized RFA. The weak strength was improved obviously. The rate of compressive strength was up to 68.5%, while the maximum enhancement was 21.4% of flexural strength and 17.6% of bond strength compared with untreated RFA in the same amount. The large pores were divided into small pores and a large number of acicular ettringites were generated inside the pores and interfacial transition zones. The carbonation enabled the RFA to participate and accelerate the hydration of new cement that optimised the pore structure and product density.

The very fine recycled powder could partially replace cement to fabricate sustainable concrete. Hou et al. (2021) used recycled powder mainly containing waste brick and concrete that was slightly finer than cement. The cement was replaced up to 30% by weight and SP was adjusted to meet the requirement for flowability when other raw materials were relatively constant. The high demand for water from recycled powders was proved by a great loss in flowability and consistency because the powders had small particle sizes, microcracks and micropores. Less free water, fine powder distraction, and active ions in recycled powder accelerated hydration, especially in the early stage, significantly improving buildability and mechanical properties. When the replacement ratio was 30%, 75% reduction of open time, 47% reduction of initial setting time, 42.5% reduction of final setting time, 226.5% increment of maximum stress, and 252.2% increment of Young's modulus were important representative property evolution.

5.2.2. Crumbed rubber concrete

Crumbed rubber was different to conventional rigid material in concrete. Liu et al. (2022d) introduced cement modification on the rubber surface, popular in cast concrete, into 3DP rubber concrete. The 15 wt% of sand was replaced by crumb rubber with cement-coated. The coating cement paste with a constant water-to-cement ratio of 0.5 was not subtracted from the cement in the mix. The impact of cement paste amount on slump and flow was minor, and good buildability was proved. The increasing cement paste caused higher strength (up to 16.1% in the Z direction and 25.7% in the Y direction). Still the effectiveness was lower when the weight ratio of cement/crumb rubber exceeded 0.4. It is noticeable that the anisotropy was also more obvious

with more cement paste. The smaller and elongational pores were found, which affected the strength. The weight ratio of cement/crumb rubber 0.4 was regarded as the optimal choice in this experiment.

Sambucci et al., 2020a, 2020b used ground tire rubber to replace fine aggregates by volume ratio. The maximum size of sand was 0.4 mm while that of rubber powder was 1 mm, and the rubber granule was larger (2–4 mm). The better-filling performance of rubberised concrete impelled fewer interlayer voids and cavities, improving interfacial cohesion. However, the total void content was higher because of the ability of rubber aggregates to repel water and entrap air, which resulted in lower density (maximum reduction was 30%). On the one hand, a much weaker strength was observed due to low density and poor compatibility between rubber particles and cement paste. On the other hand, the sample showed excellent ductility, and the incorporated rubber hindered the crack propagation. The mechanical ability could be modified by changing the mix plan but the possibility of 3DP rubber concrete was reasonable and beneficial to a sustainable environment.

5.2.3. Waste glass (WG) aggregate concrete

WG was able to replace natural aggregate and work in 3DPC. Cuevas et al. (2021) introduced the sola-lime beverage WG to replace crushed basalt as fine aggregates. The processed WG can pass the sieve of 1 mm with varying morphology including flat, elongated and needle-shaped. The particle size distribution of WG was broader than that of basalt although the largest size was the same, which meant WG was finer. The finer WG caused shorter setting times (by around 1 h) due to the accelerated cement hydration attributed to the "filler effect" or "pozzolanic reaction". The thermal insulation was improved thanks to the printing feature and promoted by the lower thermal conductivity (TC) of WG. As for strength, 50 vol% of WG showed stronger flexural and compressive strength results. The former was explained by the orientation of elongated and angular glass particles aligned by nozzle extrusion. The latter was explained by the packing ability of coarser crushed basalt aggregate and finer WG particles. The partial substitution (50 vol% in this experiment) was recommended to balance the benefits. Liu et al. (2022c) studied the gradation of WG particles to analyse their effect on mechanical properties and microstructure. Two gradations of WG were investigated in this experiment, fine and coarse glass with a median size of 367 μm and 796 μm, which were larger than the sand counterpart (204 μm). WG was bonded well with a binder similar to sand. The total porosity was increased due to WG addition, especially from the coarse particle group. The most changes occurred in large pores with a diameter over 1 mm. The different porosity affected crack propagation, which caused a remarkable change in the modified failure model from brittle to softening before the peak.

5.2.4. Geopolymer concrete

Unlike cement-based concrete, the activator solution for geopolymer concrete significantly influenced fresh concrete properties. The activator viscosity in (Panda et al., 2019b) was dominantly affected by the geopolymer viscosity, although the solution-to-binder ratio also showed obvious negative effects. The viscosity of the potassium silicate-based activator was very sensitive to the molar ratio but a higher ratio may cause lower compressive strength. The highly purified attapulgite clay presented minimal effects on viscosity but significantly improved yield stress and thixotropy at only 0.5% dosage, leading to lower demand on extrusion pressure (Panda et al., 2019b). However, unaffected strength at the early stage and a reduction of – 17% at the final stage were found because of weak nanoclay reaction. Chougan et al. (2020) added nano-graphite platelets in geopolymer concrete to improve the performance of the 3DP. The basic reason was the Van Der Waals force and the super sorbent characteristics of nano-graphite platelets. The lubrication effect was dominant at low dosage (0.1% in this paper), leading to increased workability. The thickening phenomenon was prominent at a high dosage thus causing better shape stability with 52% deformation. The effect on mechanical properties was positive, although the efficiency fluctuated with the addition ratio. Nematollahi et al. (2018) investigated the effects of PP fibre with a diameter of 11.2 μm and length of 6 mm on 3DP geopolymer concrete. Similar to cement concrete, geopolymer concrete with PP fibre showed lower flowability, leading to less interlayer contact, although it was extrudable. This further made weaker layer bond strength. The benefits on mechanical performance mainly occurred on perpendicular compressive strength and ductility but the amount was recommended at 0.25 vol%. More fibre brought more voids that posed adverse effects.

Panda et al. (2017) investigated the important physical performance of printed geopolymer concrete. Class F fly ash, silica fume and GGBS were binders with the weight ratios of 27.85%, 3.36% and 1.68% while 12.5 wt% potassium silicate played as an alkaline reagent. Also, 0.875 wt% thixotropic additives were used to adjust the printability. A slight improvement in density of 4.7% was explained by forceful pressure during extrusion. Similar anisotropic strength and micropores were found in printed samples. It was noticeable that a rare enhancement of compressive strength occurred, in a perpendicular plane to the layers. The tensile bond strength was obviously affected by the layer time gap and the shorter time gap allowed the bond to be stronger close to cast concrete. Muthukrishnan et al. (2020) introduced microwave to improve the bond strength of 3DP geopolymer concrete. The binder consisted of class F FA and GGBS while anhydrous sodium metasilicate was selected as an alkali activator. Each layer was heated in a domestic microwave oven (power 1200 W and operating frequency 2.45 GHz) for a duration then was removed out and kept setting for 1 min before printing the top layer. This design can mimic the microwave applied at the end of the nozzle. The heating process caused a faster polycondensation reaction that increased bond strength by 132% at 7th day and 87.5% at 28th day when the duration was 10 s. The stiffness was also increased, and higher stiffness made less contact area, which explained the decrement in bond strength when the heating duration was over 10 s. The effect on polycondensation reaction was significant before 10 s, considering the most moisture loss happened from 10 s. In addition, the viscosity recovery percentage was enhanced from 25% to 100% due to 10 s microwave treatment. Finally, the lateral deformation was reduced by 87% after 10 s exposure that enhanced buildability.

There were many valuable studies showing the application and performance of powder-based 3DP geopolymer concrete. The composition of the alkaline solution should be considered in the printing parameter design, which cooperated with penetration behaviour (Voney et al., 2020) that was analysed by powder porosity and specific density. The unreactive powder will cause worse quality. The geopolymer reaction mostly started when the liquid was applied, which had more stringent reaction conditions. The FA required a higher reaction temperature than slag; therefore, the reduction of compressive strength was expected and proved. Xia et al. (2019) recommended that the maximum content of FA was 50 wt% to ensure the complete reaction. Apart from lower reactiveness, the reduced penetration depth caused by finer FA particles was another reason for the reduced quality. With the curing in Na^{+}-based solution with a higher alkali modulus of 3.22 (Nematollahi et al., 2019), the compressive strength was further improved and the density dropped significantly. The printed structure was strong enough after 2 h of curing at room temperature, but further curing in a saturated anhydrous sodium metasilicate solution at 60 °C improved the strength more than 15 times (Xia and Sanjayan, 2016).

5.3. Special concrete

5.3.1. Lightweight concrete

The effect of lightweight aggregates on 3DPC was expected. Rahul and Santhanam (2020) attempted to lightweight coarse aggregate concrete based on expanded clay with a size smaller than 10 mm. The expanded clay decreased the packing density, making the pore solution easier to drain out, i.e., worse water capacity. The replacement rate by volume was limited to less than 30%. Otherwise, phase separation and

blockage duration were observed. The enhancement of compressive and stiffness were also found. Thanks to the lower density and better strength, the material offered higher critical failure height considering plastic collapse (56–72%) although it was 10–17% for the buckling collapse model.

The key advantage of 3DPC for lightweight was contributed by the structure design. Ramakrishnan et al. (2021) utilised the customisation of 3DP to achieve lightweight concrete by shaped filaments, although the theory was totally different to conventional lightweight concrete (using lightweight aggregates or introducing foam). Considering the filament was the basic element of 3DPC, it could be defined as lightweight concrete and made a difference between construct optimisations. The shape was controlled by a designed nozzle as shown in Fig. 16. The density (1576 and 1701 kg/m^3 of hollow core and U-shape) and compressive strength (19.3 and 14.6 MPa of hollow core and U-shape) of shaped filaments were equally good with conventional lightweight concrete. However, the reduction in bond strength was obvious because of the less effective contact area compared with solid filaments.

Further, the 3DP enabled the cooperation of various concrete to achieve better performance. Geng et al. (2022) fabricated foam concrete with different amounts of foam and fibre, showing various mechanical performances and densities. The innovation was attributed to 3DP, which enabled the graded layers with different properties as shown in Fig. 17. The code name of the layer presented the bending strength: Weak, Moderate, Strong, High-strong, Ultra-high-strong. The stronger layer was placed at the critical part. The crack in the bending test initially occurred at the bottom where the UHWWMS sample showed much progress in the bending test and impact test with lower density compared to the cast reference. It was noticeable that the stress distribution was modified due to graded machinal properties.

5.3.2. *Ultra-high-performance concrete (UHPC)*

UHPC potentially allow 3DPC to play a considerable role in flexible shape design with enough self-support. Yang et al. (2022a) investigated the performance of 3DP UHPC under uniaxial and triaxial confining loads. There was no noticeable difference in production methods that showed brittle failure mode, but the addition of steel fibre changed it to ductility. The thickness of each layer was 5 mm, and the inner diameter of the nozzle was 15 mm. The specimen with 6-mm fibres showed better printing quality, while the 10-mm fibre caused uneven surface because of difficult extrusion (Yang et al., 2022b). Based on the mechanical performance, the anisotropy was obvious except for a minor variation in the tensile elastic modulus. The flexural and splitting tensile failure could be either ductile or brittle in different directions (Yang et al., 2022b). The highest flexural strength reached 45.21 MPa in the printing direction. The reasonable failure criterion was different. The Power-law and the Willam-Warnke failure criterion fitted well for all 3D printing specimens, while the widespread Mohr-Coulomb failure criterion did not fit 3DP UHPC.

Arunothayan et al. (2020) investigated the performance of UHPC before and after steel fibre (length of 13 mm and diameter of 200 μm) addition at 2 vol%. The mixing proportion was calculated based on the modified Andreasen and Anderson model. The flowability decreased slightly but the shape retention was much better. The higher compressive strength, modulus of rupture, flexural toughness and apparent porosity were observed in the cast and printed samples. The anisotropy of compressive strength was clearer in printed samples after fibre addition. The highest value occurred in the longitudinal direction but was still lower than that of cast samples. In contrast, flexural performance was remarkably higher in both perpendicular and lateral directions due to the alignment of fibres in the printing direction. Although the aligned fibre did not bridge layers, the bond strength improved greatly. The fibre alignment performance was influenced by various factors. Higher fibre amount and smaller extrusion nozzle size improved the alignment effect and the fibres closer to the nozzle wall suffered higher sheared flow (Arunothayan et al., 2021). Furthermore, they used fly ash and ground granulated blast furnace slag to replace cement (Arunothayan et al., 2022) but the VMA was changed from sodium carboxymethyl cellulose water-soluble polymer powder to nanoclay. In the flowability test, the spread diameter was improved by fly ash due to the spherical shape, which brought better particle packing and bell-bearing effect. In contrast, the furnace slag with an angular shape and smaller size reduced the diameter value because of higher water demand. The effectiveness of nanoclay decreased because of cement replacement, especially replaced by FA. Lower hydration kinetics of FA and furnace slag caused lower compressive strength where the reduction was higher after 90-day curing. Compared to fibre, the improvement of cement replacement was negligible, but the global warming potential was remarkably reduced.

Dong et al. (2022) investigated the microstructure and mechanical

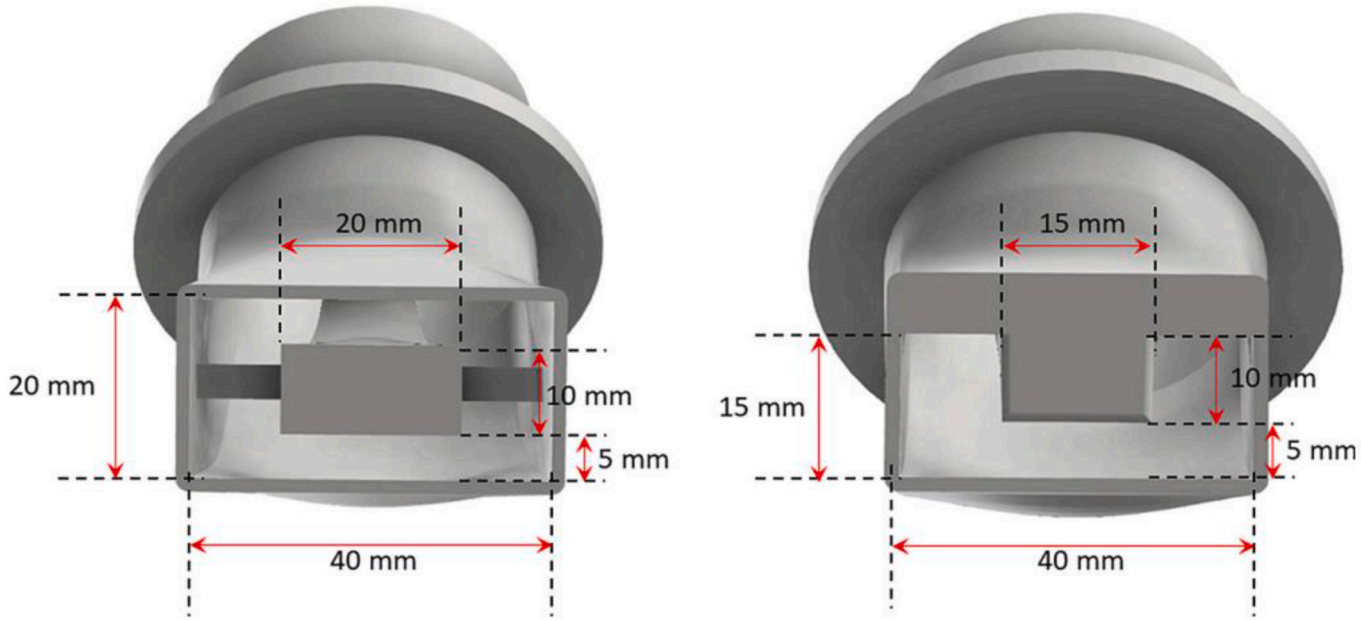

Fig. 16. Novel nozzle to print hollow-core filament and U-shape filament (Ramakrishnan et al., 2021).

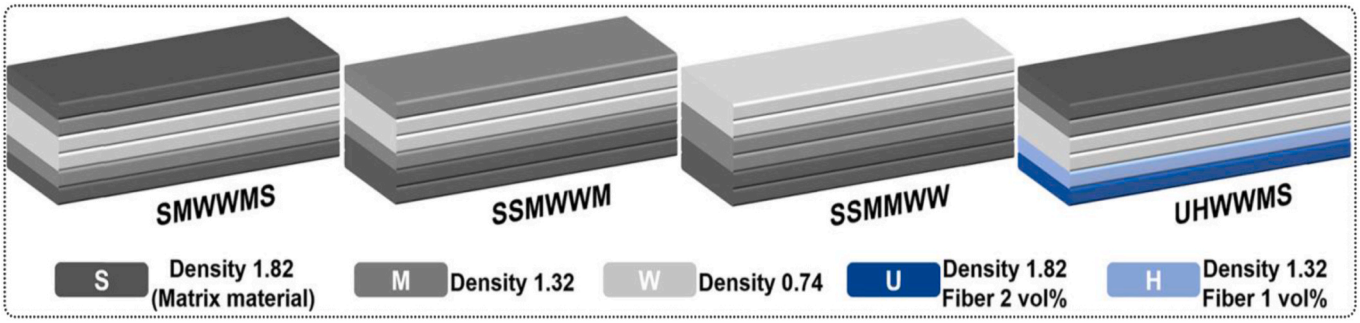

Fig. 17. Graded layers in (Geng et al., 2022).

performance of 3DP UHPC in after elevated temperatures up to 500 °C. The mechanical anisotropy did not change significantly due to the high temperature. The steel fibres in the concrete increased the strength and ductility that was good for burst resistance. In addition, the 3D printing process caused the weak interlayer that enabled easier water evaporation because of the high temperature, which improved the fire resistance of concrete.

5.3.3. Engineered cementitious composite concrete

The Engineered Cementitious Composite concrete (ECC concrete), also called strain-hardening cement-based composite concrete, was potentially more suitable for 3DPC than conventional concrete mixing design due to the difficulty of incorporating reinforcement structure (Zhu et al., 2019; Soltan and Li, 2018; Xu et al., 2022). Zhou et al. (2022) proposed that fibre addition as a key feature of ECC cannot be neglected, which normally caused high viscosity and yield stress. They also proposed a time-dependent strain-stress model based on fresh strength development. The critical height for buckling was predicted by the stiffness evolution, which was verified by the PVA fibre-based ECC in the experiment. Soltan and Li (2018) introduced detailed steps to design a printable ECC concrete from multi-factors, including calcium aluminate cement for hydration acceleration, HPMC for flowability manipulation, water content and temperature for rheological properties, etc. The final composition showed a tensile strain capacity of - 4%, tensile strength of 6 MPa and compressive strength of 30 MPa within 6 days, in addition to good extrudability and buildability. Xu et al. (2022) designed a printable ECC based on PE fibres (length of 12 mm) and modification method by nanoclay. The thinner nozzle with constant cross section showed better ultimate tensile strain and higher first-cracking strength. On the other hand, it was prone to getting clogged. The anisotropy was remarkable in the 2D testing where parallel tensile loading to printing direction presented the best strain-hardening performance and strength capability. The printing angle of 45°, the bisector of principal stress directions, was proposed to compensate for the anisotropy. This printing angle maintained obvious ductility and better strength than cast ECC. Zhu et al. (2019) used Portland cement, sulfoaluminate cement, and FA class F (weight ratio of 40:3:57) as a binder while PE fibre with a length of 12 mm and an aspect ratio of 500 was incorporated. Similar to 3DP conventional concrete, VMA, SP, and attapulgite nanoclay were introduced to improve the extrudability and buildability. The superiority compared to cast specimens was attributed to parallel fibre orientation, uniform pore size and narrower distribution caused by extrusion. That corresponded to the conclusion in (Ogura et al., 2018), in which high-density PE fibres with a length of 6 mm and an aspect ratio of 500, as well as relatively large sands (<1 mm) were used. The uniaxial tensile results showed optimal tensile strain capacity of up to 11.43% with 2 vol% fibres (Zhu et al., 2019). The extrusion may be difficult if the fibre content exceeded 2% due to nonuniform distribution (Zhu et al., 2022) and Xu et al. (2022) proposed this problem occurred from 1.5% in the experiment with PE fibres with a length of 12 mm. Apart from the slight change in matrix mixing design, they partially introduced PE fibre with a length of 6 mm and an aspect ratio of 250 to analyse the microstructure (Zhu et al., 2022). The pore morphology was not changed significantly although the size was reduced in printed specimens. The local fibre volume fraction and fibre distribution coefficient were not closely related to the printing method, although oriented fibres were prominent. The printed ECC showed more robust ductility in the extrusion method.

The properties of different concrete were various and had multiple features for 3DPC, including pros and cons. The combination of 3DP with different concrete was not only a function addition. The high-level freedom of 3DP provided ample space to achieve many challenging objectives for cast concrete.The unconventional concrete structure could improve the efficiency of thermal regulation for PCM concrete and thermo-responsive concrete, although optimisation was required. This benefit was also observed in lightweight concrete. In addition, the resource-saving ability of 3DPC and sustainable concrete push environmental protection forward effectively. On the other hand, the better mechanical properties of UHPC and ECC allowed the 3DPC to present full advantage on special-shaped structures while the incorporation quality of fibre is another challenge (Warsi et al., 2023). It was also noticeable that the printing process posed new challenges to material design, such as the foam stability for foam concrete (Lu and Wong, 2018).

6. Conclusions and prospectives

The 3D printing (3DP) is an attractive technology that provides a broader platform for concrete. The outstanding ability to create special and complex structures and higher efficiency on cost, labour, and resources are generally regarded as the key advantages of 3D printing in construction. This paper reviews state-of-the-art researches and proposes comments for the efficient development of 3DPC applications.

(1) 3DPC does not always show prominent benefits and cast concrete will still show foundational power in mass production with a simple structure, at least in the current stage. Therefore, research and application of 3DP should focus on utilizing its advantages rather than completely replacing cast concrete.
(2) The printing methods and machines illustrate respective characteristics that all deserve continuous development to extend the application areas. The 3D printer is a foundational component of 3DPC that is entirely different from conventional tools for cast concrete. Successful studies and applications for extrusion printing are dominant, but powder-based printing still has intrinsic benefits such as less moisture evaporation and better support in the early stage.
(3) The criteria and properties of printed material are closely related to the features of 3D printers, demanding the printing capacity of 3D printers, such as size, flexibility, speed, and so on. The evaluation of raw materials should introduce a relationship with the printer, such as the particle size distribution of aggregates,

rheology, hardening speed of fresh concrete, water retaining, etc. They vary for different printers.

(4) The development of 3D printing in construction is rapid, while standards based on research results are critical for further application. Besides modification for mixing strategy, path model, and quality testing, optimizing the printing process is especially significant for 3D printing. Non-destructive monitoring during the printing process can offer real-time data that is significant for further modification and investigation. Although progress has been demonstrated, there is still a huge gap in fully applying this technique in 3DPC. Universal concrete reinforcement is still favorable but much work for modification is necessary. Besides reinforcement embedding material and structure, the compatibility with the concrete printing process is also demanding and decisive.

(5) Incorporating 3DP with unconventional concrete is essential and has enormous potential. The combination may result in mutual improvement. Self-sensing concrete requires additional processes to acquire enough conductivity. The use of anisotropic conductive paths and flexible shape design may be valuable, but an attractive application is requisite. The cooperation of thermo-responsive concrete, foam concrete, PCM concrete, lightweight concrete, UHPC, and ECC with 3DP can double the benefits although much effort is required. The 3DP technique raises the efficiency of sustainable concrete, while the mixing strategy needs modification to meet the requirement for 3DP.

CRediT authorship contribution statement

Xiaonan Wang: Formal analysis, Validation, Writing – original draft, Writing – review & editing, Software. **Wengui Li:** Conceptualization, Writing – original draft, Writing – review & editing, Funding acquisition, Supervision, Project administration, Resources. **Yipu Guo:** Validation, Writing – review & editing. **Alireza Kashani:** Validation, Writing – review & editing. **Kejin Wang:** Validation, Writing – review & editing. **Liberato Ferrara:** Validation, Writing – review & editing. **Isabel Agudelo:** Validation, Writing – review & editing.

Declaration of competing interest

The authors declare that they have no known competing financial interests or personal relationships that could have appeared to influence the work reported in this paper.

Data availability

Data will be made available on request.

Acknowledgement

The authors would like to acknowledge the support from Australian Research Council (ARC), Australia (FT220100177, LP230100288, DP220101051, DP220100036, IH200100010). Wengui Li also thanks the International Excellence Fellowship of Karlsruhe Institute of Technology (KIT), Germany. Xiaonan Wang and Yipu Guo also appreciate the support from China Scholarship Council (CSC).

References

Agustí-Juan, I., Müller, F., Hack, N., Wangler, T., Habert, G., 2017. Potential benefits of digital fabrication for complex structures: environmental assessment of a robotically fabricated concrete wall. J. Clean. Prod. 154, 330–340.

Al-Qutaifi, S., Nazari, A., Bagheri, A., 2018. Mechanical properties of layered geopolymer structures applicable in concrete 3D-printing. Construct. Build. Mater. 176, 690–699.

Alghamdi, H., Neithalath, N., 2019. Synthesis and characterization of 3D-printable geopolymeric foams for thermally efficient building envelope materials. Cement Concr. Compos. 104, 103377.

Alhumayani, H., Gomaa, M., Soebarto, V., Jabi, W., 2020. Environmental assessment of large-scale 3D printing in construction: a comparative study between cob and concrete. J. Clean. Prod. 270, 122463.

Alyami, M., Khan, M., Javed, M.F., Ali, M., Alabduljabbar, H., Najeh, T., Gamil, Y., 2024. Application of metaheuristic optimization algorithms in predicting the compressive strength of 3D-printed fiber-reinforced concrete. Developments in the Built Environment 17, 100307.

Anton, A., Reiter, L., Wangler, T., Frangez, V., Flatt, R.J., Dillenburger, B., 2021. A 3D concrete printing prefabrication platform for bespoke columns. Autom. ConStruct. 122, 103467.

Arunothayan, A.R., Nematollahi, B., Ranade, R., Bong, S.H., Sanjayan, J., 2020. Development of 3D-printable ultra-high performance fiber-reinforced concrete for digital construction. Construct. Build. Mater. 257, 119546.

Arunothayan, A.R., Nematollahi, B., Ranade, R., Bong, S.H., Sanjayan, J.G., Khayat, K.H., 2021. Fiber orientation effects on ultra-high performance concrete formed by 3D printing. Cement Concr. Res. 143, 106384.

Arunothayan, A.R., Nematollahi, B., Ranade, R., Khayat, K.H., Sanjayan, J.G., 2022. Digital fabrication of eco-friendly ultra-high performance fiber-reinforced concrete. Cement Concr. Compos. 125, 104281.

Ashrafi, N., Duarte, J.P., Nazarian, S., Meisel, N.A., 2019. Evaluating the relationship between deposition and layer quality in large-scale additive manufacturing of concrete. Virtual Phys. Prototyp. 14 (2), 135–140.

Ashrafi, N., Nazarian, S., Meisel, N.A., Duarte, J.P., 2021a. Experimental prediction of material deformation in large-scale additive manufacturing of concrete. Addit. Manuf. 37, 101656.

Ashrafi, N., Nazarian, S., Meisel, N.A., Duarte, J.P., 2021b. Experimental calibration and compensation for the continuous effect of time, number of layers and volume of material on shape deformation in small-scale additive manufacturing of concrete. Addit. Manuf. 47, 102228.

Ashrafi, N., Nazarian, S., Meisel, N., Duarte, J.P., 2022. A grammar-based algorithm for toolpath generation: compensating for material deformation in the additive manufacturing of concrete. Addit. Manuf. 55, 102803.

Asprone, D., Auricchio, F., Menna, C., Mercuri, V., 2018. 3D printing of reinforced concrete elements: technology and design approach. Construct. Build. Mater. 165, 218–231.

Ayegba, B.O., Egbe, K.-J.I., Matin Nazar, A., Huang, M., Hariri-Ardebili, M.A., 2022. Resource efficiency and thermal comfort of 3D printable concrete building Envelopes optimized by performance enhancing insulation: a numerical study. Energies 15 (3).

Bai, G., Wang, L., Ma, G., Sanjayan, J., Bai, M., 2021. 3D printing eco-friendly concrete containing under-utilised and waste solids as aggregates. Cement Concr. Compos. 120, 104037.

Brooks, A.L., He, Y., Farzadnia, N., Seyfimakrani, S., Zhou, H., 2022. Incorporating PCM-enabled thermal energy storage into 3D printable cementitious composites. Cement Concr. Compos. 129, 104492.

Cao, X., Yu, S., Zheng, D., Cui, H., 2022. Nail planting to enhance the interface bonding strength in 3D printed concrete. Autom. ConStruct. 141, 104392.

Carneau, P., Mesnil, R., Roussel, N., Baverel, O., 2020. Additive manufacturing of cantilever - from masonry to concrete 3D printing. Autom. ConStruct. 116, 103184.

Casagrande, L., Esposito, L., Menna, C., Asprone, D., Auricchio, F., 2020. Effect of testing procedures on buildability properties of 3D-printable concrete. Construct. Build. Mater. 245, 118286.

Cesaretti, G., Dini, E., De Kestelier, X., Colla, V., Pambaguian, L., 2014. Building components for an outpost on the Lunar soil by means of a novel 3D printing technology. Acta Astronaut. 93, 430–450.

Chen, Y., Li, Z., Chaves Figueiredo, S., Çopuroğlu, O., Veer, F., Schlangen, E., 2019. Limestone and calcined clay-based sustainable cementitious materials for 3D concrete printing: a fundamental study of extrudability and early-age strength development. Appl. Sci. 9 (9).

Chen, Y., Chaves Figueiredo, S., Li, Z., Chang, Z., Jansen, K., Çopuroğlu, O., Schlangen, E., 2020. Improving printability of limestone-calcined clay-based cementitious materials by using viscosity-modifying admixture. Cement Concr. Res. 132, 106040.

Chen, Y., He, S., Zhang, Y., Wan, Z., Çopuroğlu, O., Schlangen, E., 2021. 3D printing of calcined clay-limestone-based cementitious materials. Cement Concr. Res. 149, 106553.

Chen, K., Liu, Q., Chen, B., Zhang, S., Ferrara, L., Li, W., 2024. Effect of raw materials on the performance of 3D printing geopolymer: A review. J. Build. Eng. 84, 108501.

Chougan, M., Hamidreza Ghaffar, S., Jahanzat, M., Albar, A., Mujaddedi, N., Swash, R., 2020. The influence of nano-additives in strengthening mechanical performance of 3D printed multi-binder geopolymer composites. Construct. Build. Mater. 250, 118928.

Christen, H., van Zijl, G., de Villiers, W., 2023. Improving building thermal comfort through passive design – an experimental analysis of phase change material 3D printed concrete. J. Clean. Prod. 392, 136247.

Classen, M., Ungermann, J., Sharma, R., 2020. Additive manufacturing of reinforced concrete—development of a 3D printing technology for cementitious composites with Metallic reinforcement. Appl. Sci. 10 (11).

Craveiro, F., Bartolo, H.M., Gale, A., Duarte, J.P., Bartolo, P.J., 2017. A design tool for resource-efficient fabrication of 3d-graded structural building components using additive manufacturing. Autom. ConStruct. 82, 75–83.

Craveiro, F., Nazarian, S., Bartolo, H., Bartolo, P.J., Pinto Duarte, J., 2020. An automated system for 3D printing functionally graded concrete-based materials. Addit. Manuf. 33, 101146.

Cuevas, K., Chougan, M., Martin, F., Ghaffar, S.H., Stephan, D., Sikora, P., 2021. 3D printable lightweight cementitious composites with incorporated waste glass

aggregates and expanded microspheres – rheological, thermal and mechanical properties. J. Build. Eng. 44, 102718.
Cui, H., Yu, S., Cao, X., Yang, H., 2022. Evaluation of printability and thermal properties of 3D printed concrete mixed with phase change materials. Energies 15 (6).
Diggs-McGee, B.N., Kreiger, E.L., Kreiger, M.A., Case, M.P., 2019. Print time vs. elapsed time: a temporal analysis of a continuous printing operation for additive constructed concrete. Addit. Manuf. 28, 205–214.
Ding, T., Xiao, J., Qin, F., Duan, Z., 2020. Mechanical behavior of 3D printed mortar with recycled sand at early ages. Construct. Build. Mater. 248, 118654.
Dong, L., Yang, Y., Liu, Z., Ren, Q., Li, J., Zhang, Y., Wu, C., 2022. Microstructure and Mechanical Behaviour of 3D Printed Ultra-high Performance Concrete after Elevated Temperatures. Additive Manufacturing, 103032.
Dörfler, K., Dielemans, G., Lachmayer, L., Recker, T., Raatz, A., Lowke, D., Gerke, M., 2022. Additive Manufacturing using mobile robots: Opportunities and challenges for building construction. Cement Concr. Res. 158, 106772.
Ebrahimi, M., Mohseni, M., Aslani, A., Zahedi, R., 2022. Investigation of thermal performance and life-cycle assessment of a 3D printed building. Energy Build., 112341
EN 1015-3, Methods of Test for Mortar for Masonry—Part 3: Determination of Consistence of Fresh Mortar (By Flow Table), 2006.
Feng, P., Meng, X., Chen, J.-F., Ye, L., 2015. Mechanical properties of structures 3D printed with cementitious powders. Construct. Build. Mater. 93, 486–497.
Flatt, R.J., Wangler, T., 2022. On sustainability and digital fabrication with concrete. Cement Concr. Res. 158, 106837.
Furet, B., Poullain, P., Garnier, S., 2019. 3D printing for construction based on a complex wall of polymer-foam and concrete. Addit. Manuf. 28, 58–64.
García de Soto, B., Agustí-Juan, I., Hunhevicz, J., Joss, S., Graser, K., Habert, G., Adey, B. T., 2018. Productivity of digital fabrication in construction: cost and time analysis of a robotically built wall. Autom. ConStruct. 92, 297–311.
Gebhard, L., Mata-Falcón, J., Anton, A., Dillenburger, B., Kaufmann, W., 2021. Structural behaviour of 3D printed concrete beams with various reinforcement strategies. Eng. Struct. 240, 112380.
Gebhard, L., Esposito, L., Menna, C., Mata-Falcón, J., 2022. Inter-laboratory study on the influence of 3D concrete printing set-ups on the bond behaviour of various reinforcements. Cement Concr. Compos. 133, 104660.
Geng, Z., She, W., Zuo, W., Lyu, K., Pan, H., Zhang, Y., Miao, C., 2020. Layer-interface properties in 3D printed concrete: Dual hierarchical structure and micromechanical characterization. Cement Concr. Res. 138, 106220.
Geng, Z., Pan, H., Zuo, W., She, W., 2022. Functionally graded lightweight cement-based composites with outstanding mechanical performances via additive manufacturing. Addit. Manuf. 56, 102911.
Han, Y., Yang, Z., Ding, T., Xiao, J., 2021. Environmental and economic assessment on 3D printed buildings with recycled concrete. J. Clean. Prod. 278, 123884.
Hao, L., Xiao, J., Sun, J., Xia, B., Cao, W., 2022. Thermal conductivity of 3D printed concrete with recycled fine aggregate composite phase change materials. J. Clean. Prod. 364, 132598.
Hass, L., Bos, F.P., Salet, T.A.M., 2022. Characterizing the bond properties of automatically placed helical reinforcement in 3D printed concrete. Construct. Build. Mater. 355, 129228.
He, Y., Zhang, Y., Zhang, C., Zhou, H., 2020. Energy-saving potential of 3D printed concrete building with integrated living wall. Energy Build. 222, 110110.
Helsel, M.A., Popovics, J.S., Stynoski, P.B., Kreiger, E., 2021. Non-destructive testing to characterize interlayer bonds of idealized concrete additive manufacturing products. NDT E Int. 121, 102443.
Hojati, M., Memari, A.M., Zahabi, M., Wu, Z., Li, Z., Park, K., Nazarian, S., Duarte, J.P., 2022. Barbed-wire reinforcement for 3D concrete printing. Autom. ConStruct. 141, 104438.
Hosseini, E., Zakertabrizi, M., Korayem, A.H., Xu, G., 2019. A novel method to enhance the interlayer bonding of 3D printing concrete: an experimental and computational investigation. Cement Concr. Compos. 99, 112–119.
Hou, S., Xiao, J., Duan, Z., Ma, G., 2021. Fresh properties of 3D printed mortar with recycled powder. Construct. Build. Mater. 309, 125186.
Ji, G., Ding, T., Xiao, J., Du, S., Li, J., Duan, Z., 2019. A 3D printed Ready-mixed concrete power distribution substation: materials and construction technology. Materials 12 (9).
Ji, G., Xiao, J., Zhi, P., Wu, Y.-C., Han, N., 2022. Effects of extrusion parameters on properties of 3D printing concrete with coarse aggregates. Construct. Build. Mater. 325, 126740.
Jiang, Q., Liu, Q., Wu, S., Zheng, H., Sun, W., 2022. Modification effect of nanosilica and polypropylene fiber for extrusion-based 3D printing concrete: printability and mechanical anisotropy. Addit. Manuf. 56, 102944.
Kazemian, A., Yuan, X., Cochran, E., Khoshnevis, B., 2017. Cementitious materials for construction-scale 3D printing: laboratory testing of fresh printing mixture. Construct. Build. Mater. 145, 639–647.
Kondepudi, K., Subramaniam, K.V.L., Nematollahi, B., Bong, S.H., Sanjayan, J., 2022. Study of particle packing and paste rheology in alkali activated mixtures to meet the rheology demands of 3D Concrete Printing. Cement Concr. Compos. 131, 104581.
Kruger, J., Zeranka, S., van Zijl, G., 2019. 3D concrete printing: a lower bound analytical model for buildability performance quantification. Autom. ConStruct. 106, 102904.
Kruger, J., Cho, S., Zeranka, S., Viljoen, C., van Zijl, G., 2020. 3D concrete printer parameter optimisation for high rate digital construction avoiding plastic collapse. Compos. B Eng. 183, 107660.
Kruger, J., du Plessis, A., van Zijl, G., 2021. An investigation into the porosity of extrusion-based 3D printed concrete. Addit. Manuf. 37, 101740.
Kuzmenko, K., Ducoulombier, N., Feraille, A., Roussel, N., 2022. Environmental impact of extrusion-based additive manufacturing: generic model, power measurements and influence of printing resolution. Cement Concr. Res. 157, 106807.
Lee, H., Kim, J.-H.J., Moon, J.-H., Kim, W.-W., Seo, E.-A., 2019. Correlation between pore characteristics and tensile bond strength of additive manufactured mortar using X-ray computed tomography. Construct. Build. Mater. 226, 712–720.
Lee, K.-W., Lee, H.-J., Choi, M.-S., 2022. Correlation between thixotropic behavior and buildability for 3D concrete printing. Construct. Build. Mater. 347, 128498.
Li, W., Guo, Y., Zhang, X., Dong, W., Li, X., Yu, T., Wang, K., 2024. Development of self-sensing ultra-high-performance concrete using hybrid carbon black and carbon nanofibers. Cem. Concr. Compos. 148, 105466.
Li, L.G., Xiao, B.F., Fang, Z.Q., Xiong, Z., Chu, S.H., Kwan, A.K.H., 2021. Feasibility of glass/basalt fiber reinforced seawater coral sand mortar for 3D printing. Addit. Manuf. 37, 101684.
Lim, J.H., Panda, B., Pham, Q.-C., 2018. Improving flexural characteristics of 3D printed geopolymer composites with in-process steel cable reinforcement. Construct. Build. Mater. 178, 32–41.
Liu, C., Wang, X., Chen, Y., Zhang, C., Ma, L., Deng, Z., Chen, C., Zhang, Y., Pan, J., Banthia, N., 2021. Influence of hydroxypropyl methylcellulose and silica fume on stability, rheological properties, and printability of 3D printing foam concrete. Cement Concr. Compos. 122, 104158.
Liu, C., Zhang, R., Liu, H., He, C., Wang, Y., Wu, Y., Liu, S., Song, L., Zuo, F., 2022a. Analysis of the mechanical performance and damage mechanism for 3D printed concrete based on pore structure. Construct. Build. Mater. 314, 125572.
Liu, H., Liu, C., Wu, Y., Bai, G., He, C., Zhang, R., Wang, Y., 2022b. Hardened properties of 3D printed concrete with recycled coarse aggregate. Cement Concr. Res. 159, 106868.
Liu, J., Li, S., Gunasekara, C., Fox, K., Tran, P., 2022c. 3D-printed concrete with recycled glass: effect of glass gradation on flexural strength and microstructure. Construct. Build. Mater. 314, 125561.
Liu, J., Setunge, S., Tran, P., 2022d. 3D concrete printing with cement-coated recycled crumb rubber: compressive and microstructural properties. Construct. Build. Mater. 347, 128507.
Liu, Q., Cheng, S., Sun, C., Chen, K., Li, W., Tam, V.W.Y., 2024. Steel cable bonding in fresh mortar and 3D printed beam flexural behavior. Autom. Constr. 158, 105165.
Liu, H., Ding, T., Xiao, J., Mechtcherine, V., 2022e. Buildability prediction of 3D–printed concrete at early-ages: a numerical study with Drucker–Prager model. Addit. Manuf. 55, 102821.
Liu, C., Chen, Y., Xiong, Y., Jia, L., Ma, L., Wang, X., Chen, C., Banthia, N., Zhang, Y., 2022f. Influence of HPMC and SF on buildability of 3D printing foam concrete: from water state and flocculation point of view. Compos. B Eng. 242, 110075.
Liu, K., Takasu, K., Jiang, J., Zu, K., Gao, W., 2023. Mechanical properties of 3D printed concrete components: a review. Developments in the Built Environment 16, 100292.
Lowke, D., Talke, D., Dressler, I., Weger, D., Gehlen, C., Ostertag, C., Rael, R., 2020. Particle bed 3D printing by selective cement activation – applications, material and process technology. Cement Concr. Res. 134, 106077.
Lowke, D., Mai, I., Keita, E., Perrot, A., Weger, D., Gehlen, C., Herding, F., Zuo, W., Roussel, N., 2022. Material-process interactions in particle bed 3D printing and the underlying physics. Cement Concr. Res. 156, 106748.
Lu, Q.Y., Wong, C.H., 2018. Additive manufacturing process monitoring and control by non-destructive testing techniques: challenges and in-process monitoring. Virtual Phys. Prototyp. 13 (2), 39–48.
Ma, G., Li, Z., Wang, L., 2018a. Printable properties of cementitious material containing copper tailings for extrusion based 3D printing. Construct. Build. Mater. 162, 613–627.
Ma, G., Sun, J., Wang, L., Aslani, F., Liu, M., 2018b. Electromagnetic and microwave absorbing properties of cementitious composite for 3D printing containing waste copper solids. Cement Concr. Compos. 94, 215–225.
Ma, G., A, R., Xie, P., Pan, Z., Wang, L., Hower, J.C., 2022. 3D-printable aerogel-incorporated concrete: anisotropy influence on physical, mechanical, and thermal insulation properties. Construct. Build. Mater. 323, 126551.
Marchment, T., Sanjayan, J., 2020. Mesh reinforcing method for 3D concrete printing. Autom. ConStruct. 109, 102992.
Markin, V., Nerella, V.N., Schröfl, C., Guseynova, G., Mechtcherine, V., 2019. Material Design and Performance Evaluation of Foam Concrete for Digital Fabrication, Materials.
Markin, V., Krause, M., Otto, J., Schröfl, C., Mechtcherine, V., 2021. 3D-printing with foam concrete: from material design and testing to application and sustainability. J. Build. Eng. 43, 102870.
Mechtcherine, V., Michel, A., Liebscher, M., Schmeier, T., 2020. Extrusion-based additive manufacturing with carbon reinforced concrete: Concept and feasibility study. Materials 13 (11).
Meisel, N.A., Watson, N., Bilén, S.G., Duarte, J.P., Nazarian, S., 2021. Design and system Considerations for construction-scale concrete additive manufacturing in Remote environments via robotic arm deposition. 3D Print. Addit. Manuf. 9 (1), 35–45.
Meng, Q., Hu, L., Li, M., Qi, X., 2023. Assessing the environmental impact of building life cycle: a carbon reduction strategy through innovative design, intelligent construction, and secondary utilization. Developments in the Built Environment 16, 100230.
Mohan, M.K., Rahul, A.V., De Schutter, G., Van Tittelboom, K., 2021a. Early age hydration, rheology and pumping characteristics of CSA cement-based 3D printable concrete. Construct. Build. Mater. 275, 122136.
Mohan, M.K., Rahul, A.V., Van Tittelboom, K., De Schutter, G., 2021b. Rheological and pumping behaviour of 3D printable cementitious materials with varying aggregate content. Cement Concr. Res. 139, 106258.

Mollah, M.T., Comminal, R., Leal da Silva, W.R., Šeta, B., Spangenberg, J., 2023. Computational fluid dynamics modelling and experimental analysis of reinforcement bar integration in 3D concrete printing. Cement Concr. Res. 173, 107263.
Muñoz, I., Alonso-Madrid, J., Menéndez-Muñiz, M., Uhart, M., Canou, J., Martin, C., Fabritius, M., Calvo, L., Poudelet, L., Cardona, R., Lombois-Burger, H., Vlasopoulos, N., Bouyssou, C., Dirrenberger, J., Papacharalampopoulos, A., Stavropoulos, P., 2021. Life cycle assessment of integrated additive–subtractive concrete 3D printing. Int. J. Adv. Des. Manuf. Technol. 112 (7), 2149–2159.
Muthukrishnan, S., Ramakrishnan, S., Sanjayan, J., 2020. Effect of microwave heating on interlayer bonding and buildability of geopolymer 3D concrete printing. Construct. Build. Mater. 265, 120786.
Nematollahi, B., Vijay, P., Sanjayan, J., Nazari, A., Xia, M., Naidu Nerella, V., Mechtcherine, V., 2018. Effect of polypropylene fibre addition on properties of geopolymers made by 3D printing for digital construction. Materials 11 (12).
Nematollahi, B., Xia, M., Sanjayan, J., 2019. Post-processing methods to improve strength of particle-bed 3D printed geopolymer for digital construction applications. Frontiers in Materials 6.
Nerella, V.N., Hempel, S., Mechtcherine, V., 2019. Effects of layer-interface properties on mechanical performance of concrete elements produced by extrusion-based 3D-printing. Construct. Build. Mater. 205, 586–601.
Ngo, T.D., Kashani, A., Imbalzano, G., Nguyen, K.T.Q., Hui, D., 2018. Additive manufacturing (3D printing): a review of materials, methods, applications and challenges. Compos. B Eng. 143, 172–196.
Ogura, H., Nerella, V.N., Mechtcherine, V., 2018. Developing and testing of strain-hardening cement-based composites (SHCC) in the context of 3D-printing. Materials 11 (8).
Ooms, T., Vantyghem, G., Van Coile, R., De Corte, W., 2021. A parametric modelling strategy for the numerical simulation of 3D concrete printing with complex geometries. Addit. Manuf. 38, 101743.
Panda, B., Paul, S.C., Hui, L.J., Tay, Y.W.D., Tan, M.J., 2017. Additive manufacturing of geopolymer for sustainable built environment. J. Clean. Prod. 167, 281–288.
Panda, B., Lim, J.H., Tan, M.J., 2019a. Mechanical properties and deformation behaviour of early age concrete in the context of digital construction. Compos. B Eng. 165, 563–571.
Panda, B., Unluer, C., Tan, M.J., 2019b. Extrusion and rheology characterization of geopolymer nanocomposites used in 3D printing. Compos. B Eng. 176, 107290.
Pasupathy, K., Ramakrishnan, S., Sanjayan, J., 2022. Enhancing the properties of foam concrete 3D printing using porous aggregate. Cement Concr. Compos., 104687
Perrot, A., Rangeard, D., Courteille, E., 2018. 3D printing of earth-based materials: processing aspects. Construct. Build. Mater. 172, 670–676.
Perrot, A., Jacquet, Y., Rangeard, D., Courteille, E., Sonebi, M., 2020. Nailing of layers: a promising way to Reinforce concrete 3D printing structures. Materials 13 (7).
Pierre, A., Weger, D., Perrot, A., Lowke, D., 2018. Penetration of cement pastes into sand packings during 3D printing: analytical and experimental study. Mater. Struct. 51 (1), 22.
Pott, U., Stephan, D., 2021. Penetration test as a fast method to determine yield stress and structural build-up for 3D printing of cementitious materials. Cement Concr. Compos. 121, 104066.
Rahul, A.V., Santhanam, M., 2020. Evaluating the printability of concretes containing lightweight coarse aggregates. Cement Concr. Compos. 109, 103570.
Rahul, A.V., Santhanam, M., Meena, H., Ghani, Z., 2019. 3D printable concrete: mixture design and test methods. Cement Concr. Compos. 97, 13–23.
Rahul, A.V., Mohan, M.K., De Schutter, G., Van Tittelboom, K., 2022. 3D printable concrete with natural and recycled coarse aggregates: rheological, mechanical and shrinkage behaviour. Cement Concr. Compos. 125, 104311.
Ramakrishnan, S., Muthukrishnan, S., Sanjayan, J., Pasupathy, K., 2021. Concrete 3D printing of lightweight elements using hollow-core extrusion of filaments. Cement Concr. Compos. 123, 104220.
Ranjbar, N., Kuenzel, C., Gundlach, C., Kempen, P., Mehrali, M., 2022. Halloysite reinforced 3D-printable geopolymers. Cement Concr. Compos. 136, 104894.
Reiter, L., Wangler, T., Anton, A., Flatt, R.J., 2020. Setting on demand for digital concrete – Principles, measurements, chemistry, validation. Cement Concr. Res. 132, 106047.
Salari, F., Bosetti, P., Sglavo, V.M., 2022. Binder jetting 3D printing of magnesium oxychloride cement-based materials: parametric analysis of manufacturing factors. Journal of Manufacturing and Materials Processing 6 (4).
Salet, T.A.M., Ahmed, Z.Y., Bos, F.P., Laagland, H.L.M., 2018. Design of a 3D printed concrete bridge by testing. Virtual Phys. Prototyp. 13 (3), 222–236.
Sambucci, M., Marini, D., Valente, M., 2020a. Tire Recycled Rubber for More Eco-Sustainable Advanced Cementitious Aggregate. Recycling.
Sambucci, M., Marini, D., Sibai, A., Valente, M., 2020b. Preliminary mechanical analysis of rubber-cement composites suitable for additive process construction. Journal of Composites Science.
Shakor, P., Sanjayan, J., Nazari, A., Nejadi, S., 2017. Modified 3D printed powder to cement-based material and mechanical properties of cement scaffold used in 3D printing. Construct. Build. Mater. 138, 398–409.
Shakor, P., Nejadi, S., Paul, G., Sanjayan, J., 2020a. Dimensional accuracy, flowability, wettability, and porosity in inkjet 3DP for gypsum and cement mortar materials. Autom. ConStruct. 110, 102964.
Shakor, P., Nejadi, S., Sutjipto, S., Paul, G., Gowripalan, N., 2020b. Effects of deposition velocity in the presence/absence of E6-glass fibre on extrusion-based 3D printed mortar. Addit. Manuf. 32, 101069.
Shakor, P., Nejadi, S., Paul, G., Gowripalan, N., 2021. Effects of Different Orientation Angle, Size, Surface Roughness, and Heat Curing on Mechanical Behavior of 3D Printed Cement Mortar With/Without Glass Fiber in Powder-Based 3DP, 3D Printing and Additive Manufacturing.
Shao, L., Feng, P., Zuo, W., Wang, H., Geng, Z., Liu, Q., Miao, C., Liu, Z., 2022. A novel method for improving the printability of cement-based materials: controlling the releasing of capsules containing chemical admixtures. Cement Concr. Compos. 128, 104456.
Sikora, P., Techman, M., Federowicz, K., El-Khayatt, A.M., Saudi, H.A., Abd Elrahman, M., Hoffmann, M., Stephan, D., Chung, S.-Y., 2022. Insight into the microstructural and durability characteristics of 3D printed concrete: cast versus printed specimens. Case Stud. Constr. Mater. 17, e01320.
Soltan, D.G., Li, V.C., 2018. A self-reinforced cementitious composite for building-scale 3D printing. Cement Concr. Compos. 90, 1–13.
Suiker, A.S.J., Wolfs, R.J.M., Lucas, S.M., Salet, T.A.M., 2020. Elastic buckling and plastic collapse during 3D concrete printing. Cement Concr. Res. 135, 106016.
Sun, J., Xiao, J., Li, Z., Feng, X., 2021a. Experimental study on the thermal performance of a 3D printed concrete prototype building. Energy Build. 241, 110965.
Sun, J., Huang, Y., Aslani, F., Wang, X., Ma, G., 2021b. Mechanical enhancement for EMW-absorbing cementitious material using 3D concrete printing. J. Build. Eng. 41, 102763.
Sun, B., Zeng, Q., Wang, D., Zhao, W., 2022. Sustainable 3D printed mortar with CO2 pretreated recycled fine aggregates. Cement Concr. Compos. 134, 104800.
Talke, D., Saile, B., Meier, N., Herding, F., Mai, I., Zetzener, H., Kwade, A., Lowke, D., 2023. Particle-bed 3D printing by selective cement activation – influence of process parameters on particle-bed density. Cement Concr. Res. 168, 107140.
Tan, Z., Bernal, S.A., Provis, J.L., 2017. Reproducible mini-slump test procedure for measuring the yield stress of cementitious pastes. Mater. Struct. 50 (6), 235.
Tao, Y., Ren, Q., Lesage, K., Van Tittelboom, K., Yuan, Y., De Schutter, G., 2022a. Shape stability of 3D printable concrete with river and manufactured sand characterized by squeeze flow. Cement Concr. Compos. 133, 104674.
Tao, J.-L., Lin, C., Luo, Q.-L., Long, W.-J., Zheng, S.-Y., Hong, C.-Y., 2022b. Leveraging internal curing effect of fly ash cenosphere for alleviating autogenous shrinkage in 3D printing. Construct. Build. Mater. 346, 128247.
Tay, Y.W.D., Li, M.Y., Tan, M.J., 2019. Effect of printing parameters in 3D concrete printing: printing region and support structures. J. Mater. Process. Technol. 271, 261–270.
Tay, Y.W.D., Lim, J.H., Li, M., Tan, M.J., 2022. Creating functionally graded concrete materials with varying 3D printing parameters. Virtual Phys. Prototyp. 17 (3), 662–681.
Tinoco, M.P., de Mendonça, É.M., Fernandez, L.I.C., Caldas, L.R., Reales, O.A.M., Toledo Filho, R.D., 2022. Life cycle assessment (LCA) and environmental sustainability of cementitious materials for 3D concrete printing: a systematic literature review. J. Build. Eng. 52, 104456.
Toklu, Y.C., Bekdaş, G., Geem, Z.W., 2020. Harmony search optimization of nozzle Movement for additive manufacturing of concrete structures and concrete elements. Appl. Sci. 10 (12).
Tošić, Z., Eichenauer, M.F., Ivaniuk, E., Lordick, D., Krasić, S., Mechtcherine, V., 2022. Design and optimization of free-form surfaces for modular concrete 3D printing. Autom. ConStruct. 141, 104432.
Tu, H., Wei, Z., Bahrami, A., Ben Kahla, N., Ahmad, A., Özkılıç, Y.O., 2023. Recent advancements and future trends in 3D concrete printing using waste materials. Developments in the Built Environment 16, 100187.
van den Heever, M., du Plessis, A., Kruger, J., van Zijl, G., 2022a. Evaluating the effects of porosity on the mechanical properties of extrusion-based 3D printed concrete. Cement Concr. Res. 153, 106695.
van den Heever, M., du Plessis, A., Bester, F., Kruger, J., van Zijl, G., 2022b. A mechanistic evaluation relating microstructural morphology to a modified Mohr-Griffith compression-shear constitutive model for 3D printed concrete. Construct. Build. Mater. 325.
van den Heever, M., Bester, F., Kruger, J., van Zijl, G., 2022c. Numerical modelling strategies for reinforced 3D concrete printed elements. Addit. Manuf. 50, 102569.
Van Der Putten, J., De Volder, M., Van den Heede, P., De Schutter, G., Van Tittelboom, K., 2020. 3D printing of concrete: the influence on chloride penetration. In: Bos, F.P., Lucas, S.S., Wolfs, R.J.M., Salet, T.A.M. (Eds.), Second RILEM International Conference on Concrete and Digital Fabrication. Springer International Publishing, Cham, pp. 500–507.
Vantyghem, G., De Corte, W., Shakour, E., Amir, O., 2020. 3D printing of a post-tensioned concrete girder designed by topology optimization. Autom. ConStruct. 112, 103084.
Vespalec, A., Novák, J., Kohoutková, A., Vosynek, P., Podroužek, J., Škaroupka, D., Zikmund, T., Kaiser, J., Paloušek, D., 2020. Interface behavior and interface tensile strength of a hardened concrete mixture with a coarse aggregate for additive manufacturing. Materials 13 (22).
Vlachakis, C., Perry, M., Biondi, L., McAlorum, J., 2020. 3D printed temperature-sensing repairs for concrete structures. Addit. Manuf. 34, 101238.
Voney, V., Odaglia, P., Brumaud, C., Dillenburger, B., Habert, G., 2020. Geopolymer Formulation for binder Jet 3D printing. In: Bos, F.P., Lucas, S.S., Wolfs, R.J.M., Salet, T.A.M. (Eds.), Second RILEM International Conference on Concrete and Digital Fabrication. Springer International Publishing, Cham, pp. 153–161.
Wan, Q., Wang, L., Ma, G., 2022. Continuous and adaptable printing path based on transfinite mapping for 3D concrete printing. Autom. ConStruct. 142, 104471.
Wang, L., Tian, Z., Ma, G., Zhang, M., 2020. Interlayer bonding improvement of 3D printed concrete with polymer modified mortar: experiments and molecular dynamics studies. Cement Concr. Compos. 110, 103571.
Wang, L., Ma, G., Liu, T., Buswell, R., Li, Z., 2021a. Interlayer reinforcement of 3D printed concrete by the in-process deposition of U-nails. Cement Concr. Res. 148, 106535.

Wang, L., Liu, Y., Yang, Y., Li, Y., Bai, M., 2021b. Bonding performance of 3D printing concrete with self-locking interfaces exposed to compression–shear and compression–splitting stresses. Addit. Manuf. 42, 101992.
Wang, X., Jia, L., Jia, Z., Zhang, C., Chen, Y., Ma, L., Wang, Z., Deng, Z., Banthia, N., Zhang, Y., 2022a. Optimization of 3D printing concrete with coarse aggregate via proper mix design and printing process. J. Build. Eng. 56, 104745.
Wang, L., Aslani, F., Mukherjee, A., 2022b. Development of 3D printable self-sensing cementitious composites. Construct. Build. Mater. 337, 127601.
Wang, X., Li, W., Luo, Z., Wang, K., Shah, S.P., 2022c. A critical review on phase change materials (PCM) for sustainable and energy efficient building: design, characteristic, performance and application. Energy Build. 260, 111923.
Warsi, S.B.F., Panda, B., Biswas, P., 2023. Exploring fibre addition methods and mechanical properties of fibre-reinforced 3D printed concrete: a review. Developments in the Built Environment 16, 100295.
Weger, D., Gehlen, C., 2021. Particle-bed binding by selective paste intrusion—strength and durability of printed fine-Grain concrete Members. Materials 14 (3).
Weng, Y., Lu, B., Li, M., Liu, Z., Tan, M.J., Qian, S., 2018. Empirical models to predict rheological properties of fiber reinforced cementitious composites for 3D printing. Construct. Build. Mater. 189, 676–685.
Weng, Y., Li, M., Liu, Z., Lao, W., Lu, B., Zhang, D., Tan, M.J., 2019. Printability and fire performance of a developed 3D printable fibre reinforced cementitious composites under elevated temperatures. Virtual Phys. Prototyp. 14 (3), 284–292.
Weng, Y., Li, M., Ruan, S., Wong, T.N., Tan, M.J., Ow Yeong, K.L., Qian, S., 2020. Comparative economic, environmental and productivity assessment of a concrete bathroom unit fabricated through 3D printing and a precast approach. J. Clean. Prod. 261, 121245.
Westerlind, H., Hernández, J., 2020. Knitting concrete. In: Bos, F.P., Lucas, S.S., Wolfs, R. J.M., Salet, T.A.M. (Eds.), Second RILEM International Conference on Concrete and Digital Fabrication. Springer International Publishing, Cham, pp. 988–997.
Wolfs, R.J.M., Bos, F.P., Salet, T.A.M., 2018a. Early age mechanical behaviour of 3D printed concrete: numerical modelling and experimental testing. Cement Concr. Res. 106, 103–116.
Wolfs, R.J.M., Bos, F.P., Salet, T.A.M., 2018b. Correlation between destructive compression tests and non-destructive ultrasonic measurements on early age 3D printed concrete. Construct. Build. Mater. 181, 447–454.
Xia, M., Sanjayan, J., 2016. Method of formulating geopolymer for 3D printing for construction applications. Mater. Des. 110, 382–390.
Xia, M., Nematollahi, B., Sanjayan, J., 2019. Printability, accuracy and strength of geopolymer made using powder-based 3D printing for construction applications. Autom. ConStruct. 101, 179–189.
Xiao, J., Zou, S., Yu, Y., Wang, Y., Ding, T., Zhu, Y., Yu, J., Li, S., Duan, Z., Wu, Y., Li, L., 2020. 3D recycled mortar printing: system development, process design, material properties and on-site printing. J. Build. Eng. 32, 101779.
Xiao, J., Zou, S., Ding, T., Duan, Z., Liu, Q., 2021. Fiber-reinforced mortar with 100% recycled fine aggregates: a cleaner perspective on 3D printing. J. Clean. Prod. 319, 128720.
Xiao, J., Lv, Z., Duan, Z., Hou, S., 2022. Study on preparation and mechanical properties of 3D printed concrete with different aggregate combinations. J. Build. Eng. 51, 104282.
Xu, N., Qian, Y., Yu, J., Leung, C.K.Y., 2022. Tensile performance of 3D-printed Strain-Hardening Cementitious Composites (SHCC) considering material parameters, nozzle size and printing pattern. Cement Concr. Compos. 132, 104601.
Yang, Y., Wu, C., Liu, Z., Zhang, H., 2022a. 3D-printing ultra-high performance fiber-reinforced concrete under triaxial confining loads. Addit. Manuf. 50, 102568.
Yang, Y., Wu, C., Liu, Z., Wang, H., Ren, Q., 2022b. Mechanical anisotropy of ultra-high performance fibre-reinforced concrete for 3D printing. Cement Concr. Compos. 125, 104310.
Yao, Y., Hu, M., Di Maio, F., Cucurachi, S., 2020. Life cycle assessment of 3D printing geo-polymer concrete: an ex-ante study. J. Ind. Ecol. 24 (1), 116–127.
Yu, S., Du, H., Sanjayan, J., 2020. Aggregate-bed 3D concrete printing with cement paste binder. Cement Concr. Res. 136, 106169.
Yu, S., Xia, M., Sanjayan, J., Yang, L., Xiao, J., Du, H., 2021. Microstructural characterization of 3D printed concrete. J. Build. Eng. 44, 102948.
Yu, S., Sanjayan, J., Du, H., 2022. Effects of cement mortar characteristics on aggregate-bed 3D concrete printing. Addit. Manuf. 58, 103024.
Zareiyan, B., Khoshnevis, B., 2017. Effects of interlocking on interlayer adhesion and strength of structures in 3D printing of concrete. Autom. ConStruct. 83, 212–221.
Zhang, Y., Zhang, Y., Liu, G., Yang, Y., Wu, M., Pang, B., 2018. Fresh properties of a novel 3D printing concrete ink. Construct. Build. Mater. 174, 263–271.
Zhang, Y., Zhang, Y., She, W., Yang, L., Liu, G., Yang, Y., 2019a. Rheological and harden properties of the high-thixotropy 3D printing concrete. Construct. Build. Mater. 201, 278–285.
Zhang, C., Hou, Z., Chen, C., Zhang, Y., Mechtcherine, V., Sun, Z., 2019b. Design of 3D printable concrete based on the relationship between flowability of cement paste and optimum aggregate content. Cement Concr. Compos. 104, 103406.
Zhang, C., Jia, Z., Wang, X., Jia, L., Deng, Z., Wang, Z., Zhang, Y., Mechtcherine, V., 2022a. A two-phase design strategy based on the composite of mortar and coarse aggregate for 3D printable concrete with coarse aggregate. J. Build. Eng. 54, 104672.
Zhang, Y., Qiao, H., Qian, R., Xue, C., Feng, Q., Su, L., Zhang, Y., Liu, G., Du, H., 2022b. Relationship between water transport behaviour and interlayer voids of 3D printed concrete. Construct. Build. Mater. 326, 126731.
Zhang, C., Deng, Z., Chen, C., Zhang, Y., Mechtcherine, V., Sun, Z., 2022c. Predicting the static yield stress of 3D printable concrete based on flowability of paste and thickness of excess paste layer. Cement Concr. Compos., 104494
Zhao, H., Hu, Y., Li, Y., Wang, K., Dehn, F., Li, W., 2024. Triaxial compressive performance of recycled aggregate/glass sand concrete: Experimental study and mechanism analysis. J. Clean. Prod. 442, 141006.
Zhi, P., Wu, Y.-C., Yang, Q., Kong, X., Xiao, J., 2022. Effect of spiral blade geometry on 3D-printed concrete rheological properties and extrudability using discrete event modeling. Autom. ConStruct. 137, 104199.
Zhou, W., McGee, W., Zhu, H., Gökçe, H.S., Li, V.C., 2022. Time-dependent fresh properties characterization of 3D printing engineered cementitious composites (3DP-ECC): on the evaluation of buildability. Cement Concr. Compos. 133, 104704.
Zhu, B., Pan, J., Nematollahi, B., Zhou, Z., Zhang, Y., Sanjayan, J., 2019. Development of 3D printable engineered cementitious composites with ultra-high tensile ductility for digital construction. Mater. Des. 181, 108088.
Zhu, B., Pan, J., Li, J., Wang, P., Zhang, M., 2022. Relationship between microstructure and strain-hardening behaviour of 3D printed engineered cementitious composites. Cement Concr. Compos. 133, 104677.
Zou, S., Xiao, J., Ding, T., Duan, Z., Zhang, Q., 2021. Printability and advantages of 3D printing mortar with 100% recycled sand. Construct. Build. Mater. 273, 121699.
Zuo, W., Dong, C., Keita, E., Roussel, N., 2020. Penetration study of liquid in powder bed for 3D powder-bed printing. In: Bos, F.P., Lucas, S.S., Wolfs, R.J.M., Salet, T.A.M. (Eds.), Second RILEM International Conference on Concrete and Digital Fabrication. Springer International Publishing, Cham, pp. 379–386.

Update

Developments in the Built Environment

Volume 19, Issue , October 2024, Page

DOI: https://doi.org/10.1016/j.dibe.2024.100442

Developments in the Built Environment 19 (2024) 100442

Contents lists available at ScienceDirect

Developments in the Built Environment

journal homepage: www.sciencedirect.com/journal/developments-in-the-built-environment

Corrigendum to "Concrete 3D printing technology for sustainable construction: A review on raw material, concrete type and performance" [Dev. Built. Environ. 17 (2024) 100378]

Xiaonan Wang [a,b], Wengui Li [a,*], Yipu Guo [a], Alireza Kashani [a], Kejin Wang [c], Liberato Ferrara [d], Isabel Agudelo [e]

[a] Centre for Infrastructure Engineering and Safety, School of Civil and Environmental Engineering, The University of New South Wales, NSW, 2052, Australia
[b] School of Civil and Environmental Engineering, University of Technology Sydney, NSW, 2007, Australia
[c] Department of Civil, Construction and Environmental Engineering, Iowa State University, IA, 50011, USA
[d] Department of Civil and Environmental Engineering, Politecnico di Milano, 20133, Milano, MI, Italy
[e] School of Industrial Design, Universidad Nacional de Colombia, Ave Cra 30 #45-3, Bogotá, Colombia

The authors regret the affiliation of the co-author should be updated from its English version to Spanish version. The fifth affiliation in the article should read as:

[e] School of Industrial Design, Universidad Nacional de Colombia, Ave Cra 30 #45-3, Bogotá, Colombia.

The authors would like to apologise for any inconvenience caused.

DOI of original article: https://doi.org/10.1016/j.dibe.2024.100378.
* Corresponding author. School of Civil and Environmental Engineering, The University of New South Wales, NSW, 2052, Australia.
E-mail address: wengui.li@unsw.edu.au (W. Li).

https://doi.org/10.1016/j.dibe.2024.100442

Available online 25 April 2024